ABSTRACT

WATKINS, MEGAN FAYE. A Heat Transfer Analysis of Vertical Dense Granular Flows. (Under the direction of Dr. Richard Gould).

Particle-based heat transfer fluids for concentrated solar power (CSP) tower applications offer a unique advantage over traditional fluids, as they have the potential to reach very high operating temperatures. The present work studies the heat transfer behavior of dense granular flows through cylindrical tubes as a potential system configuration for CSP tower receivers. Experimental studies were conducted using a bench-scale apparatus to examine the heat transfer to such a flow configuration, as well as examine the effect of system parameters on the heat transfer to the flow. The experimental results corroborate the observations of other researchers; namely, that the discrete nature of the flow limits the heat transfer from a tube wall to the flow due to an increased thermal resistance in the layer of particles adjacent to the heated wall. A two-layer model was developed to describe this heat transfer phenomenon. The model assumed the flow was composed of two layers: a bulk layer characterized by the bulk effective properties of the flow, and a thin layer adjacent to the heated wall (with thickness of a particle radius) characterized by an effective thermal conductivity (ETC). A correlation to approximate the ETC of the wall-adjacent layer was developed, taking into consideration how the ETC may vary with flow rate and the system configuration. The packing fraction of the wall-adjacent layer and the number of particles in contact with the wall were found to control the heat transfer from the heated wall. Discrete Element Method (DEM) simulations indicated that both these parameters decrease with increasing flow rate, which manifests in a decrease in heat transfer with increasing flow rate. Data from DEM simulations for six system configurations was used to develop empirical correlations to predict these parameters for different flow rates and system configurations.

Incorporating the empirical correlations into the ETC correlation developed for the wall-adjacent layer allowed the heat transfer to the flow to be predicted using the two-layer model. The model showed good agreement with the experimental results taken for different tube diameters, particle diameters, and flow rates (within the experimental uncertainty). The experimental results and model suggest that, at low operating temperatures (<200°C), the heat transfer to a flow increases with increasing tube diameter and/or decreasing particle diameter due to the relative size of the wall-adjacent layer within the flow.

As a final step, the heat transfer to dense flows at operating temperatures more characteristic of CSP applications was studied. The effect of temperature on the heat transfer to the flow was examined for a single flow rate. The results demonstrated an increase in the heat transfer with increasing temperature due to enhanced thermal properties at higher temperatures. The influence of radiation was also examined by developing a simple radiation model for the wall-adjacent layer. For the small particle diameters tested in the present study (<320μm), radiation did not contribute significantly to the overall heat transfer. The model suggests, however, that the radiation contribution will increase with increasing particle diameter due to the increased void size. The results from all aspects of the current work provide an understanding of the parameters controlling the heat transfer to a dense granular flow and pave the way for designing future dense flow systems.

A Heat Transfer Analysis of Vertical Dense Granular Flows

by
Megan Faye Watkins

A dissertation submitted to the Graduate Faculty of
North Carolina State University
in partial fulfillment of the
requirements for the degree of
Doctor of Philosophy

Mechanical Engineering

Raleigh, North Carolina

2018

APPROVED BY:

_____	_____
Richard Gould Committee Chair	Alexei Saveliev
_____	_____
Tiegang Fang	Brendan O'Connor

DEDICATION

To my parents,

for their never-ending love and support;

To my brothers,

who have supported me since birth, nurturing my love for math and science;

And to my boyfriend,

who has been my rock throughout this entire experience.

BIOGRAPHY

Megan Watkins grew up in Saratoga Springs, NY, the youngest of three children. From a very early age, she had a love for math and science, which propelled her to begin studying engineering in high school, as part of the Project Lead the Way program. She received her BS in Mechanical Engineering from Binghamton University in May 2013. During her time at Binghamton, she gained an interest in renewable energy technologies. After graduation, she came to North Carolina State University in pursuit of her PhD in Mechanical Engineering, where she was fortunate enough to find a research project focused in concentrated solar power technologies. She has grown fond of the thermal sciences during her time at NC State and hopes to continue to use her new background to continue working in the field of renewable energy technologies, continuing work in concentrated solar power or learning about building enclosures.

ACKNOWLEDGMENTS

First and foremost, I would like to thank my advisor, Dr. Richard Gould, for his support and guidance over the past four and a half years, and for sparking my interest in the thermal sciences. I would also like to thank the members of my committee, Dr. Alexei Saveliev, Dr. Tiegang Fang, and Dr. Brendan O'Connor, for their time and input into my research. To my labmates, Yesaswi Chilamkurti and Alex Szerszen, thank you for all your valuable feedback, picking me up when I was down, and for creating such a friendly work environment. I could not have asked for better colleagues and friends. I would also like to express gratitude to ARPA-E for the financial support they provided during my time at NC State, as well as the feedback they provided and the opportunity to be part of such a large project. In conjunction, I would also like to thank everyone at RTI International for their guidance with my work, questioning me and forcing me to grow throughout this experience.

Finally, I would like to thank all my friends and family for keeping me sane throughout this adventure called grad school. To all my friends from church and my soccer team, thank you for helping me find fun things to do outside of school and providing a safety net when I was having a rough day. To my parents, brothers, and family near and far, thank you for your love and support, encouraging me when I needed a boost, for your interest in my work, even if you did not understand the details, and for just always being there for me. And finally, to my boyfriend, Ben, for keeping my light-hearted, fun-loving nature alive when I was struggling to do so by myself.

TABLE OF CONTENTS

LIST OF TABLES

LIST OF FIGURES

Chapter 1

Introduction

At a given instant in time, the amount of solar energy striking the Earth's surface is more than 10,000 times the total energy consumed worldwide [1]. The key challenge facing researchers today is how best to capture and utilize this unlimited resource. While photovoltaics are the most commonly recognized technologies implemented to capture the sun's energy, concentrated solar power (CSP) technologies are gaining momentum. Central receiver, or solar tower, systems utilize a field of heliostats, which focus the sun's radiation onto a central point at the top of a tower. A heat transfer fluid (HTF) located in the receiver at the top of the tower absorbs the sun's energy. After collecting the heat energy from the sun, the heat transfer fluid travels down the tower and passes through a heat exchanger to a power block. The efficiency of such a power plant is directly related to the temperature of the hot reservoir; a higher temperature yields a more efficient cycle.

Solar power towers offer the potential to reach extremely high operating temperatures (>1000°C), thereby enabling more efficient power plant cycles. A variety of obstacles must first be overcome, however, to develop a system that utilizes the high operating potential of central receiver towers. One of the main challenges is developing a new HTF that can operate at such high temperatures. Molten nitrate salts and steam are two of the most common HTFs currently in use in solar tower systems. The Ivanpah Solar Power Facility in California, for example, implements

steam, while the Crescent Dunes Solar Energy Project in Nevada implements molten salts [2]. Both HTFs demonstrate attractive qualities; molten salts can be used as both a HTF and for thermal energy storage, while steam reduces the need for an intermediate heat exchanger, as the steam can directly drive the power plant turbine. Both fluids, however, have drawbacks; molten salts have a limited working temperature domain (approximately 240-565°C), while steam requires very high pressures and an additional material for thermal energy storage. A HTF that can operate over a very wide temperature range and act as a thermal energy storage medium would be ideal for increasing the efficiency of solar power tower systems and reducing the overall cost of such systems. Liquid metals demonstrate a higher operational temperature, but can be highly corrosive and present safety concerns [3].

Solid particle-based HTFs are currently being studied in various forms, as they can operate over a very wide temperature range, act as a thermal energy storage medium, and pose no safety concerns. Many current research efforts focus on maximizing the heat collected in the solar receiver by altering the receiver design and the type of particle flow implemented. Fluidized beds of particles [4], falling particle curtains [5], and flows of particles over absorber tubes [6] are three examples of solid particle-based receiver configurations. Our work investigates gravity-driven dense granular flows through vertical tubes as another possible system configuration.

Internal gravity-driven particulate flows have been studied extensively for decades due to their numerous practical applications, such as the flow of food grains. Vertical chute flows are characterized by shearing at the wall boundaries. In general, granular flows can be divided into three flow regimes: quasi-static, dense, and dilute [7]. Quasi-static flows encompass slow flow rates where the inertia of individual particles is negligible. These flows are characterized by a strong contact network amongst particles and are therefore often referred to as a granular solid.

Dilute, or “gaseous”, flows occur at fast flow rates, where the collisions between particles drive the motion of the flow. Binary collisions between particles are characteristic of this flow regime; as a result, the kinetic theory of dense gases is often employed to describe these flows. The transitional flow regime, often referred to as the dense flow regime, features characteristics of both the quasi-static and dilute flow regimes; the inertia of individual particles is important while a contact network between particles also exists. Dense and quasi-static flows are characterized by dense packings, with packing fractions typically around 60%, while dilute flows are characterized by lower packing fractions, down to approximately 30% [8].

The dense flow regime was selected as a viable option for concentrated solar power applications based on an understanding of the internal heat transfer mechanics of a particulate flow. While the heat transfer to dense flows has been studied relatively sporadically over the past few decades, there is an abundance of literature regarding the heat transfer to static beds of particles and fluidized beds (for example [9], [10]). It is well understood in the scientific community that the particle volume packing fraction strongly effects the overall heat transfer to a particulate bed. Three main heat transfer mechanisms exist within a particulate bed: particle-particle conduction, particle-fluid-particle conduction, and radiation through the void spaces. Each heat transfer mechanism is depicted in Figure 1.1, which illustrates a unit cell composed of two particles. Particle-particle conduction describes the heat transfer between particles via the contact area. In general, the contact area between two particles is quite small, resulting in negligible heat transfer by particle-particle conduction. The contribution due to particle-particle conduction becomes more significant when a large compressive load is applied to the particle bed and/or when the particles deform easily [11], [12]. The particle-particle conduction is also important in a particle bed with a large particle-to-gas thermal conductivity ratio (>1000) [9]. In general, however, the majority of

the heat transfer in a bed occurs through the interstitial gas between particles (particle-fluid-particle conduction). Since, in most cases, the particles demonstrate superior thermal properties compared with the interstitial gas, small void spaces between particles are desired to maximize the heat transfer. Therefore, we believe that using granular flows with a high packing fraction will enhance the overall heat transfer to the flow. The dense flow regime was selected over the quasi-static regime due to the increased particle agitation in faster flows. Increased particle agitation was initially thought to provide a small mixing component that could enhance the heat transfer slightly over quasi-static flows.

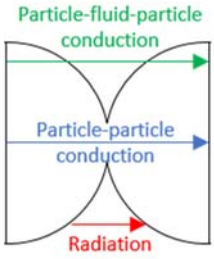

Figure 1.1: Heat transfer mechanisms present in a unit cell composed of two particles.

One potential trade-off of using flows with such high packing fractions is a reduced heat transfer due to particle mixing. Just as mixing enhances the heat transfer within turbulent flows, mixing of particles enhances the heat transfer from the wall to the flow. Particle mixing in granular flows can be achieved using very fast, dilute flows, or by introducing a fluidizing gas. Dilute flows, which exhibit packing fractions as low as 30%, introduce mixing when collisions between particles cause particles to "stream" across the flow. Hsiau & Hunt [13] studied this heat transfer phenomenon, using the kinetic theory of dense gases to develop an effective thermal conductivity model to characterize the "streaming" behavior. Natarajan & Hunt [14] note that the heat transfer due to streaming opposes the heat transfer due to molecular conduction; as the streaming contribution increases with decreasing packing fraction, the contribution from molecular

conduction decreases. No clear indication was given as to whether the heat transfer to a dilute flow with streaming was superior to a denser flow with better molecular conduction. Particle flows that utilize a fluidization gas rely on a similar streaming behavior, as the resulting circulation of particles within the bed continually brings new particles in contact with the wall. Flamant et al. [4] investigated the heat transfer to an upward circulating bed of dense particle suspensions, which demonstrate packing fractions up to 35% for slower gas velocities. They observed intriguing heat transfer properties, noting that the packing fraction and particle velocity strongly influence the heat transfer to the flow. One drawback of such a system is the thermal loss to the fluidization gas.

The study of heat transfer to dense granular flows dates back to the mid-1900's. Brinn et al. [15] examined the heat transfer to granular flows through a vertical tube subjected to a constant wall temperature. The experimental results were compared with an analytic solution for a laminar plug flow. They found good agreement between the analytic solution and the experimental results. Sullivan & Sabersky [16] studied the heat transfer to vertical chute flows with a single heated wall. Their experimental results did not agree with the results predicted by a continuum solution for their setup; instead, the granular flows demonstrated inferior heat transfer performance, which was attributed to the interaction between the particles and the wall. A semi-empirical correlation relating the Nusselt number with the Péclet number was developed to capture the reduced heat transfer observed in the particulate flows. The correlation developed assumed that the flow consists of a bulk core region and a small interstitial gas layer separating the wall and the bulk region. The model, which assumed the gas layer was a fraction of a particle diameter thick (0.085 in their case), showed good agreement with their experimental results. The contact resistance was assumed constant across all flow rates. Natarajan & Hunt [17] expanded upon the work of Sullivan & Sabersky by studying vertical chute flows with longer heated sections and faster flow rates. The

model developed by Sullivan & Sabersky showed good agreement with their experimental results for low velocity, high-density flows. The model, however, did not capture the decrease in heat transfer observed at very fast flow rates.

Spelt et al. [18], Patton et al. [19], and Ahn [20] studied the heat transfer to granular flows down an inclined chute across a wide range of flow rates. Similar to Natarajan & Hunt [17], their results showed good agreement with the model developed by Sullivan & Sabersky for low velocity flows. Unlike the vertical flows of Sullivan & Sabersky and Natarajan & Hunt, however, the best agreement with the model was found using an air layer thickness of approximately 0.025 of a particle diameter. The smaller air gap was attributed to the difference in system configuration; gravity pushes particles toward the wall in an inclined chute, whereas gravity has no effect on the compactness of particles at the wall in a vertical chute. Similar to Natarajan & Hunt, a critical flow rate was observed in each of these inclined chute studies, after which the heat transfer to the flow began to decrease. The presence of a critical value and deviation from the model at higher flow rates was explained by recognizing that the density of the flow (directly related to the packing fraction) adjacent to the heated surface plays a crucial role in the heat transfer to the flow. At low flow rates, there is little change in the density near the wall; however, as the flow rate increases, the packing begins to loosen and the density adjacent to the heated surface reduces. Due to the increased volume of air, the contact resistance increases with increasing flow rate. Ahn attempted to modify the model developed by Sullivan & Sabersky to account for the variation in the contact resistance with packing fraction; their model, however, was only successful with certain particle materials.

Schlünder [21] and Denloye & Botterill [22] also recognized the importance of the wall-adjacent layer on the overall heat transfer to the flow. Both these works calculated the contact

resistance using correlations derived based on the physics of the problem, rather than an empirical constant like that used in the Sullivan & Sabersky model. Denloye & Botterill, who also studied the heat transfer to vertical chute flows, used the "packet renewal theory" originally developed by Mickley & Fairbanks [23] for fluidized beds to compare with experimental data. The modified version of the model developed by Baskakov [24], which incorporates a thermal contact resistance at the heated surface, was also implemented. The near-wall thermal conductivity correlation for a static bed derived by Yagi & Kunii [25] was used to calculate the contact resistance. The modified model showed better agreement with the experimental data, compared with the original model, once again indicating the importance of the wall-adjacent layer on the overall heat transfer to the flow. Schlünder used the same correlation developed by Sullivan & Sabersky, but utilized the heat transfer coefficient correlation developed in his previous work [26] for the wall-adjacent layer to approximate the wall contact resistance. The models were used to predict the experimental results observed throughout the literature for particulate flows. He found reasonable agreement with the experimental results of Ernst [27] and Botterill et al. [28] but not with the experimental data of Sullivan & Sabersky.

More recently, Morris et al. [29] sought to characterize the heat transfer through the wall-adjacent layer using the same physics applied in Discrete Element Method (DEM) simulations. They observed that the heat transfer to a particle from the wall reduces quickly upon losing contact with the wall, as the small layer of air between the particle and the wall acts as a layer of insulation. To more accurately predict the heat transfer from a heated wall to the layer of particles adjacent to the wall, they incorporated a particle distribution function to incorporate heat transfer to both particles in contact with the wall and those not in contact. An empirical correlation for the Nusselt number, in the form of a 7^{th}-order polynomial, describing the heat transfer coefficient within the

wall-adjacent layer was developed for flow down an inclined plane. Morris et al. [6] applied the derived correlation as a boundary condition to a two-phase continuum model to examine the heat transfer to dense granular flows over an array of hexagonal tubes. They observed a decrease in the heat transfer from the heated surface to the flow with increasing flow velocity, which was attributed to the loosening of the packing adjacent to the wall. The results from the continuum model were compared with those from DEM simulations; they found relatively good agreement between the two modelling techniques.

The above-mentioned works focus on low temperature measurements, where radiation between particles is negligible. Radiation heat transfer is expected, however, to be an important mechanism at temperatures typical of concentrated solar power towers. We are unaware of any previous works that have studied the heat transfer to dense granular flows at temperatures where radiation is significant. Experimental investigations of the heat transfer through a static particle bed over a wide range of temperatures suggest an increase in the heat transfer with increasing temperature, due to an increased radiative heat transfer contribution. Yagi & Kunii [30], for example, measured the effective thermal conductivity (ETC) for various particle materials and particle shapes. They concluded that the particle diameter and particle material have a strong effect on the effective thermal conductivity of the beds. Similar results have been observed using analytical models. The model developed by Cheng & Yu [31], which showed relatively good agreement with experimental results for glass and iron particles, was used to examine the relative contribution of each major heat transfer mechanism (as defined in Figure 1.1) and how parameters such as particle diameter and emissivity effect the ETC. For the particle diameters tested (2 to 20 mm), the ETC increased with increasing particle diameter at higher temperatures, as the size of the void spaces effects the penetration of the radiation. For the range of particles tested, the relative

contribution of radiation was greater than the conduction contribution at higher temperatures. The temperature at which the radiation becomes more significant depends on the particle diameter. For particles less than 2mm in diameter, the conduction contribution is the dominant mechanism.

The objective of the present work is to characterize the heat transfer to vertical dense granular flows through cylindrical tubes over a broad temperature range, gaining an understanding of the parameters and fundamental mechanics that effect the overall heat transfer to the flow. This goal has been achieved by completing tasks which can broadly be subdivided into three groups: experimental study of low temperature (<200°C) flows, analytical study of heat transfer to particulate flows, with emphasis placed on the wall contact resistance, and combined experimental and analytical study of heat transfer to flows at high operating temperatures (up to 1000°C).

An experimental apparatus was designed and used to study the heat transfer to gravity-driven, dense granular flows through vertical cylindrical tubes. Multiple particle diameters, tube diameters, particle materials, and flow rates were examined, seeking insight into their effect on the heat transfer to the flow. The material and thermal properties of all particles tested were also assessed and used to characterize the heat transfer results observed (Chapter 2).

The results from the experimental study corroborate the results observed in the literature for chute flows; namely, that continuum solutions do not accurately predict the heat transfer to particulate flows. An analytic model for the Nusselt number was developed for flow through cylindrical tubes, incorporating a contact resistance at the wall. A correlation was developed to predict the resistance to heat transfer in the layer of particles adjacent to the heated wall, with attention placed on examining how the resistance to heat transfer varies with flow rate. An understanding of how fundamental flow parameters, such as the packing fraction adjacent to the wall and number of particle-wall contact points, varied with flow rate was incorporated, ultimately

providing an understanding of how the heat transfer to the flow varies with flow rate (Chapter 3). The model developed was then compared with the experimental results of the present study, as well as experimental results found in the literature for vertical chute flows (Chapter 4).

Finally, the experimental apparatus used to characterize the heat transfer at low operating temperatures was modified to accommodate measurements at much higher operating temperatures. The effect of temperature on the heat transfer to the flow was studied using multiple tube and particle diameters. The analytic model was modified to incorporate a radiation contribution, which was compared with the experimental results (Chapter 5).

Chapter 2

Experimental Study of Heat Transfer to Particulate Beds and Flows

The heat transfer capabilities of dense granular flows through cylindrical tubes was first characterized at low temperatures, gaining an understanding of the important parameters that effect the overall heat transfer to the flow and fine-tuning the experimental apparatus to best estimate the heat transfer capabilities. Heat transfer measurements were then performed at temperatures more characteristic of CSP applications. The following sections introduce the particles utilized, discussing the characterization of both their mechanical and thermal properties. The experimental apparatus designed to study the heat transfer to the flows at low operating temperatures (< 200°C) and the corresponding results is also reviewed.

2.1. Heat Transfer to Dense Granular Flows

A bench-scale experimental apparatus was designed to examine the heat transfer to dense granular flows through cylindrical tubes. In an attempt to understand the parameters that effect the heat transfer to the flow, various tube diameters, particle diameters, and flow rates were examined.

The following sections introduce the experimental apparatus implemented throughout the study, the system parameters tested, and the techniques used to quantify the heat transfer to the flow.

2.1.1. Apparatus & Procedures

The bench-scale apparatus designed to examine the heat transfer to the particulate flows can be seen in Figure 2.1. A 1.82m long Inconel tube was suspended vertically from a structural frame using three support bars. Heat losses through the support bars were minimized by placing ceramic spacers between the tube and the support bar. A supply hopper was attached to the top of the tube using a series of pipe reducers, which allowed the apparatus to be utilized for a batch process. A 60mm long quartz tube was sandwiched between the supply hopper and the top of the Inconel tube, acting as a thermal break to prevent the conduction of heat to the particles in the supply hopper. An Inconel orifice was attached to the exit of the tube to control the flow rate. The orifices were manufactured with an angle greater than that of the angle of repose of the particles, yielding a mass flow (no stagnant particles near the wall). The mass of particles exiting the orifice every second was measured using an OHAUS scale (resolution of ±0.2g), allowing for the calculation of the mass flow rate. Note that all primary components of the apparatus were made of Inconel, as ultimately the goal was to test the particulate flows at very high operating temperatures (up to 1000°C). A constant wall heat flux boundary condition was applied to the flow by ohmically heating the tube. Copper clamps were attached to the top and bottom of the tube, 1.57m apart. 3/0 copper welding cables connected the copper clamps to a 10kW low voltage, high current power supply (TDK-Lambda GEN 20-500-3P208). The heating power supplied to the flow was determined by measuring the voltage drop across the tube and multiplying by the current sourced.

The entire length of the tube was surrounded by 95mm of ceramic and high temperature mineral wool insulation.

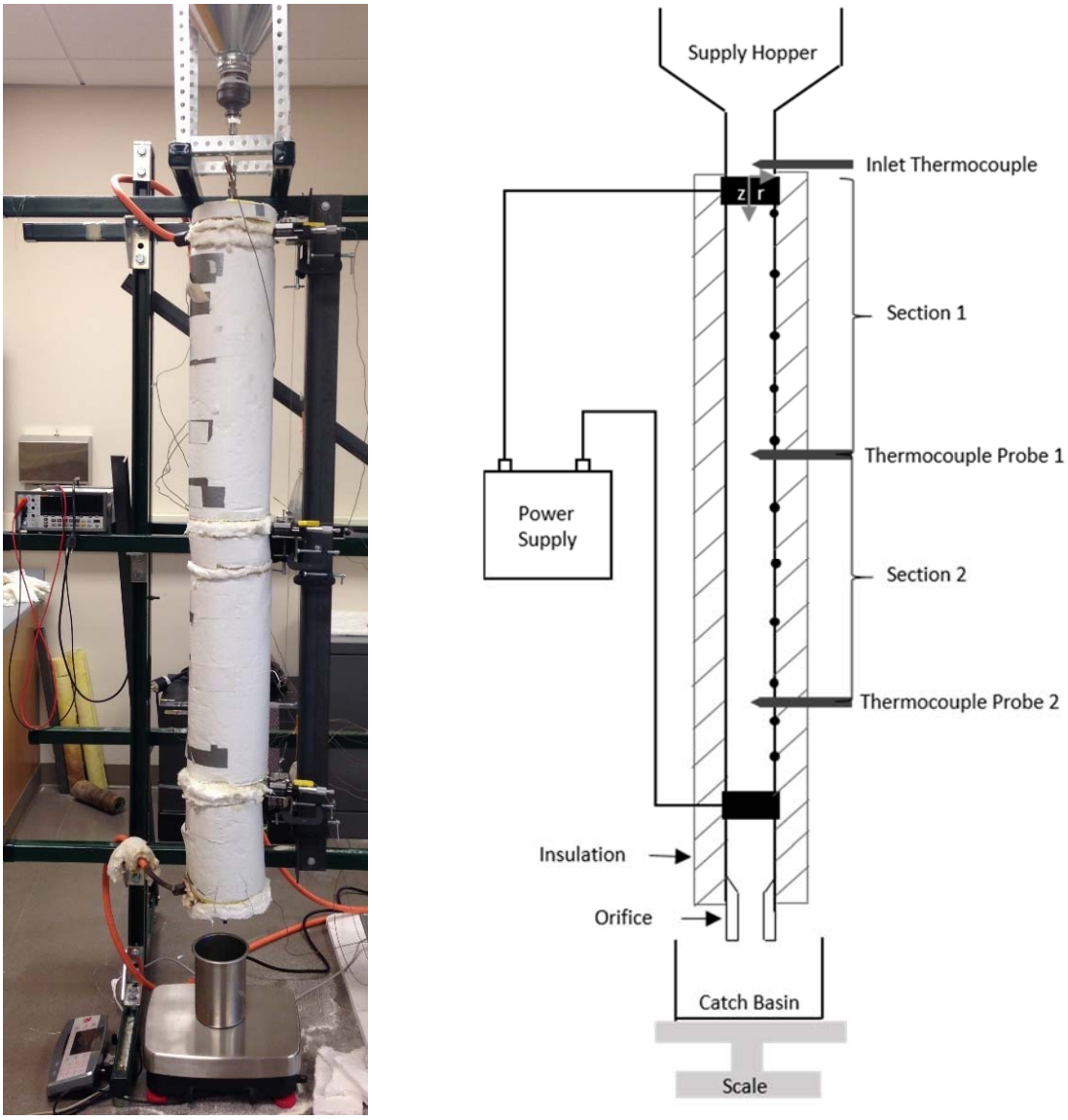

Figure 2.1: Experimental apparatus used to characterize the heat transfer to dense granular flows.

The temperature of the tube wall was monitored at 11 axial locations using type K thermocouples. Type K thermocouples were selected, as they provide reliable results over a very wide temperature range (-200 to 1200°C). Each thermocouple was attached to the wall using an Inconel hose clamp. A thin sheet of mica was placed around the thermocouple bead to prevent the

temperature measurements from being altered by the current sourced through the tube. The temperature of the flow was monitored at three axial locations using type K thermocouple probes. The probes (0.82mm sheath OD) were inserted into the flow via 1.4mm holes drilled into the tube wall. Each probe was attached to a linear position slider (Figure 2.2), which allowed the thermocouple to be traversed across the radius of the tube, measuring the flow temperature at known radial locations. A radial temperature distribution was then constructed from the radial temperature measurements. Two thermocouples were located within the heated section of the tube, 0.64 and 1.26m below the z = 0 position (top of copper clamp in Figure 2.1). The third thermocouple was located 6.35mm above the z = 0 position, measuring a temperature profile at the inlet to the heated section. A small temperature gradient existed at the inlet due to minor axial conduction through the tube.

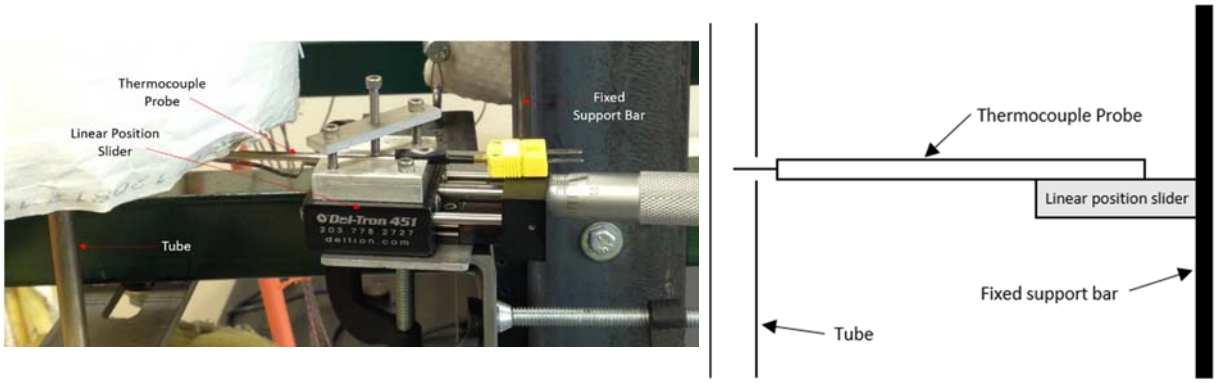

Figure 2.2: Thermocouple traversal system used to measure the radial temperature profiles.

All temperature measurements were made after steady state conditions had been achieved. Steady state was assumed to be achieved when the wall temperatures varied by less than ±0.2%. This condition was typically achieved in less than 2 hours. The volume of the supply hopper was considerably larger than that of the tube, allowing continuous operation throughout the duration of a trial. Particles were not recycled to the hopper after exiting the tube; rather room temperature particles were always maintained in the hopper.

A typical trial consisted of loading the supply hopper with sufficient particles to last the duration of the trial based on the desired flow rate. After commencing the flow of particles, recording of the mass accumulation and the temperatures were initiated. The current sourced through the tube was prescribed in order to obtain a desired flow temperature drop across the length of the tube. The tube and flow temperatures were allowed to reach essentially steady values. The flow thermocouple probes were then traversed across the radius of the tube, starting from the wall and ending at the centerline. Traversing the thermocouple into the tube prevented the particles from getting wedged in the hole in the tube wall, allowing for a smooth traversal of the thermocouple probe.

2.1.2. Test Cases

In an attempt to gain a more thorough and generalized understanding of the heat transfer to vertical dense granular flows through cylindrical tubes, a variety of system parameters were tested. In particular, five different system configurations were utilized to examine the effect of three different parameters: particle diameter, tube diameter, and particle material. Table 2.1 summarizes the different system configurations. The material and thermal properties of each particle material will be discussed in more detail in Section 2.2.

Table 2.1: Experimental system configurations.

Configuration Number	Tube OD (mm)	Particle Diameter (mm)	Tube-to-particle diameter ratio	Particle Material
1	9.53	0.140	54.4	Zirconia-silica
2	9.53	0.270	28.2	Zirconia-silica
3	9.53	0.320	23.8	Zirconia-silica
4	9.53	0.340	22.4	Alumina-silicate
5	12.70	0.270	40.1	Zirconia-silica

The effect of the flow rate on the heat transfer to the flow in each system configuration was also examined by utilizing five different orifices, each with a different diameter. The flow rates tested ranged from 1.5 to 9.5g/s. Faster flow rates could have been obtained, but required a sizable quantity of particles to maintain the flow for the duration of a trial; therefore, the heat transfer to faster flows was not examined in this study. Flows in the range tested demonstrate a choked flow phenomenon, which ensures an essentially constant mass flow rate throughout the duration of a trial. The mass flow rates measured followed the trend predicted by the Beverloo correlation, which describes the mass flow rate through a vertical tube based on the density of the flow, the particle diameter, and the orifice diameter [32].

Each system configuration was tested approximately 3-4 times to ensure repeatable results. The input heating power was varied for each test case to maintain similar mean flow temperatures at both fluid flow (FF) measurement locations for all cases. The thermal properties at each measurement location could thus be assumed approximately the same for every case tested. The present set of experiments, defined as the "low temperature measurements", utilized temperatures less than 200°C. The mean flow temperature at the z = 0.64m location was maintained at ~80°C, while the mean flow temperature at the z = 1.26m location was maintained at ~125°C.

2.1.3. Heat Transfer Characterization

The convective heat transfer coefficient was used as the metric for quantifying the heat transfer to the particulate flow. The heat transfer coefficient describes the ability of a flow to transfer heat from the wall and is expressed as

$$h = \frac{q''_{wall}}{T_w - T_m} \tag{1}$$

where q''_{wall} represents the input wall heat flux, T_w represents the wall temperature, and T_m represents the bulk mean flow temperature. The input heat flux represents the heating power per unit area of the internal surface of the tube. As seen in Figure 2.1, the tube was divided into two sections, the first section encompassing the length between the inlet of the heated section (z = 0m) and the thermocouple at z = 0.64m, and the second section encompassing the length between the thermocouple at z = 0.64m and the thermocouple at z = 1.26m. The electrical resistance of the tube varies slightly along the length of the tube due to the variation in temperature. As a result, the second section of the tube displays a slightly different wall heat flux than the first section. Only two sections were utilized for the calculation of the heat transfer coefficient to simplify the measurement process; however, utilizing smaller sections yields a more accurate description of the variation in the heat flux with axial position and therefore a more accurate heat transfer coefficient calculation. The variation in the wall heat flux was examined in more detail, which will be discussed in Section 2.3.

An accurate calculation of the heat flux entering the flow, and therefore heat transfer coefficient, was ensured by subtracting heat lost through the insulation from the total heating power generated due to ohmic heating. Heat losses through the insulation were estimated based on the thermal resistance of the insulation and the temperature drop across the insulation. Since the tube was surrounded by two different types of insulation (ceramic and mineral wool), the total thermal resistance was determined based on the sum of the two individual thermal resistances. The corresponding heat losses were determined according to

$$\dot{Q_{loss}} = \frac{2\pi L\left(T_{w,o} - T_{wool}\right)}{\frac{\ln(R_{cer}/R_o)}{k_{cer}} + \frac{\ln(R_{wool}/R_{cer})}{k_{wool}}} \tag{2}$$

where $\dot{Q_{loss}}$ represents the rate of heat loss through the insulation for a given length of tube, L, k_{cer} and k_{wool} represent the thermal conductivities of the ceramic insulation and the mineral wool

insulation, respectively, R_o, R_{cer}, and R_{wool} represent the radii of the outside of the tube, ceramic insulation, and mineral wool insulation, respectively, and $T_{w,o}$ and T_{wool} represent the temperatures of the outside of the tube and the mineral wool insulation, respectively. The heat losses were calculated for both the top and bottom tube sections. The temperature-dependent thermal conductivities of the insulations were obtained from manufacturer data [33]–[35]. The thermal conductivities at the average insulation temperature, determined using $T_{w,o}$ and T_{wool}, were used. A thermal imaging camera (FLIR E40) was used to determine the temperature on the outside of the insulation (T_{wool}). The temperature was determined by taking an average of the values measured along the perimeter of the insulation. A sample thermal image can be seen in Figure 2.3.

Figure 2.3: Example of thermal image taken at z = 0.64m.

The local heat transfer coefficient was calculated at each FF thermocouple location using the local heat flux for each section, with heat losses included, and the associated wall-mean temperature difference. It is important to note that the heat transfer coefficient utilized to describe the heat transfer to the flow in the present work differs from the heat transfer coefficient used in other works. Sullivan & Sabersky [16] and Natarajan & Hunt [17], for example, calculated the

heat transfer coefficient using the difference between the wall temperature and the inlet flow temperature. This description of the heat transfer coefficient makes sense for Sullivan & Sabersky, as the length of the heated sections used were much smaller (<0.025m) than the lengths used in the present work (~1.3m). The flow through such a short heated length can be considered thermally-developing and the inlet temperature is a reasonable approximation of the mean flow temperature. Natarajan & Hunt, however, used heated sections up to 1.0m in length. Perhaps their reason for using the inlet temperature to describe the heat transfer coefficient lies simply in the difficult nature of experimentally measuring the mean flow temperature; no explanation for their choice was given. It is important to pay attention to these differences in the heat transfer coefficient definition when comparing the results from these works with the results from the present work.

2.1.3.1. Mean Temperature Calculation

The bulk mean flow temperature is an important quantity utilized throughout the present work. The mean temperature is used not only to calculate the heat transfer coefficient, but is also used to quantify the effective thermal properties of the flow (such as the specific heat and the thermal conductivity). It is standard practice [36] to define the bulk mean (or mixing cup) temperature of an internal flow as

$$T_m = \frac{\int_0^{R_i} \rho c_p(T) u_z(r) T(r) 2\pi r dr}{\int_0^{R_i} \rho c_p(T) u_z(r) 2\pi r dr} \tag{3}$$

where ρ represents the density of the flow, $c_p(T)$ represents the temperature-dependent specific heat of the flow, $u_z(r)$ represents the radial distribution of the axial velocity component, $T(r)$ represents the radial temperature distribution, and R_i represents the inner radius of the tube.

Experimental studies found in the literature and discrete element method (DEM) simulations performed by my colleague provided guidance in understanding the flow mechanics

of our particulate flows and the associated effect on flow properties. It has been shown both experimentally [37] and with DEM simulations [38], [39] that vertical dense granular flows through cylindrical tubes demonstrate an essentially uniform velocity profile across the tube, with a thin shear layer a couple particle diameters thick. Chilamkurti & Gould [38] found that the velocity profiles can be well represented by a Gaussian-shaped profile, with the form $u_z(r) = Ae^{-\left(\frac{r-B}{Y}\right)^2} + Z$, where A, B, Y, and Z are constants that depend on the tube diameter and flow rate. The velocity profiles for the flow rates tested experimentally in the present study were obtained from the DEM simulations and used to calculate the mean flow temperature. The resulting mean temperatures calculated using the Gaussian profiles varied minimally from the mean temperatures calculated assuming a plug flow with a velocity equal to the centerline velocity. Thus, our analysis treated the flows as plug flows for simplification. A similar assumption was utilized by Sullivan & Sabersky [16] and Natarajan & Hunt [17] in their studies of particulate flows through a vertical chute.

The average packing fraction of the flows, as measured from the DEM simulations, was observed to decrease by less than 6% from the static bed values measured (see Section 2.2.1 for static bed measurements). The bulk density of the flow was therefore assumed to be equivalent to the bulk density of a static bed of particles and constant across the radius of the tube. Incorporation of a temperature-dependent specific heat (see Section 2.2.2) yielded an increase in the calculated mean temperature of less than 1.5%; therefore, the temperature-dependency was neglected in the mean temperature calculation.

As previously mentioned, a thermocouple probe was traversed across the radius of the tube to obtain a radial temperature distribution. An analytic solution to the case of a plug flow subjected to a constant wall heat flux boundary condition yields a radial temperature profile quadratic in

shape. A quadratic regression matched the data well and was therefore used to represent the radial temperature distribution, $T(r)$. Incorporating the assumptions discussed into Equation 3, the expression for the mean temperature can be reduced to

$$T_m = \frac{C_1}{2} R_i^2 + \frac{2C_2}{3} R_i + C_3 \tag{4}$$

where C_1, C_2, and C_3 represent the coefficients of the quadratic temperature profile.

2.1.3.2. Wall Temperature Calculation

The temperature of the tube wall at the location of the mean temperature measurement is another important quantity used in the characterization of the heat transfer to the flow. The wall temperature was determined using two approaches. The first approach involved clamping a thermocouple to the tube wall at the same axial location as the FF thermocouples. A hole was drilled in the clamp to allow the FF thermocouple probes to enter the tube. The second approach involved interpolating the wall temperature at the desired axial location using a regression fit to the wall temperature data. The measured wall temperature distributions in the fully-developed region demonstrated an essentially linear trend. A linear least squares regression was therefore fit to the data and used to determine the wall temperature at the correct axial location. The two approaches yielded relatively similar values, with differences up to 2%. The wall temperatures determined using the first approach were utilized in the calculation of the local heat transfer coefficients whenever possible. The second approach was implemented when the wall thermocouple broke and no direct temperature data was available at that particular axial location. The second approach was primarily used for the high temperature measurements, as the thermocouples broke more often due to higher temperatures and moving parts (discussed in

Chapter 5). To avoid disrupting the apparatus by taking off insulation, a broken thermocouple was not immediately replaced if all other wall thermocouples were still operating properly.

The wall temperatures determined using both approaches represent the wall temperature on the outside of the tube; however, the temperature on the inside of the tube wall was desired to calculate the local heat transfer coefficient. The temperature on the inside of the tube wall was calculated based on the thermal resistance of the wall and the input wall heat flux. A thermal conductivity value of 14.5 W/m-K was assumed for the Inconel tube wall [40].

2.1.3.3. Nusselt Number Calculation

Since the Nusselt number is a standard non-dimensional number used to characterize the heat transfer from a heated surface to a flow, the Nusselt number of the particulate flows was also of interest. The Nusselt number provides a generalized way of comparing the heat transfer to a flow for a variety of system parameters. The Nusselt number (Nu) for the present flows was calculated based on the bulk effective thermal conductivity (k_b) and the inner tube diameter (D_i) according to

$$Nu = \frac{hD_i}{k_b} \tag{5}$$

Apart from its ability to compare the heat transfer across the different system configurations (as defined in Table 2.1), the Nusselt number was also used to examine the significance of the discrete nature of the flow on the heat transfer from the wall to the flow. A continuum plug flow through a tube subjected to a constant wall heat flux yields a closed form solution for the Nusselt number of the form

$$Nu = \frac{8}{1-8\sum_{j=1}^{\infty}\frac{\exp\left(-4\lambda_j^2 z^*\right)}{\lambda_j^2}} \tag{6}$$

$$z^* = \frac{(z/D_i)}{Pe_D} = \frac{zk_b}{m'' D_i^2 c_p} \quad (7)$$

where z^* represents the inverse Graetz number, λ_j represents the j^{th} eigenvalue, Pe_D represents the Péclet number based on tube diameter, and m'' represents the mass flux of the flow, defined by the cross-sectional area of the inside of the tube. Closer examination of Equation 6 shows that the Nusselt number converges to a constant value of 8 in the thermally-developed region (i.e. when $z^* \to \infty$) [41]. Ideally, if the discrete nature of the flow is insignificant, the Nusselt numbers calculated for the particulate flows should follow a similar trend to that of Equation 6. The comparison of the two will be discussed in detail in Section 2.3.

2.2. Material & Thermal Properties of a Static Bed

The flows utilized were composed of ceramic particles of two different varieties. The particle materials were selected by our partner institution, RTI International, in order to best meet the goals set forth by our ARPA-E funded project. The material and thermal properties of the particle material, as well as the properties of a bed of particles, were of interest to help characterize and understand the heat transfer to the flows. The following sections introduce the two types of particles used and the measurement of a variety of material and thermal properties.

2.2.1. Material Properties

The particles used for the majority of the experiments were a zirconia-silica particle obtained from Saint Gobain (ER-120). Three different batches of these particles were obtained, each with a different range of particle diameters. Scanning electron microscopy (SEM) was used to examine the sphericity of the particles, surface roughness, and the range of particle diameters

present. As seen in Figure 2.4, the particles are mostly spherical, with marginal surface roughness. The mean particle diameter measured for each batch can be seen in Table 2.2.

The density of the particle material was measured by placing a known mass of particles into a known volume of water. The amount of water displaced by the particles, determined by examining the change in volume of the water, indicated the volume of the particles, from which the density of the particles could be determined.

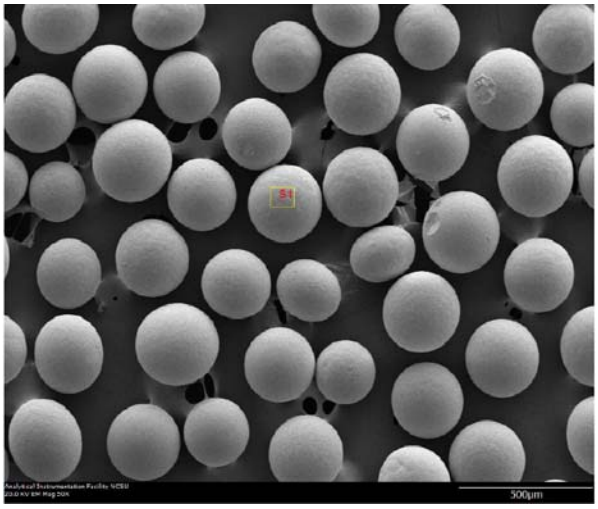

Figure 2.4: SEM image of the zirconia-silica particles.

The bulk density of a bed of particles was determined by measuring the mass and volume of a beaker of particles. The packing fraction of the static bed could then be determined using

$$\phi = \frac{\forall_{part}}{\forall_{total}} = \frac{\rho_b - \rho_g}{\rho_{part} - \rho_g} \tag{8}$$

where $\forall_{part}$ represents the volume of particles, $\forall_{total}$ represents the total volume, ρ_b represents the bulk (or total) density of the bed, ρ_g represents the density of the interstitial gas, air, and ρ_{part} represents the density of the particles. The density of the particles (3800 kg/m^3) was much greater than the density of air (1.2 kg/m^3); therefore, Equation 8 can be simplified to $\phi = {\rho_b}/{\rho_{part}}$. The resulting material properties can be seen in Table 2.2. The bulk density, and therefore packing

fraction, measured for each particle diameter were approximately the same; therefore, they were reported as the same value. This is expected for a monodisperse bed of particles, as the packing fraction is independent of the particle diameter. Since the degree of polydispersity is relatively small for each particle diameter tested, similar packing fractions make sense.

Table 2.2: Material properties of ceramic particles and static beds.

Particle Material	**Mean Particle Diameter, d_p (μm)**	**Particle Density, ρ_{part} (kg/m^3)**	**Bulk Density, ρ_b (kg/m^3)**	**Packing fraction**
Zirconia-silica	140	3801	2386	0.63
	270			
	320			
Alumina-silicate	340	3237	2006	0.62

A second batch of ceramic particles, selected due to their lower cost point, were tested and compared with the zirconia-silica particles. The second batch of particles were an alumina-silicate variety (75% Al_2O_3, 11% SiO_2, 9% Fe_2O_3) obtained from Carbo Ceramics (ID50 model). SEM was again used to examine the sphericity and roughness of the particles, as well as the mean particle diameter. As seen in Figure 2.5, the particles are more irregularly shaped compared with the zirconia-silica particles and have a slightly rougher texture.

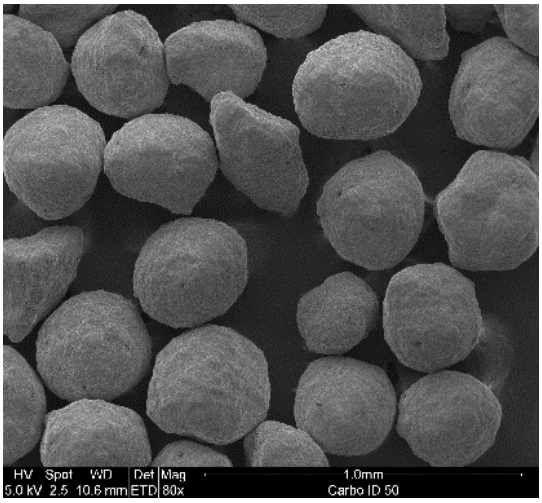

Figure 2.5: SEM image of the alumina-silicate particles.

The mean particle diameter was similar to that of the largest zirconia-silica particles. The density of the particles and the bulk density and packing fraction of a static bed were measured using the same techniques described above. As noted in Table 2.2, the alumina-silicate particles possessed a lower density, but similar packing fraction.

2.2.2. Specific Heat

A Differential Scanning Calorimeter (DSC) was obtained from TA Instruments (model Q20) to measure the heat flow through a small particle bed. The three-sample test, as defined in ASTM E1269-11, was used to determine the specific heat of the particle bed. The specific heats of the zirconia-silica and the alumina-silicate particles were measured over a temperature range from 40 to 500°C, as seen in Figure 2.6 below.

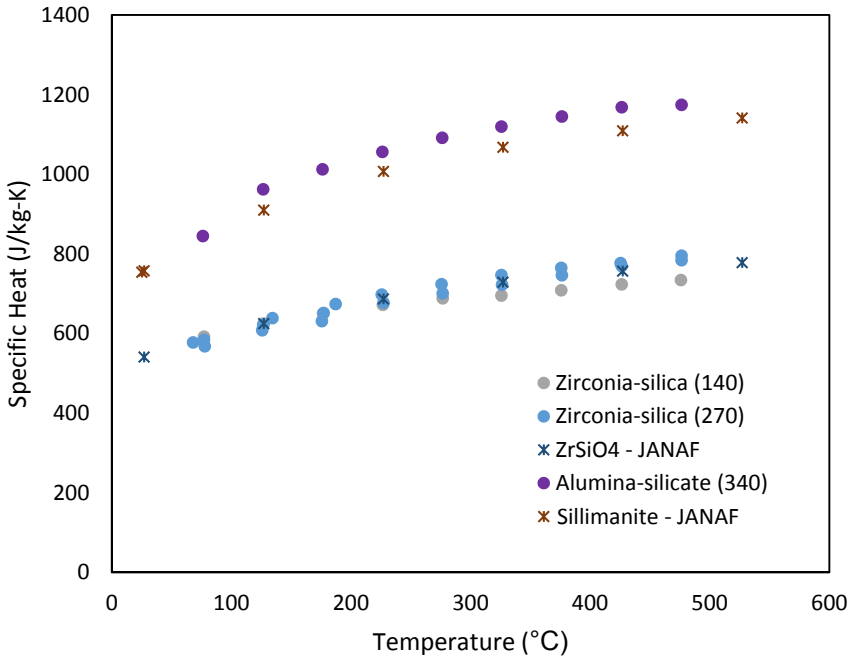

Figure 2.6: Specific heats of static particle beds. Numbers in parentheses denote particle diameter.

The effect of particle diameter on the measured specific heat of a particle bed was examined by measuring the values for beds composed of the 140 and 270μm zirconia-silica particles. The particle diameter appeared to have little effect on the specific heat values measured (for the range of particle diameters tested). This makes sense since the packing fraction for each particle diameter was essentially the same. The results from each particle type were compared with specific heat values listed in the NIST JANAF Thermochemical Tables [42] for similar materials. Since the volumetric heat capacity of air is significantly less than the volumetric heat capacity of the particles (~2000x less), the specific heat of a particle bed should be similar to the specific heat for the solid material. The zirconia-silica particle bed yields similar values to those listed in the JANAF tables for zirconium-silicate ($ZrSiO_4$). The results for the alumina-silicate particles are slightly greater than the values listed in the JANAF tables for sillimanite, an aluminum-silicate variety (63% Al_2O_3, 37% SiO_2). The differences most likely result from differences in the material composition.

An expression to estimate the specific heat of a particle bed at a given temperature was of interest for characterizing the heat transfer to the flow. A power-law expression was found to best represent the temperature-dependency of the specific heat. Table 2.3 summarizes the specific heat of the static particle beds.

Table 2.3: Specific heats of static particle beds.

Particle Material	**Bulk Specific Heat**	
	Temp-dependent (T in °C)	**@ 25°C (J/kg-K)**
Zirconia-silica	$271.5T^{0.1719}$	472
Alumina-silicate	$403T^{0.1762}$	711

2.2.3. Thermal Conductivity

The effective thermal conductivity of a static particle bed is an important parameter, as it provides insight into the physics of the heat transfer within a particulate bed and helps characterize

the heat transfer to the flow. The thermal conductivity measurements were made using two instruments: an apparatus designed in-house that can achieve bed temperatures up to 700°C (referred to as the "concentric tube apparatus") and an off-the-shelf unit from TA instruments with a maximum temperature limit of 300°C. The development of the concentric tube apparatus, the measurement principles, and the results from the two instruments will be discussed. The results will also be compared with effective thermal conductivity models found in the literature.

2.2.3.1. Concentric Tube Apparatus

An apparatus (Figure 2.7) to measure the effective thermal conductivity of a particle bed was designed using the principles of steady state heat conduction. The setup consists of a stainless steel tube (63.5mm OD) with a 1000W cartridge heater (12.7mm OD, 203.2mm long) positioned along the axis of the tube, creating an annulus between the two. The bottom of the tube was filled with approximately 50.8mm of ceramic insulation to minimize heat losses through the bottom. Four type K thermocouples, with wire diameters of 0.127mm, were threaded through two-hole ceramic insulators (0.794mm in diameter) and mounted to the bottom of the tube. The thermocouples were 101.6mm long, allowing the thermocouple beads to measure the temperatures at the midpoint of the tube length. The thermocouples were mounted in two pairs; each pair was positioned at a different circumferential position, with each thermocouple at a different radial location. Since the thermocouple beads were positioned far from the ends of the tube, the heat was assumed to flow predominately in the radial direction at the measurement location.

The tube was first filled halfway with particles, as seen in Figure 2.7c. The radial positions of the thermocouple beads were then measured using a scale. Finally, the remaining half of the tube was filled with particles and pieces of insulation were placed on the top. During the filling

process, the tube was tapped at regular intervals, in an attempt to create a relatively dense packing. Studies have shown that the degree of packing effects the heat transfer within a bed; looser packings display reduced effective thermal conductivities as compared with denser packings [9], [43]. Therefore, in an attempt to create similar packings for each experimental trial, the tube was tapped at regular intervals.

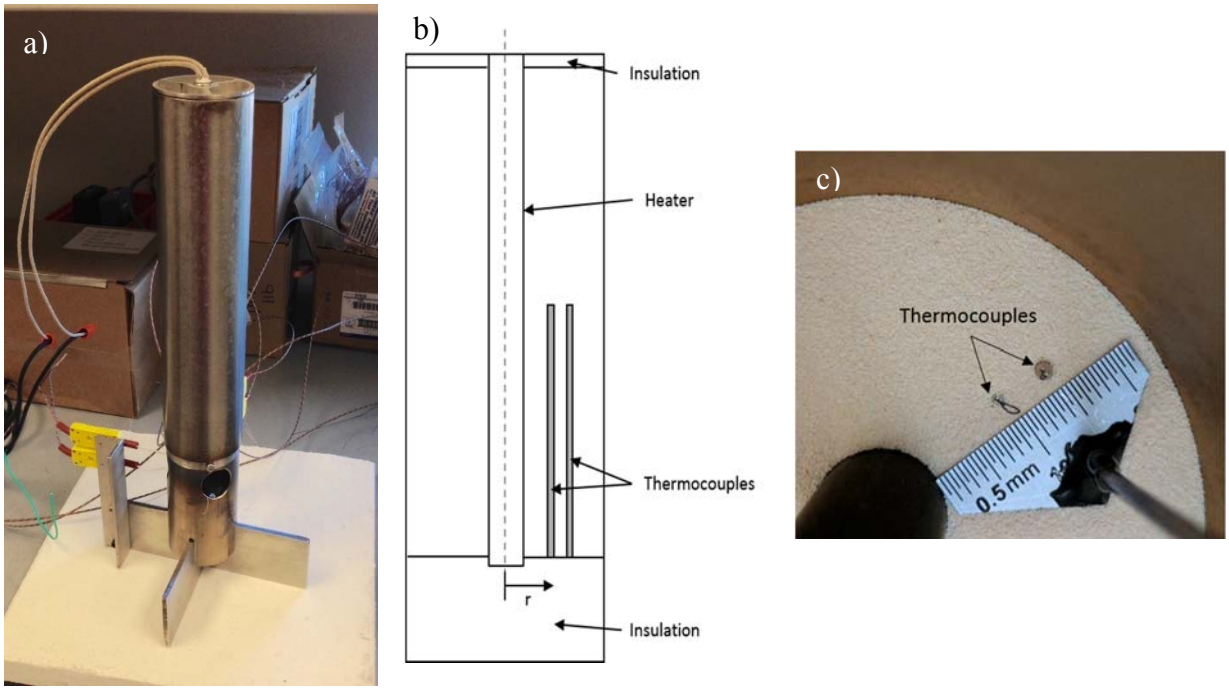

Figure 2.7: a) Image and b) schematic of the concentric tube apparatus designed in-house; c) cross-sectional view of the thermocouple locations within the particle bed.

Power to the cartridge heater was supplied by a 150V power supply (BK Precision XLN15010). The voltage supplied to the heater was controlled manually and the resulting current sourced to the heater was recorded by the power supply. The steady state solution to the heat conduction equation for an annulus subject to a constant wall heat flux at R_{in} and a constant temperature at R_{out} yields a temperature profile of the form

$$T(r) = \frac{VI}{2\pi L_H k_b} \ln(r/R_{in}) + T_{out} \tag{9}$$

where V represents the voltage potential, I represents the current supplied, L_H represents the length of the heater, T_{out} represents the temperature at R_{out}, and k_b represents the thermal conductivity of the particle bed. A logarithmic regression was fit to the measured temperature profile and the thermal conductivity was extracted using

$$k_b = \frac{VI}{2\pi L_H a_b} \tag{10}$$

where a_b represents the coefficient from the logarithmic regression. The calculated thermal conductivity was reported at the average bed temperature. The resulting thermal conductivity values are reported in Figure 2.8 for all particle variations. The effective thermal conductivity values measured by Carbo Ceramics for the alumina-silicate particles are also included. The ETCs measured using the CT apparatus show good agreement with the values measured by Carbo Ceramics, which were performed using ASTM C 1113.

It is important to note that a single particle bed was used to test the ETC for the 320μm particles and the alumina-silicate particles, whereas three separate particle beds were created to test the 270 and 140μm particles. Each time a new bed was created, a new packing resulted and the thermocouple positions were re-measured. The variation observed in the results for the 270 and 140μm particles most likely results from the variation in the packing fraction between different experimental trials, as well as the uncertainty in the measured radial positions for each trial. It is also important to note that at the higher temperatures, the temperature range spanned across the annulus reached up to 200°C. Recall that the thermal conductivity was assumed constant in Equation 9. This assumption seems invalid at the higher temperatures, as the trends displayed in Figure 2.8 suggest a variation in the thermal conductivity across this temperature range. To validate the trend developed from the values calculated assuming constant thermal conductivity, the radial temperature profile obtained from the solution of the heat conduction equation with a

variable thermal conductivity was studied. Incorporation of the linear trend observed in Figure 2.8 demonstrated comparable agreement with the temperature profiles measured. Therefore, the trends observed in Figure 2.8 were assumed to be accurate and were used throughout the rest of the study.

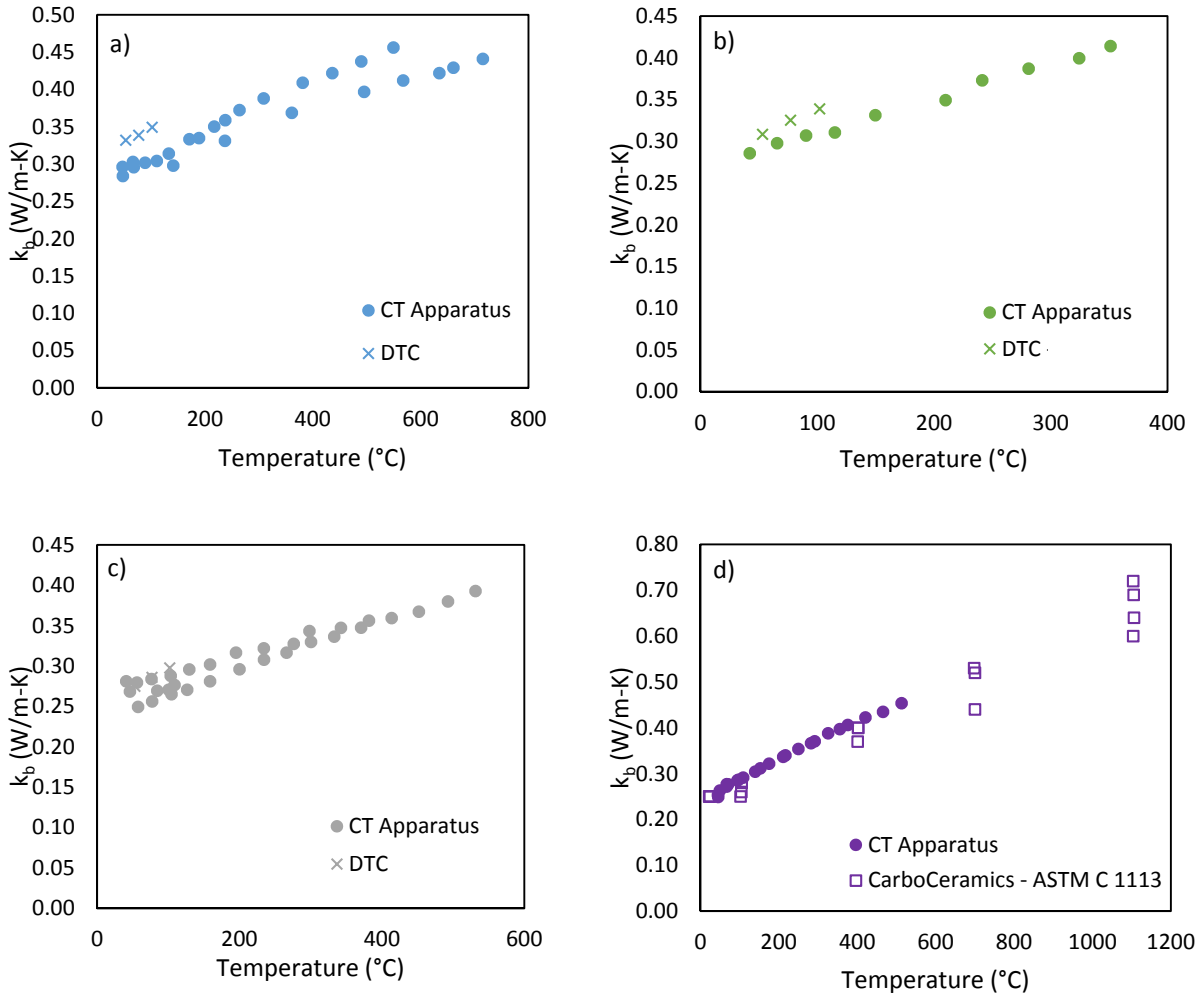

Figure 2.8: Experimentally measured effective thermal conductivities of static particle bed for a) 270µm, b) 320µm, and c) 140µm zirconia silica particles and d) 340µm alumina-silicate particles as a function of average bed temperature.

The experimental results demonstrate an increase in the effective thermal conductivity with increasing temperature for all particle materials and particle diameters tested. Linear regressions were fit to each data set and used to interpolate ETC values at different temperatures; the resulting regressions are summarized in Table 2.4.

Table 2.4: Effective thermal conductivities of static particle beds.

Particle Material	Mean Particle Diameter (μm)	Effective Thermal Conductivity (W/m-K) w/ T in °C	Range (°C)
Zirconia-silica	140	$0.000264T + 0.252$	40 < T < 600
	270	$0.000248T + 0.287$	40 < T < 700
	320	$0.000371T + 0.281$	40 < T < 350
Alumina-silicate	340	$0.000425T + 0.244$	40 < T < 520

The effect of particle diameter on the ETCs measured for the zirconia-silica particles is examined in Figure 2.9 below. The 140μm particles yield slightly lower thermal conductivities than the 270 and 320μm particles; however, the variation is within the experimental uncertainty in many cases.

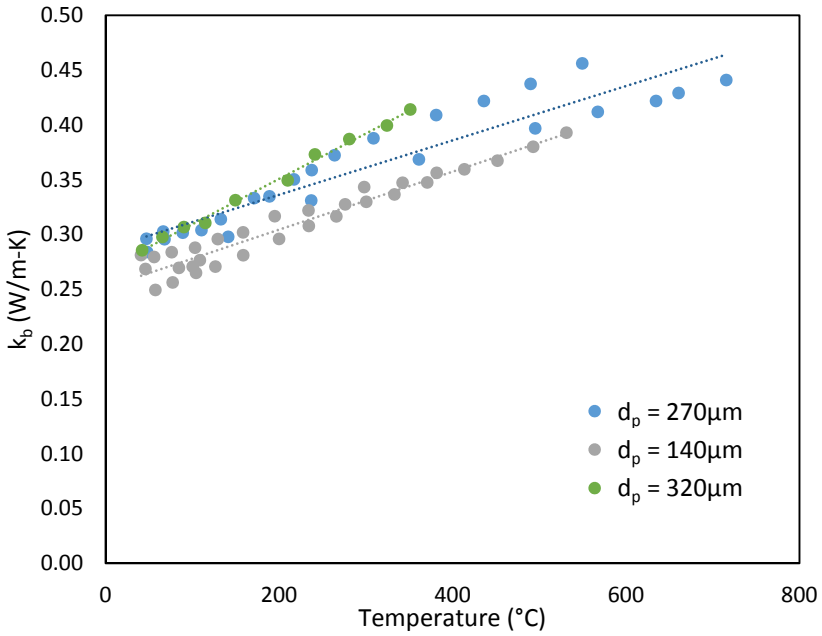

Figure 2.9: Effect of particle diameter on the effective thermal conductivity of a static particle bed.

The linear regressions fit to each data set are also depicted in Figure 2.9. Three distinct trends emerge for each particle diameter, with varying slopes and relative magnitudes. The variation in packing fraction between the prepared particle beds may partly explain the variation

in the trends observed for different particle diameters. The different temperature ranges sampled for each particle diameter may also influence the resulting trends. According to the model developed by Van Antwerpen et al. [44], the thermal conductivity is essentially independent of particle diameter at low temperatures; particle diameter has a stronger influence at higher temperatures due to the presence of radiation. The Van Antwerpen et al. model is discussed in more detail in Section 2.2.3.3.

2.2.3.2. Direct Thermal Conductivity Apparatus

The effective thermal conductivity of a particle bed was also characterized with a DTC-300 Direct Thermal Conductivity (DTC) apparatus from TA Instruments for comparison with the concentric tube apparatus. The DTC consists of two heated plates, between which the sample specimen is placed. A heat flux transducer located within the lower plate measures the induced heat flow across the sample. The thermal conductivity of the sample is then calculated based on the sample thickness. The particle bed is enclosed within a specimen cell, which consists of two brass plates and an insulating ring (Figure 2.10). Due to the high thermal conductivity of the brass plates compared with the particle sample, the temperature within the brass is assumed constant and the sample thickness is considered solely that of the particle bed. When creating a particle sample, the bed was gently shaken to create a denser sample (similar to the tapping used when filling the concentric tube apparatus).

Figure 2.10: DTC specimen cell.

It is important to observe the differences between the measured effective thermal conductivity values from the concentric tube and DTC apparatuses. The concentric tube apparatus measures the effective thermal conductivity of a bulk bed, with no effects from wall boundaries. In contrast, the DTC results are effected by the presence of two wall boundaries from the two brass plates. As discussed in Chapter 1, the packing of particles near a wall is more ordered, yielding lower packing fractions as compared with the random packing of particles in the bulk of a bed, and therefore reduced heat transfer. To compare the results from the two apparatuses, the thermal conductivity of the bulk bed was extracted from the thermal conductivity measured by the DTC. The particle bed associated with the DTC sample was modelled as a series of three thermal resistances: two resistances associated with the particle layer adjacent to the wall and a resistance associated with the bulk of the bed. It is common in the literature to assume that the wall contact resistance has a thickness of half a particle diameter. This approach was adopted in the present work as well. The total thermal resistance of the sample specimen was then determined according to

$$R_{total}(t_{total}) = \frac{t_{total}}{k_{total}} = \frac{1}{k_b} t_{total} + d_p \left(\frac{1}{k_{wa}} - \frac{1}{k_b} \right) \tag{11}$$

where R_{total} represents the total thermal resistance of the sample, k_{total} represents the effective thermal conductivity of the DTC sample, t_{total} represents the total thickness of the sample, and k_c represents the effective thermal conductivity of the wall-adjacent layer (thickness of $0.5d_p$). A series of sample specimen were created, each with a different thickness; a linear regression was fit to the resulting thermal conductivity values, in the form of Equation 11, and used to extract the bulk and wall-adjacent layer thermal conductivities from the regression coefficients. The resulting bulk thermal conductivities can be seen in Figure 2.8. The values measured with the DTC are

slightly higher than those measured using the concentric tube apparatus, but lie within the range of experimental uncertainty.

2.2.3.3. Comparison with Models in the Literature

Throughout the past century, many attempts have been made to model the effective thermal conductivity of a static particle bed. A plethora of models exist, ranging in complexity, from simple models dependent on one or two parameters (such as packing fraction and material thermal conductivities) to detailed models that incorporate mechanical properties, particle roughness, etc. These models were compared with the experimental results displayed in Figure 2.8 to verify the trends observed.

In an attempt to capture the temperature-dependency of the ETC, which was particularly important for the high temperature flow measurements (discussed in Chapter 5), a model that incorporated all modes of heat transfer was desired. The multi-sphere unit cell model developed by Van Antwerpen et al. [44] was the primary model implemented, as it provides a thorough description of each heat transfer mode. Unlike many of the other models in the literature, which depend solely on the packing fraction of the particle bed, Van Antwerpen et al. attempt to account for the packing structure of the particle bed by incorporating the coordination number and the contact angle.

Regardless of complexity, all models require knowledge of the thermal conductivities of both the interstitial gas and the particle material. Room temperature values for zirconium-silicate ($k = 2.1$ W/m-K) [45] and sillimanite ($k = 1.76$ W/m-K) [46] were available in the literature. Incorporation of these values in the Van Antwerpen et al. model showed good agreement with the experimentally measured values at approximately room temperature. Temperature-dependent

thermal conductivity data obtained for sillimanite from the CRC Materials Science and Engineering Handbook [46] displays a decrease in thermal conductivity with increasing temperature. Incorporation of this data into the Van Antwerpen et al. model, however, resulted in poor agreement with the experimental data at higher temperatures. Temperature-dependent thermal conductivity data was not, on the other hand, readily available for zirconium-silicate. The temperature-dependency of the zirconia-silica particles was therefore approximated from the trend observed for zirconia (ZrO_2), the material most similar to zirconia-silica with available temperature-dependent data. The temperature-dependent thermal conductivity data available for zirconia [47] demonstrated a slight increase in thermal conductivity with temperature; a quadratic regression best captured this trend. As a first approximation, the y-intercept of the regression was modified to depict the room temperature thermal conductivity of zirconium silicate. This modified regression was incorporated into the model developed by Van Antwerpen et al. [44] for the thermal conductivity of the particles. The model captured the thermal conductivity trend displayed by the experimental data for low temperatures; however, the model underestimated the effective thermal conductivity at higher temperatures.

In an attempt to capture the increase in ETC with temperature displayed by the experimental results, the material thermal conductivity was approximated by minimizing the difference between the values measured and the values predicted by the Van Antwerpen model. MATLAB's built-in optimization functions were used to determine the material thermal conductivity within the temperature range of the experimental measurements. This process was performed using the experimental data from each particle diameter; the optimized values from each particle diameter were averaged to approximate the thermal conductivity of the zirconia-silica

solid. A quadratic regression best fit the temperature-dependent trend displayed by the optimized zirconia-silica solid.

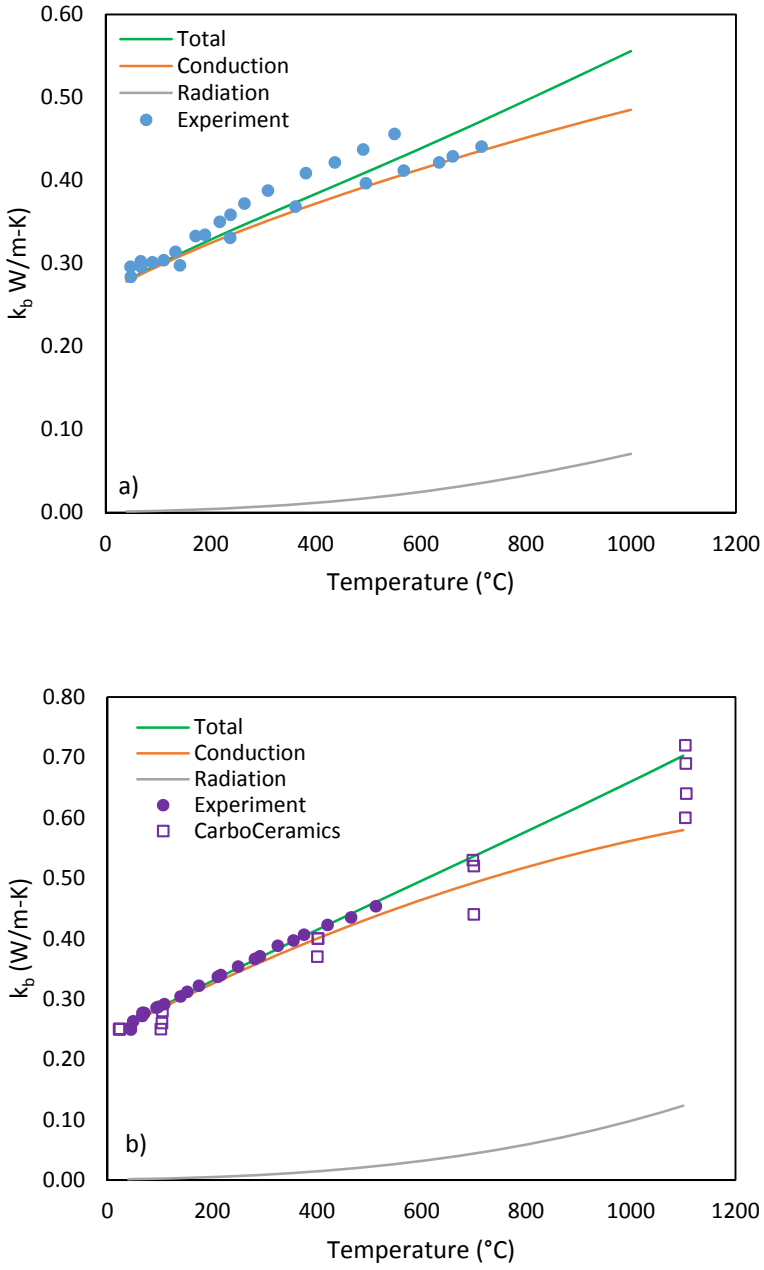

Figure 2.11: Bulk effective thermal conductivity as a function of temperature for the a) 270µm zirconia-silica particles and b) the 340µm alumina-silicate particles. Solid lines denote values calculated using the Van Antwerpen et al. [44] model. Circles denote experimentally measured values.

A similar technique was used to estimate the thermal conductivity of alumina-silica. In contrast to the decreasing trend reported for sillimanite, the optimized alumina-silica thermal conductivity displayed a slight increase in thermal conductivity with temperature. The difference between the two may result from the difference in material composition; in particular, the presence of iron oxide in the alumina-silicate particles may alter the thermal conductivity from that of sillimanite. A linear regression best fit the temperature-dependent trend displayed by the optimized alumina-silicate solid. The regressions were incorporated into the Van Antwerpen model and used to estimate the bulk ETCs at temperatures up to 1100°C (Figure 2.11). Note that the emissivity of the particles was assumed to be 0.8.

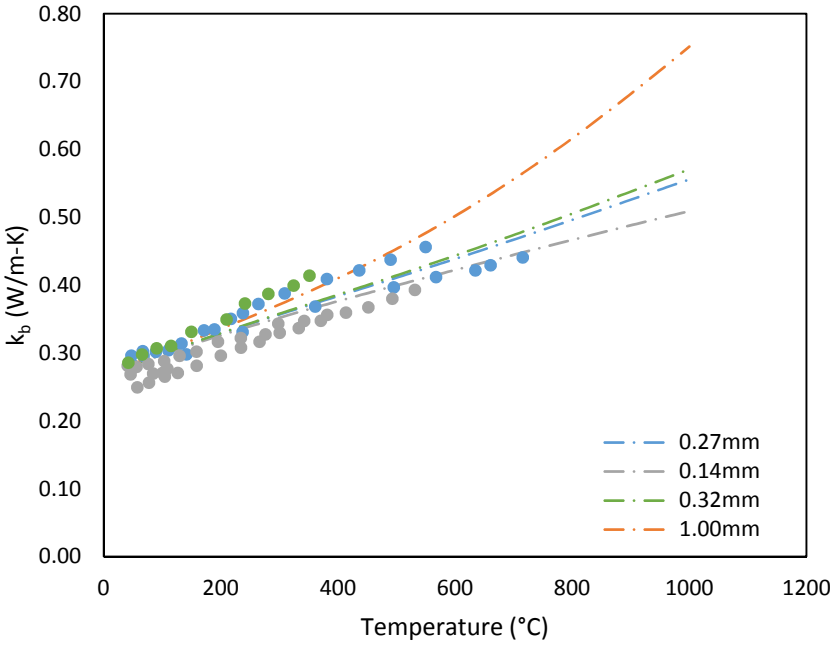

Figure 2.12: Variation in bulk effective thermal conductivity with temperature and particle diameter for zirconia-silica particles. Circles denote experimentally measured values, lines denote values predicted by Van Antwerpen model.

The contribution of conduction and radiation to the total ETC calculated using the Van Antwerpen model is also displayed in Figure 2.11. The radiation contribution becomes more

significant at temperatures greater than approximately 600°C; however, it is clear that conduction is the primary heat transfer mode for the particle beds studied. The radiation contribution plays a much larger role in the total heat transfer as the particle diameter increases; the radiation contribution begins to surpass the conduction contribution for particle diameters greater than approximately 2mm. The effect of particle diameter on the heat transfer through a static particle bed, as predicted by the Van Antwerpen model, can be seen in Figure 2.12.

As previously mentioned, the effective thermal conductivity is independent of particle diameter at low temperatures; as the temperature increases, however, and the contribution from radiation increases, the larger particles begin to display superior heat transfer capabilities. While the packing fraction of a bed is independent of the particle diameter, the relative size of the void spaces increases with increasing particle diameter. As a result, radiation is able to penetrate further, as compared with a smaller particle.

2.3. Low Temperature Results

The radial temperature distributions obtained from all test cases were relatively quadratic in shape. Examples of the radial temperature distributions obtained for the 9.5mm OD tube with the 270μm zirconia-silica particles at two different flow rates can be seen in Figure 2.13. Each temperature displayed is the average of all the samples collected at the given radial position. In general, each temperature was sampled approximately 40 times. The wall temperature measured at the corresponding axial position is also displayed in Figure 2.13, denoted by the '×' above each curve. The coefficient of determination associated with each profile across all experiments was greater than 0.97. As expected, the temperature increases with axial position and the faster flow

rates yield a steeper temperature profile. In both cases, a slight profile is observed at the inlet of the heated section due to axial conduction through the tube wall.

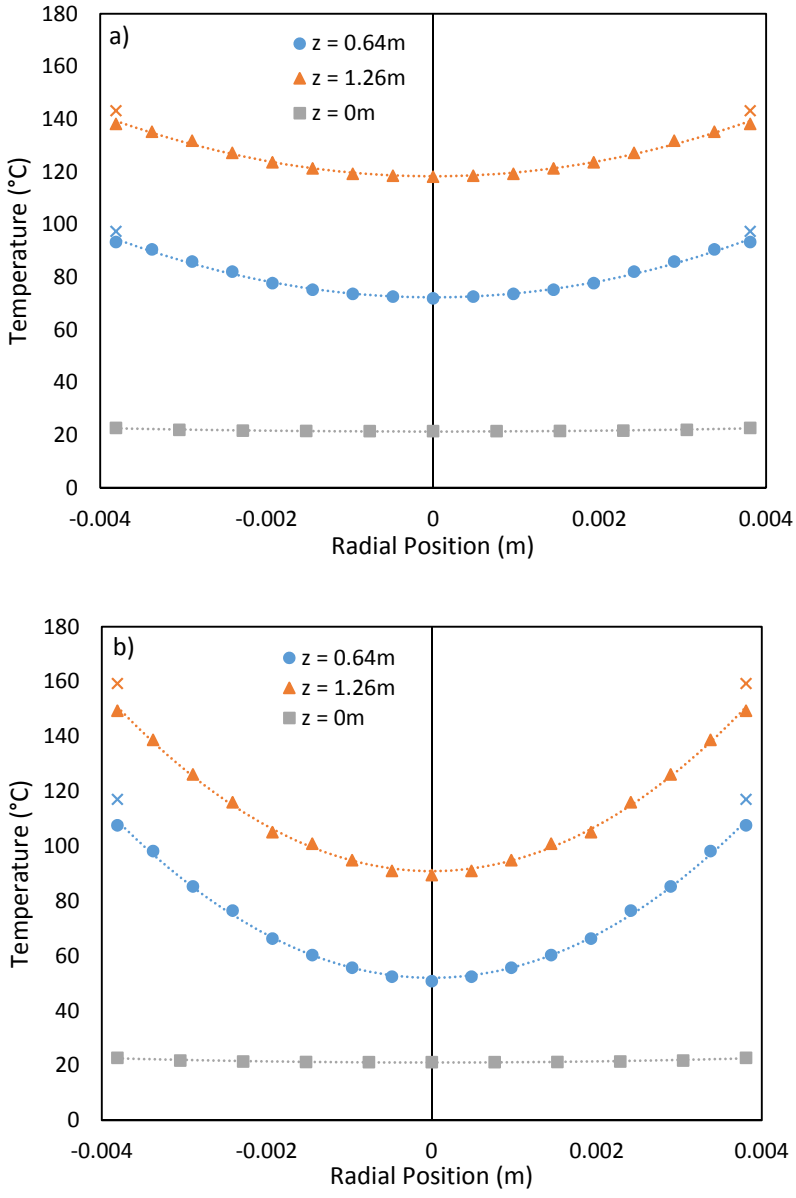

Figure 2.13: Radial temperature profiles for 270µm zirconia-silica particles in the 9.5mm OD tube at a) 0.015m/s and b) 0.047m/s. Solid shapes denote experimental data, dashed lines denote quadratic regression, and '×' denotes wall temperature.

Note that the wall temperature measured is greater than the flow temperature measured at the wall. The observed magnitude of the temperature jump is greater for the faster flow rate due to

the higher heating power applied. Recall that the mean flow temperatures were maintained constant across all tests; a higher heat input was required to achieve the same temperatures at faster flow rates. The wall temperature jump observed at the wall most likely results from the discrete nature of the flow, relating to the increased thermal contact resistance discussed by many in the literature. The effect of the wall on the heat transfer to the dense flows of the current study will be investigated more thoroughly in subsequent chapters.

The mean temperature values calculated for the temperature profiles displayed in Figure 2.13 are plotted at their corresponding axial positions in Figure 2.14. The resulting wall temperature distribution is also displayed. The wall temperature distribution displays features characteristic of an internal flow subject to a constant wall heat flux. The rate of increase in the temperature with axial position is approximately constant for $z > 0.34$m; the rate of temperature increase varies, however, between the inlet and $z = 0.34$m. These trends correspond to the thermally-developed and the thermal entrance regions of an internal flow.

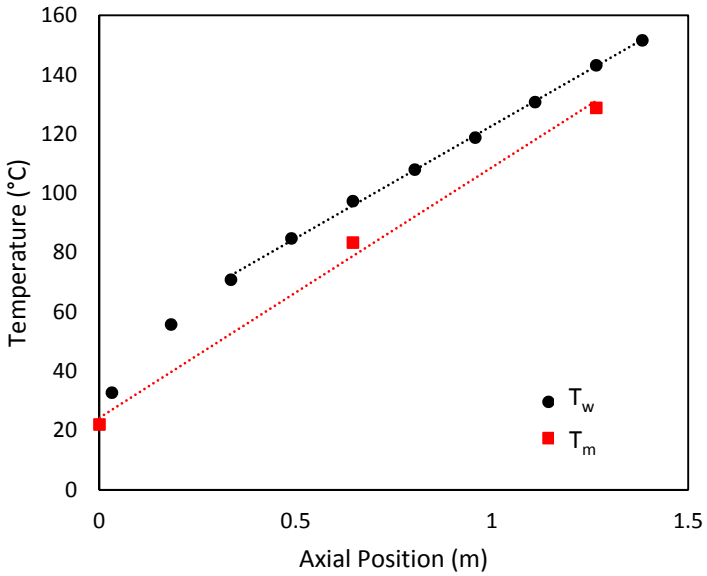

Figure 2.14: Axial wall and mean temperature distributions for 270µm zirconia-silica particles in the 9.5mm OD tube at 0.015m/s. Dashed lines denote linear regression.

Note that the length of the entrance region varies with flow rate. For all the cases tested in the present study, both fluid flow thermocouples were positioned within the thermally-developed region; at the fastest flow rates, the thermal entrance region appears to approach the FF thermocouple probe at z = 0.64m. Typically, for low temperature flows in which the temperature drop across the length of the tube is small, the thermal properties of the flow are assumed constant. In this case, the wall and mean temperatures increase at similar rates in the thermally-developed region. The mean temperature distribution displayed in Figure 2.14 displays a slightly larger slope than the wall temperature distribution. Across all cases tested, the slopes differed by up to 11%. The variation from standard low temperature flows observed results from the variation in the thermal properties of the flow and the variation in the wall heat flux along the length of the tube. Since the electrical resistivity of the tube increases with increasing temperature and therefore increasing axial position, the heat flux supplied to the flow increases with increasing axial position.

As a sanity check, the mean temperatures calculated using the radial temperature profiles were compared with the mean temperatures predicted by the 1st Law of Thermodynamics. The axially-dependent heating power was incorporated to obtain a more accurate comparison with the experimental data. The axially-dependent heating power was estimated by examining the variation in the electrical resistance of the tube with axial position:

$$\dot{Q}(z) = I^2 \int_0^z \frac{\rho_{elec}\big(T_w(z)\big)dz}{A_{tw}} \tag{12}$$

Here, A_{tw} represents the cross-sectional area of the tube wall and ρ_{elec} represents the electrical resistivity of the tube. The resistivity of the tube was assumed to vary linearly with temperature; an expression of the form $T_w(z) = cz^d + ez$ best captured the wall temperature distribution in both the thermally-developing and developed regions. Applying these assumptions to Equation 12 yields

$$\dot{Q}(z) = G_1 z^{d+1} + G_2 z^2 + G_3 z \tag{13}$$

where G_1, G_2, and G_3 are coefficients obtained by curve fitting with experimental data and d represents the exponent from the wall temperature distribution. Note that the curve fitting was performed using the heating powers that incorporated the heat losses through the insulation. The mean temperature as a function of axial position according to the 1st Law energy balance was calculated by implementing a power-law temperature-dependency for the specific heat, as described in Table 2.3 $\left(c_p = H_1 T^{H_2}\right)$, and inserting Equation 13:

$$T_{m,e}(z) = \left[\frac{(G_1 z^{d+1} + G_2 z^2 + G_3 z)(H_2+1)}{\dot{m} H_1} + T_{in}^{H_2+1}\right]^{1/(H_2+1)} \tag{14}$$

Here, $\dot{m}$ represents the mass flow rate and T_{in} represents the inlet temperature. Figure 2.15 compares the axial distribution of the mean temperatures calculated experimentally with the mean temperature distribution calculated using Equation 14.

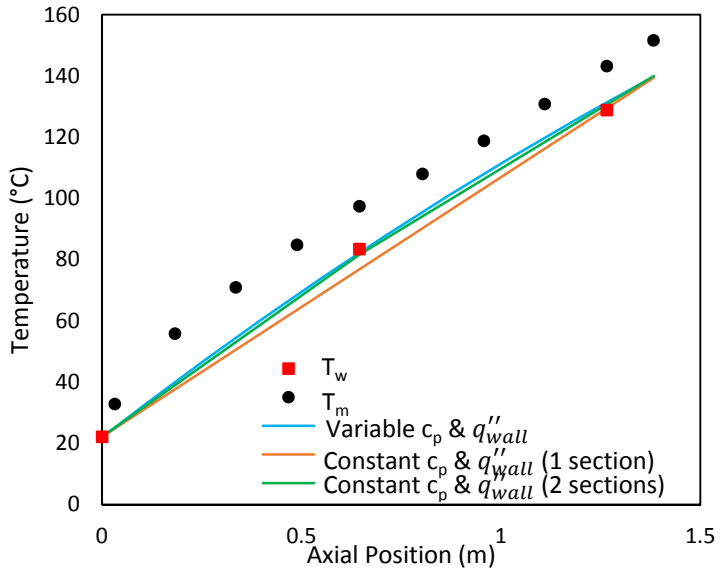

Figure 2.15: Comparison of mean temperatures calculated using an energy balance and experimental data (270µm Z-S particles, 9.5mm OD tube, 0.015m/s). Solid shapes denote experimental data; solid lines denote energy balance results.

The distribution resulting for a constant wall heat flux condition $\left(\dot{Q}(z) = q''_{wall} 2\pi R_i z\right)$ and constant specific heat is also displayed in Figure 2.15. Note that the tube was again divided into two sections (as demonstrated in Figure 2.1), with a constant heat flux and specific heat associated with each section. The specific heat was calculated at the average temperature of each section. For the low temperatures studied in this chapter, the mean temperatures calculated using both approaches (i.e. variable specific heat and wall heat flux vs. constant specific heat and wall heat flux) yield similar results. For comparison, the mean temperatures calculated without sectioning the tube into two parts are also displayed. Here, the specific heat was calculated at the average temperature across the tube length. The trend produced by this approach underestimates the mean temperatures in the mid-section of the tube. This suggests that the variation in the specific heat with temperature, and therefore axial position, is important to predict the mean temperature accurately. Recall that the specific heat of the particles increases more rapidly at lower temperatures (Figure 2.6); this trend manifests itself in a faster increase in mean temperature in the first section of the tube. The division of the tube into two sections is significant enough in this case, however, to adequately capture this trend. The mean temperatures calculated using the energy balance agree well with the experimentally calculated values, thereby confirming the validity of our mean temperature measurement approach.

The effect of flow rate and particle diameter on the heat transfer to the flow can be seen in Figure 2.16. The uncertainty associated with each measurement is presented in the form of error bars, which denote the 95% confidence interval. Appendix A summarizes the uncertainty calculations. The largest uncertainty is observed at the slowest flow rates (up to 14%); since slow flow rates demonstrate very small temperature gradients, the heat transfer coefficient (which is hyperbolic in nature) is more sensitive to variations in the temperature difference measured. Note

that the 140 and 320µm particles could not be tested at the faster flow rates due to the quantity of particles available.

All particles demonstrate a slight increase in heat transfer with increasing velocity; however, the large uncertainty makes it difficult to state this with certainty. The particle diameter appears to have negligible effect on the heat transfer to the flow for the range of particle diameters tested. Ideally, a wider range of particle diameters would have been tested to fully observe the effect of particle diameter (if there is one at low temperatures).

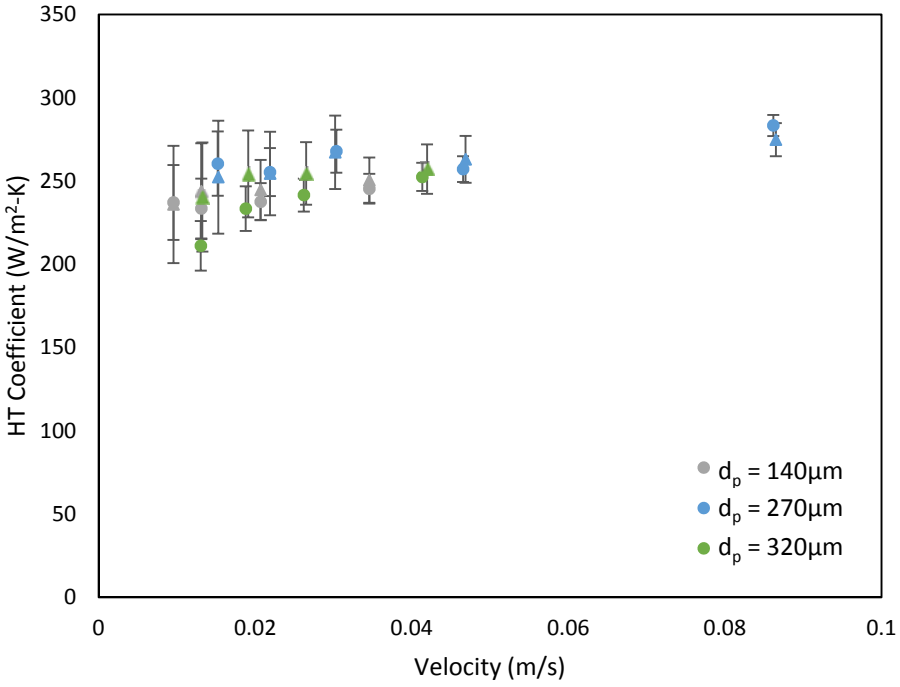

Figure 2.16: Heat transfer coefficients calculated for flows composed of zirconia-silica particles in the 9.5mm OD tube. '●' denotes value measured at z = 0.64m, '▲' denotes value measured at z = 1.26m. Error bars denote 95% confidence interval.

The effect of particle material on the heat transfer to the flow, as demonstrated by the 320µm zirconia-silica (Z-S) particles and the 340µm alumina-silicate (A-S) particles, can be seen in Figure 2.17. The error bars are not displayed to present a clearer picture of the data; however,

the uncertainty in the data for the alumina-silicate particles is similar to that of the zirconia-silica particles (up to 10% at the slowest flow rate). The two ceramic particles selected for the project demonstrate comparable heat transfer to the flow. Recall that the alumina-silicate particles were selected due to their lower cost-point than the zirconia-silica particles. The results displayed in Figure 2.17 suggest that the alumina-silicate particles would be more suited to concentrated solar power applications, as they contribute less to the overall cost of the CSP system. Similar to the zirconia-silica particles, the alumina-silicate particles demonstrate a slight increase in heat transfer with increasing flow rate, although again it is difficult to claim this with certainty due to the magnitude of the uncertainty in the measurement calculations.

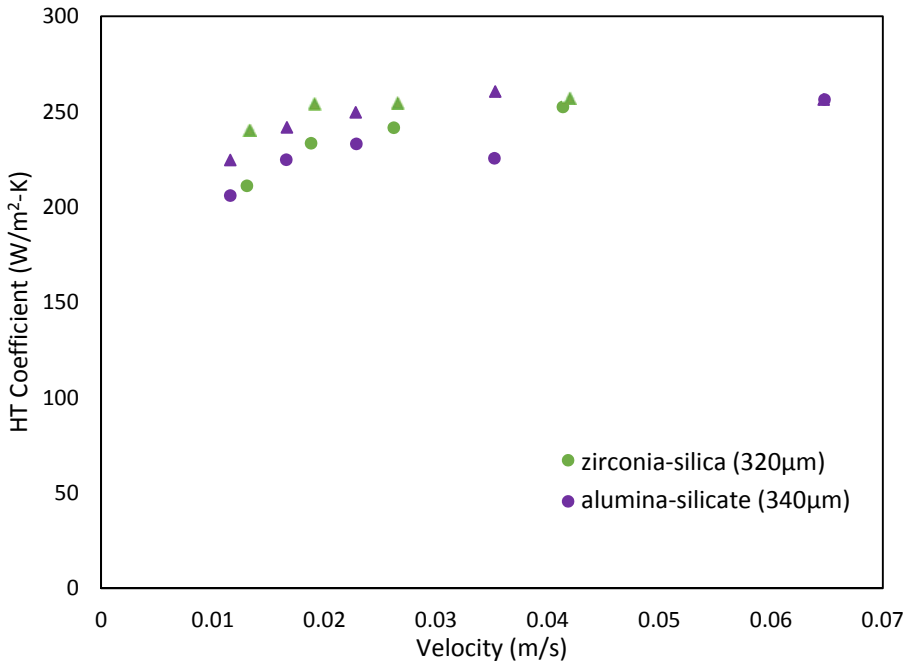

Figure 2.17: Heat transfer coefficients calculated for 320µm Z-S and 340µm A-S particles in 9.5mm OD tube. '●' denotes value measured at z = 0.64m, '▲' denotes value measured at z = 1.26m.

The effect of tube diameter on the heat transfer to the flow, demonstrated using the 270µm zirconia-silica particles, can be seen in Figure 2.18. The largest uncertainty for the 12.7mm OD

tube is also found at the slowest flow rate (up to 9%) and the heat transfer coefficient displays a slight increase with increasing flow velocity. As expected, the smaller tube diameter yields superior heat transfer coefficients.

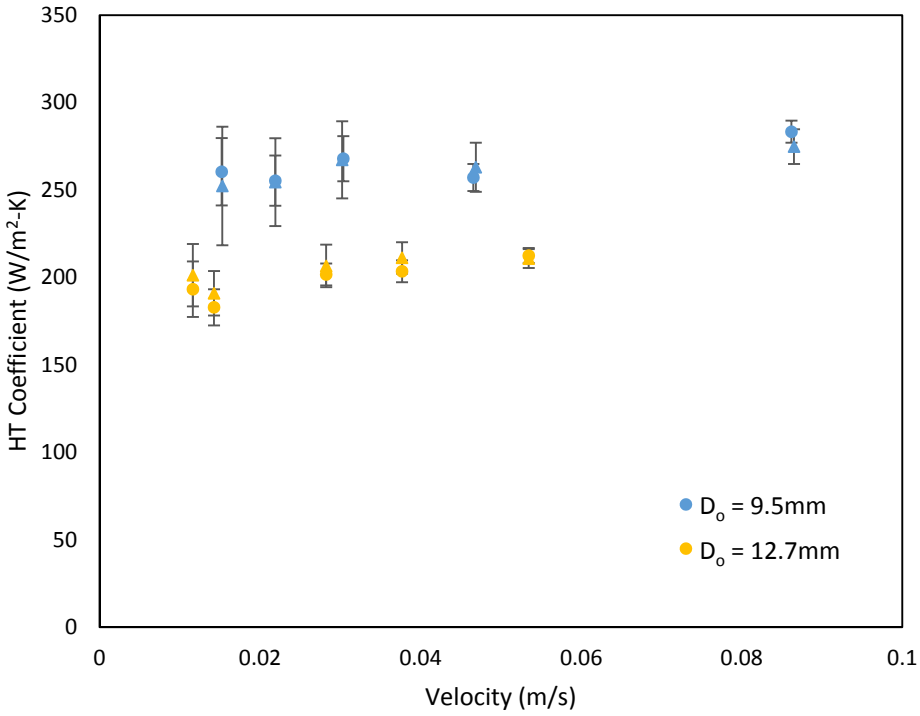

Figure 2.18: Heat transfer coefficients calculated for the 270µm Z-S particles in the 9.5 and 12.7mm OD tubes. '●' denotes value measured at z = 0.64m, '▲' denotes value measured at z = 1.26m.

A more interesting observation comes from the comparison of the Nusselt numbers calculated for each system configuration (Figure 2.19). The larger tube diameter yields higher Nusselt numbers than the smaller tube. It is well understood in continuum heat transfer that a thermally-developed flow demonstrates a constant Nusselt number, regardless of tube diameter, flow rate, or material. The deviation from this phenomenon for the current flows is interesting and will be discussed further in subsequent chapters. Another important observation is the deviation of the magnitude of the Nusselt number from the continuum solution. As mentioned in Section

2.1.3.3, an analytic solution to the problem of heat transfer to an internal flow subjected to a constant wall heat flux yields a Nusselt number of 8 in the thermally-developed region. The Nusselt numbers calculated for the dense granular flows yield values noticeably less than 8. Note that the uncertainty in the Nusselt numbers is greater than that in the heat transfer coefficients due to uncertainty in the bulk ETC measurements. Up to 16% relative uncertainty is observed in the Nusselt numbers calculated for all system configurations.

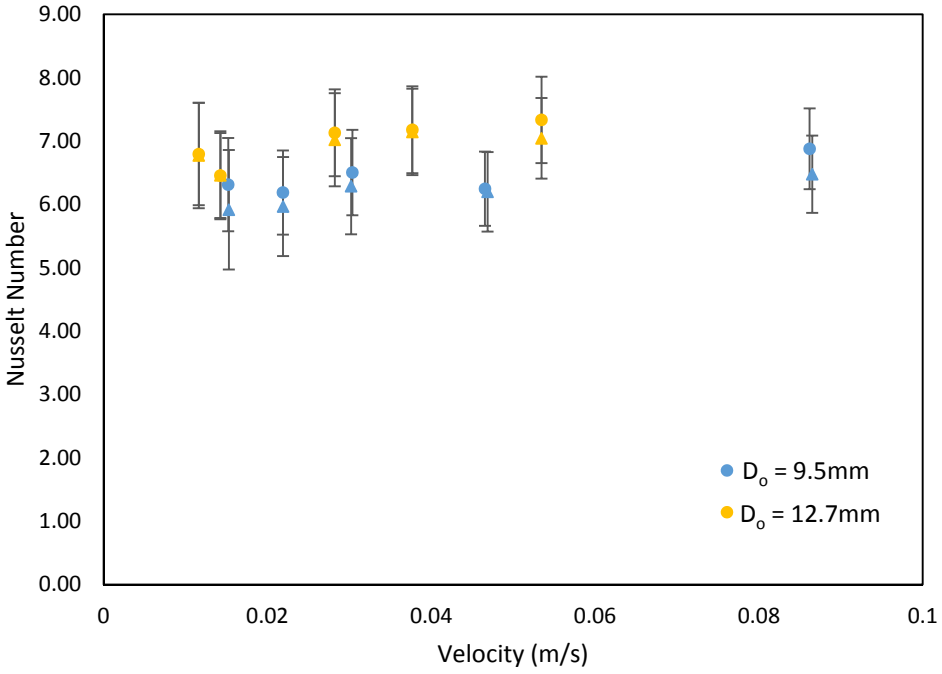

Figure 2.19: Nusselt numbers calculated for the 270µm Z-S particles in the 9.5 and 12.7mm OD tubes.

A common approach used to visualize the heat transfer to internal flows is to examine the Nusselt number as a function of the inverse Graetz number. The inverse Graetz number, defined as $z^* = \frac{(z/D_i)}{Pe_D}$, represents the non-dimensional axial distance. The experimental data from all five system configurations is plotted as a function of the inverse Graetz number in Figure 2.20. The continuum solution for a plug flow (Equation 6) is also plotted for comparison.

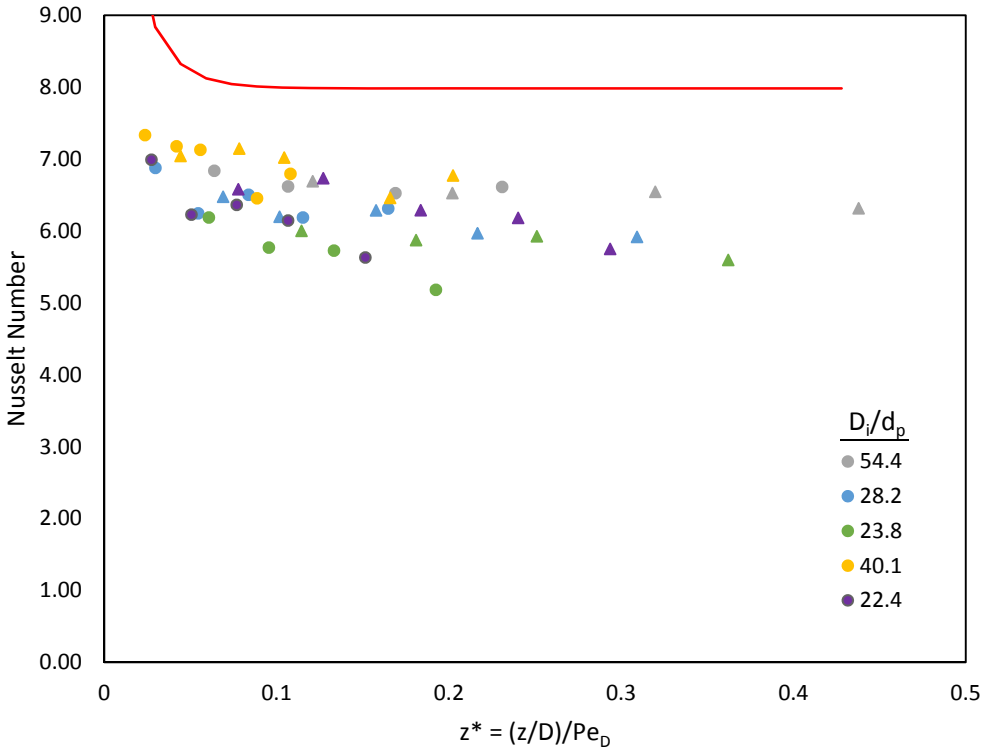

Figure 2.20: Nusselt number plotted as a function of inverse Graetz number for all system configurations. '●' denotes value measured at z = 0.64m, '▲' denotes value measured at z = 1.26m. Solid line denotes the plug flow continuum solution.

It is clear from Figure 2.20 that the discrete nature of the flows reduces the heat transfer from a heated wall to a flow. The scatter observed in the data results from both experimental uncertainty and the relative importance of the discrete nature of the flow. The following chapter investigates the effect of the discrete nature of the flow on the heat transfer in more detail.

Chapter 3

Two-Layer Model Development

A generalized heat transfer correlation to describe the heat transfer to vertical dense granular flows through cylindrical tubes was developed to better understand the underlying physics governing the heat transfer to the flow and to predict the heat transfer to different system configurations. The following sections discuss the derivation of an analytic model and the components incorporated to account for the discrete nature of the flow.

3.1. Analytic Solution to the Energy Equation

The importance of a wall on the heat transfer to a particulate bed is well documented. A common approach taken to model the heat transfer from a heated surface to a particulate bed is to divide the bed into two regions: a region that encompasses the majority of the bed (referred to as the bulk region) and a second region adjacent to the surface, with a thickness of a particle radius, that accounts for the variation in the heat transfer due to the more ordered arrangement of particles along a surface. A similar approach was taken to model the heat transfer to the flows studied in

the present work. The schematic in Figure 3.1 describes the two layers used to model the flow and their associated dimensions.

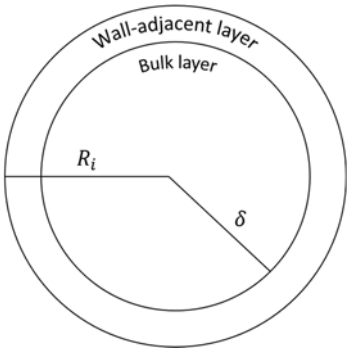

Figure 3.1: Schematic of regions used to model the dense flow.

An analytic solution was derived for a thermally-developed flow using the two-dimensional energy equation:

$$U\frac{\partial T_j(r,z)}{\partial z} = \frac{\alpha_j}{r}\frac{\partial}{\partial r}\left(r\frac{\partial T_j(r,z)}{\partial r}\right) \tag{15}$$

Here, T represents the temperature, U represents the flow velocity, α represents the thermal diffusivity, and subscript j denotes the j^{th} layer of the composite. Equation 15, which assumes a plug flow with constant thermal properties in each layer, was solved subjected to the following boundary conditions

$$T_b(r=0,z)\ is\ finite \tag{16}$$

$$k_{wa}\frac{\partial T_{wa}}{\partial r}\Big|_{r=R_i,z} = q''_{wall} \tag{17}$$

$$T_b(r=\delta,z) = T_{wa}(r=\delta,z) \tag{18}$$

$$k_b\frac{\partial T_b}{\partial r}\Big|_{r=\delta,z} = k_{wa}\frac{\partial T_{wa}}{\partial r}\Big|_{r=\delta,z} \tag{19}$$

$$T_b(r,z=0) = T_{wa}(r,z=0) = T_{in} \tag{20}$$

where k represents the thermal conductivity of each layer, δ represents the radius of the bulk layer and subscripts b and wa correspond to the bulk and wall-adjacent layers, respectively. The radius

of the bulk layer, as defined in Figure 3.1, is equivalent to $\delta = R_i - 0.5d_p$. For simplification, the density and specific heat were assumed the same in both the wall-adjacent and bulk layers. The derivation of the solution can be found in Appendix B. The solution of the thermally-developed problem results in the following Nusselt number correlation:

$$Nu_{k_b} = \frac{hD_i}{k_b} = \frac{8R_i^4}{\delta^4 + \frac{k_b}{k_{wa}}(R_i^4 - \delta^4)} \tag{21}$$

Examination of the above expression for a single layer (i.e. when $\delta = R_i$, $k_b = k_{wa}$) indicates that the Nusselt number converges to a constant value of 8, as expected for a thermally-developed plug flow subjected to a constant wall heat flux [41]. The expression for the radius of the bulk layer was inserted into Equation 21 to create a simplified Nusselt number correlation:

$$Nu_{k_b} = \frac{8}{W^4 + \frac{k_b}{k_{wa}}(1 - W^4)} \tag{22}$$

$$W = \left(\frac{\delta}{R_i}\right) = \left(1 - \frac{1}{(D_i/d_p)}\right) \tag{23}$$

Here, W is a new parameter defined to represent the ratio of the radii of the two layers; it depends only on the ratio of the tube-to-particle diameters. The ratio of the tube-to-particle diameters describes the relative importance of the curvature of the tube wall on the heat transfer through the wall-adjacent layer, as well as the relative size of the bulk layer. According to Legawiec & Ziolkowski [48], the heat transfer through the wall-adjacent layer for a static bed increases with the ratio of the tube-to-particle diameters due to an increase in packing fraction in the wall-adjacent layer. Note, also, that W is independent of temperature, but rather only depends on the system configuration. Therefore, according to Equation 22, the Nusselt number based on the bulk thermal conductivity depends only on the ratio of the bulk-to-wall-adjacent layer thermal conductivities for a given system configuration.

3.2. Effective Thermal Conductivity of Wall-Adjacent Layer

In order to compare our experimental results from Section 2.3 with the Nusselt number correlation described in Equation 22, an understanding of the wall-adjacent layer thermal conductivity is required. The effective thermal conductivity of the layer of particles adjacent to a wall has been studied for static beds of particles (for example[25], [44], [48]). On the other hand, while most of the works studying the heat transfer to dense granular flows have acknowledged the presence of an increased thermal resistance at the wall, they have failed to provide an in-depth understanding of the heat transfer from the surface through this wall-adjacent layer (for example [16], [17], [20]). They also fail to provide a means to estimate this thermal resistance. Sullivan & Sabersky [16], for example, incorporated an additional thermal resistance in their development of a model to describe the heat transfer to their flows, but simply chose an empirical parameter to represent this resistance to allow the model to fit the trends displayed by their experimental results. Denloye & Botterill [22] and Schlünder [21], on the other hand, utilized relations developed to describe the heat transfer through the wall-adjacent layer of static beds. Morris et al. [29] noted that static bed correlations, which are derived for densely packed beds, do not capture the intermittent nature of particle contacts in a flow. They developed a correlation to more accurately describe the heat transfer phenomenon at a wall boundary by incorporating a particle distribution function, which accounted for the variation in packing fraction adjacent to a wall in a flow. The resulting boundary condition correlation took the form of a 7^{th}-order polynomial expression, which described the Nusselt number of the wall-adjacent layer for flow down an incline and depended on the packing fraction of the wall-adjacent layer. Their ultimate goal was to develop a model to describe the near-wall heat transfer that could be utilized in numerical models for continuum flows.

In our study, we sought to characterize the underlying physics controlling the heat transfer from a heated wall to a vertical granular flow and develop a simple correlation to predict the resistance to the heat transfer, in the form of an effective thermal conductivity. The work of Legawiec & Ziolkowski [48] was used as a guide in the derivation of a thermal conductivity for the wall-adjacent layer. Since Legawiec & Ziolkowski were developing a correlation to describe the heat transfer through the wall-adjacent layer of a static particle bed, they assumed that all particles in the contact layer were in contact with the wall. The heat transfer to a single particle was analyzed, considering the heat transfer through both the interstitial gas and the particle. They assumed the particle had a point contact with the wall; therefore, any heat transfer through the contact area was neglected. The wall-adjacent layer effective thermal conductivity was then determined based on the number of particles in the wall-adjacent layer, assuming each particle demonstrated the single particle heat transfer.

For a flowing granular bed, such as our dense granular flows, the assumption that all particles in the wall-adjacent layer are in contact with the wall is no longer accurate. The DEM simulations performed by my colleague were used to examine the particle mechanics adjacent to the wall and how they varied with flow rate, inferring how the observed characteristics effect the heat transfer to the flow. In particular, the variation in the packing fraction in the wall-adjacent layer and the number of particles in contact with the wall as a function of the mean flow rate were of interest. As demonstrated by Morris et al. [29], the heat transfer to a single particle decreases significantly as soon as the particle loses contact with the wall. The thin layer of air between the wall and the particle acts as a layer of insulation, causing the heat transfer to the particle to drop noticeably. Therefore, it is important to account for the heat transfer to particles not in contact with the wall.

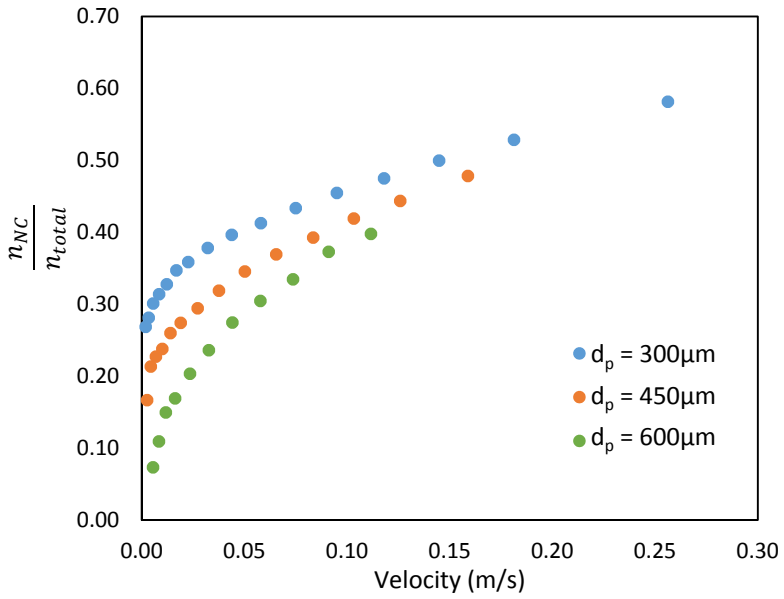

Figure 3.2: Fraction of the total wall-adjacent layer particles that are *not* in contact with the wall as a function of flow rate and particle diameter. Results for a 7.75mm ID tube.

Based on the DEM simulations, on average, 10-60% of the particles in the wall-adjacent layer are not in contact with the wall, depending on the flow rate, particle diameter, and tube diameter. An example of the variation in the fraction of particles not in contact with the wall (defined as the ratio of the number of particles not in contact with the wall to the total number of particles in the wall-adjacent layer) with flow rate is displayed in Figure 3.2. It is clear that the flow rate has a significant effect on the contact behavior of the particles.

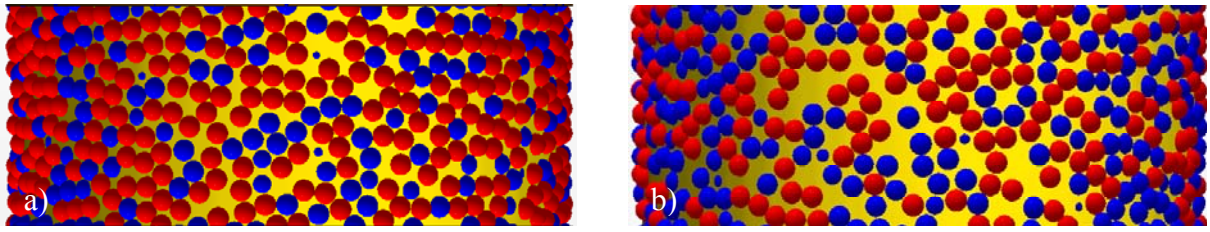

Figure 3.3: Particle arrangements in wall-adjacent layer for mean flow velocities of a) 0.023m/s and b) 0.25m/s (using 7.75mm ID tube and 300µm particles). Red particles denote particles in contact with the wall, blue particles denote particles not in contact with the wall, and yellow denotes void spaces.

Figure 3.3 provides a visual understanding of the particle arrangement in the wall-adjacent layer at different flow rates. The red particles in Figure 3.3 represent particles in contact with the wall, while the blue particles represent particles not in contact with the wall, and the yellow represents void spaces where no particle is present. These images emphasize the fact that the number of particles in contact with the wall decreases with increasing flow rate. It should also be noted that the amount of void space (yellow) increases with increasing flow rate, resulting in a reduced packing fraction at faster flow rates. These observations suggest that the heat transfer to the flow should decrease with increasing flow rate. This phenomenon was captured in the model developed to describe the heat transfer in the wall-adjacent layer.

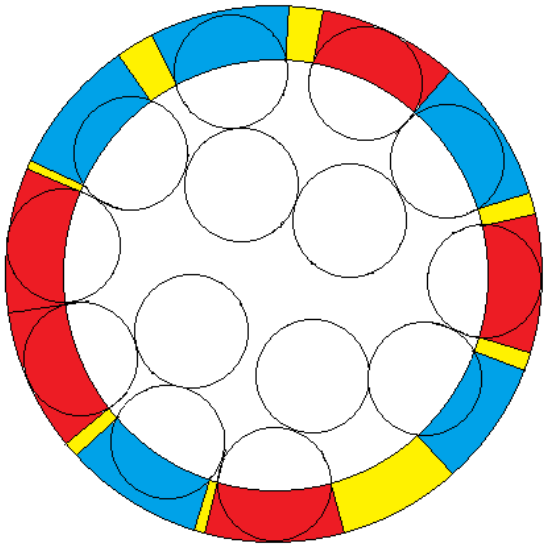

Figure 3.4: Depiction of thermal resistances used to model wall-adjacent layer heat transfer. Red denotes resistance considered for contact particles, blue denotes resistance for particles not in contact, and yellow denotes resistance for void spaces.

The model developed assumes that the heat transfer through the wall-adjacent layer is composed of three thermal resistances: a resistance due to particles in contact with the wall (R_C), a resistance due to particles not in contact with the wall (R_{NC}), and a resistance due to void spaces

where no particle is present (R_{void}). Figure 3.4 depicts each of these thermal resistances, with the sum of each color representing the total thermal resistance of each type. The three resistances are acting in parallel, therefore the total resistance to heat transfer through the wall-adjacent layer is described by

$$\frac{1}{R_{wa}} = \frac{1}{R_C} + \frac{1}{R_{NC}} + \frac{1}{R_{void}} \tag{24}$$

$$R_{wa} = \frac{\ln(R_i/\delta)}{k_{wa}} \frac{R_i}{A_{total}} \tag{25}$$

$$R_C = \frac{\ln(R_i/\delta)}{k_C} \frac{R_i}{A_C N_C} \tag{26}$$

$$R_{NC} = \frac{\ln(R_i/\delta)}{k_{NC}} \frac{R_i}{A_{NC} N_{NC}} \tag{27}$$

$$R_{void} = \frac{\ln(R_i/\delta)}{k_{void}} \frac{R_i}{A_{void}} \tag{28}$$

Here, R_{wa} represents the total thermal resistance of the wall-adjacent layer due to conduction, k_C, k_{NC}, k_{void}, and k_{wa} represent the thermal conductivities for a particle in contact with the wall (a single red block in Figure 3.4), a particle not in contact with the wall (a single blue block in Figure 3.4), the void spaces, and the wall-adjacent layer, respectively. A_C and A_{NC} represent the areas of the tube wall considered in the calculation of the heat transfer to a single particle in contact with the wall and not in contact with the wall, respectively, A_{void} represents the area of the tube wall where the heat transfer is purely through the interstitial gas, A_{total} represents the total area of the tube wall under consideration and N_C and N_{NC} represent the number of particles in contact with the wall and not in contact with the wall in the area under consideration, respectively. The thermal conductivity of the void spaces (k_{void}) is equivalent to the thermal conductivity of the interstitial gas (k_g). The area of wall subject to heat transfer through the void spaces is determined based on the total area of the tube wall "covered" by particles, both with and without contact:

$$A_{void} = A_{total} - N_C A_C - N_{NC} A_{NC} \tag{29}$$

Equations 24-29 were rearranged to solve for the wall-adjacent layer thermal conductivity:

$$k_{wa} = k_{void}(1 - n_C A_C - n_{NC} A_{NC}) + k_C n_C A_C + k_{NC} n_{NC} A_{NC} \tag{30}$$

Here, n_C and n_{NC} represent the number of particles with and without contact per unit wall area, respectively. To simplify the problem, all the particles not in contact with the wall were assumed to be at the same distance from the wall, yielding two groups of particles: those in contact with the wall and those at a distance ar_p from the wall (where r_p represents the particle radius). According to Equation 30, many parameters are required to characterize the heat transfer through the contact layer. The projected area of a single particle on the tube wall ($A_{contact}$ and A_{NC}) was determined based on geometry. The number of particles in contact with the wall per unit wall area (n_C) was obtained from the DEM simulations. The number of particles not in contact with the wall per unit wall area (n_{NC}) was determined based on the packing fraction of the wall-adjacent layer (ϕ_{wa}) and n_C, where the packing fraction was obtained from DEM simulations. The expression for the packing fraction of the wall-adjacent layer was utilized to find the number of particles not in contact with the wall:

$$\phi_{wa} = \frac{2A[\forall_C n_C + \forall_{NC} n_{NC}]}{r_p(2A-1)} \tag{31}$$

Here, $\forall_C$ and $\forall_{NC}$ represent the volume of a single particle in the wall-adjacent layer for both particles in contact with the wall (assuming a point contact) and those particles a distance ar_p from the wall, and A represents the tube-to-particle diameter ratio $\left(A = D_i/d_p\right)$. The volume of a single particle in the contact layer was determined based on geometry.

The thermal conductivity for a single particle (both k_C and k_{NC}) was derived using an approach similar to that used by Legawiec & Ziolkowski [48]. The heat transfer from the wall to the edge of the contact layer (δ) consists of heat transfer through the interstitial gas and the solid

particle. The total thermal resistance can then be represented by connecting the associated thermal resistances in series. Initially, the thermal conductivities were calculated for the cylindrical tube system studied in the present work; the resulting solutions, however, could not be reduced to a simple algebraic expression (see Appendix C). Legawiec & Ziolkowski obtained a simplified expression by deriving the solution for a flat wall and incorporating correction factors to account for the curved surface of a cylindrical wall. A similar approach was employed in the present work. Using Figure 3.5 as a guide, the infinitesimal resistances for the gas and solid can be represented by

$$dR_g = \frac{D_g(r)}{k_g 2\pi r dr} = \frac{(1+a)r_p - \sqrt{r_p^2 - r^2}}{k_g 2\pi r dr} \tag{32}$$

$$dR_s = \frac{D_s(r)}{k_s 2\pi r dr} = \frac{\sqrt{r_p^2 - r^2} - ar_p}{k_s 2\pi r dr} \tag{33}$$

where k_s represents the thermal conductivity of the solid particle material and r represents the radial position as defined in Figure 3.5.

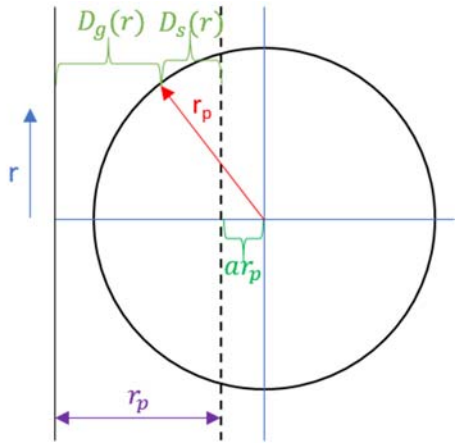

Figure 3.5: Schematic of single particle in wall-adjacent layer of flat plate.

The total thermal conductivity for a single particle can then be calculated by integrating the sum of the resistances for $0 \leq r \leq r_p\sqrt{1-a^2}$, yielding

$$k_{particle} = \frac{2k_g}{(1-a^2)}\left(\frac{K}{K-1}\right)^2\left[\frac{a(K-1)+K}{K}\ln\left(\frac{K}{aK+1-a}\right) - \frac{(1-a)(K-1)}{K}\right] \quad (34)$$

Here, K represents the ratio of the solid-to-gas thermal conductivities $\left(K = k_s/k_g\right)$. Inserting Equations 31 and 34 into Equation 30, letting $a = 0$ for k_C, the effective thermal conductivity of the wall-adjacent layer can be written in its simplified form, with the correction factors implemented:

$$k_{wa} = k_g\left\{1 + \pi r_p^2 n_C\left(1+\frac{1}{A}\right)[2\Phi_C - 1] + \frac{\left(1+\frac{1.35}{A}\right)}{(1-a)^2(2+a)}\left[3\left(1-\frac{0.5}{A}\right)\phi_{wa} - 2\pi r_p^2 n_C\right]\left(2\Phi_{NC} - (1-a^2)\right)\right\} \quad (35)$$

$$\Phi_C = \left(\frac{K}{K-1}\right)^2\left[\ln K - \frac{(K-1)}{K}\right] \quad (36)$$

$$\Phi_{NC} = \left(\frac{K}{K-1}\right)^2\left[\frac{a(K-1)+K}{K}\ln\left(\frac{K}{aK+1-a}\right) - \frac{(1-a)(K-1)}{K}\right] \quad (37)$$

The correction factors utilized approximately capture the variation in the projected area of a single particle on the wall for a curved wall compared with a flat wall and the change in the volume of a single particle enclosed in the wall-adjacent layer for a cylinder versus a flat plate. The thermal conductivities for a single particle (k_C and k_{NC}) were essentially the same for the cylinder and flat plate cases (varying by less than 1.5%). The largest variation is observed for small tube-to-particle diameter ratios, where the effect of curvature is greatest.

3.2.1. Flow Parameters

The effective thermal conductivity of the contact layer can be determined using Equations 35-37; however, an understanding of the number of contact points, the contact layer packing fraction, and the average distance of "no contact (NC)" particles from the wall is required. A series of DEM simulations were performed with StarCCM+ using two different tube diameters and three

different particle diameters to examine how these parameters (n_C, ϕ_{wa}, a) varied with particle diameter, tube diameter, and flow rate. Each of the six system configurations was tested using up to 15 different flow rates, ranging from creeping ($U = 0.002\ m/s$) to the upper limit of choked flow (which varies for each system configuration). The centroids of all particles were tracked at each time step, for a total of 1000 time steps, and used to calculate the packing fraction in the wall-adjacent layer, the number of particle-wall contacts at a given instant, and the average distance of particles from the wall; the parameter values reported are time-averaged values. Table 3.1 summarizes the system configurations and their corresponding tube-to-particle diameter ratios.

Table 3.1: DEM system configurations implemented to characterize the flow behavior in the wall-adjacent layer.

D_i/d_p	Tube Diameter, D_i (mm)	Particle Diameter, d_p (μm)
25.8	7.75	300
17.2	7.75	450
12.9	7.75	600
36.4	10.92	300
24.3	10.92	450
18.2	10.92	600

Figure 3.6a displays the variation of the packing fraction in the wall-adjacent layer with flow rate as a function of particle diameter. For mean flow velocities greater than approximately 0.02m/s, the packing fraction decreases with increasing flow rate; below 0.02m/s, the packing fraction increases slightly with increasing flow rate. The decrease in packing fraction observed agrees with the observation made in Figure 3.3. The behavior observed at slow flow rates is curious; however, since our work primarily focused on the dense flow regime, we have not further investigated the slow flow rate behavior.

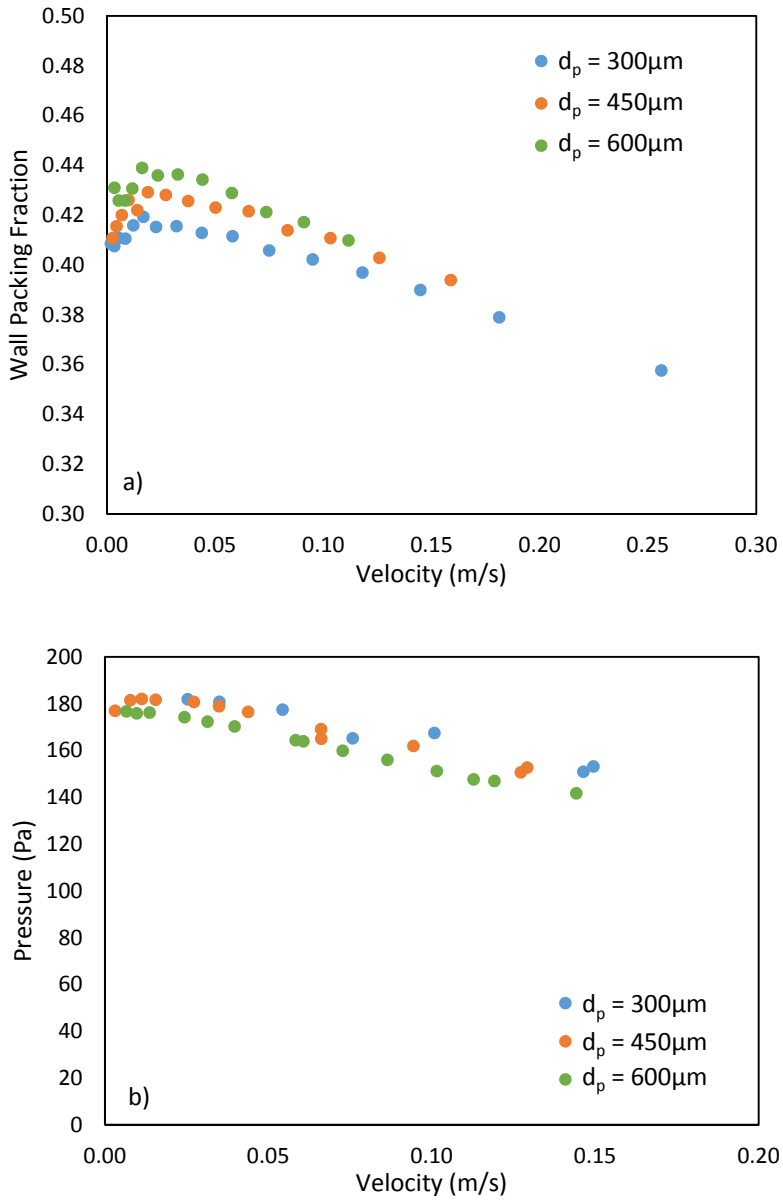

Figure 3.6: Variation in the a) contact layer packing fraction and b) pressure with mean flow velocity as a function of particle diameter (using 7.75mmID tube). Note that the y-axis scale of (a) does not start at zero.

The variation in pressure within the tube may be one possible explanation for the decrease in packing fraction observed with increasing flow velocity. Using DEM simulations, my colleague studied the variation of pressure within the tube [38]. An increase in pressure with increasing depth below the hopper was observed, saturating to a constant value, termed the saturation pressure. This

observation agreed with the experimental investigations of Janssen [49]. The pressure inside the tube may manifest itself by pushing particles against the wall. A higher pressure thus results in a greater force with which the particles are pushed against the wall, forcing the particles to fill in the available void spaces near the wall, thereby increasing the packing fraction in the wall-adjacent layer. The variation in pressure with flow velocity for different particle diameters is plotted in Figure 3.6b. The pressure decreases with increasing flow rate, which is similar to the trend observed in the wall-adjacent layer packing fraction. The pressure, however, does not capture the trend observed in the particle diameter. Further research into the trends observed in the flow mechanics was outside the scope of the present study, however future work should strive to understand the mechanisms controlling the behaviors observed. Since the DEM simulations were validated in our previous work [38], we trust the results obtained and used them to understand the heat transfer phenomenon.

The packing fraction results for all system configurations and flow rates greater than 0.02m/s (dense regime) were used to develop an empirical correlation that can be used to predict the packing fraction for different system configurations and mean flow velocities. The correlation that best captures the trends observed takes the form of

$$\phi_{wa} = 0.43 - \frac{2}{3A^2} - \left(0.003 + \frac{1}{4A}\right)\frac{U}{\sqrt{g d_p}} \tag{38}$$

where U represents the average flow velocity and g represents the gravitational acceleration. The correlation agrees with the simulation results for all flow rates (including slow velocities) within 5%.

The variation in the number of contacts with flow rate for various particle diameters can be seen in Figure 3.7. The number of particle-wall contacts per unit wall area were normalized using the maximum number of possible contacts so the effect of particle and tube diameter could

be compared. The maximum number of possible contacts, based on the optimal packing along a cylindrical wall (using the equations for a column of spheres [50]), can be approximated well for $A > 4$ by assuming a hexagonal packing of particles along the inner tube wall. The assumption of a hexagonal packing along the wall for $A < 4$ overestimates the number of contacts. However, since this is such a small range of tube-to-particle diameter ratios, and not the range under consideration, the hexagonal packing of particles was utilized. The maximum number of possible contacts was therefore defined as:

$$n_{C,max} = \frac{(1-1/A)}{2\sqrt{3}r_p^2} \tag{39}$$

For all system configurations, the number of contacts decreases with increasing flow rate. This may result partially from an increased "mean free path" of particles in the axial direction at faster flow rates. In general, the normalized number of contacts increases with increasing particle diameter; however, the rate of decrease with velocity is greater for larger particle diameters. Once again, future work should investigate the trends observed in the flow mechanics.

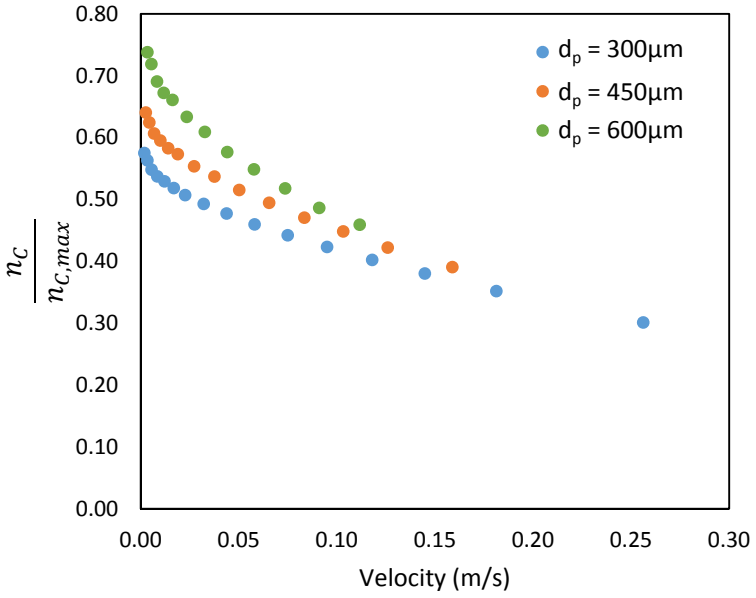

Figure 3.7: Variation in the normalized number of particle contacts per unit wall area with flow rate and particle diameter.

An empirical correlation was developed to capture the trends observed in the DEM data for all six system configurations:

$$\frac{n_C}{n_{C,max}} = \left(\frac{1.6}{A^{0.09}} - 0.6\right) \exp\left(-\left(0.07 + \frac{175}{A^{2.55}}\right)\frac{U}{\sqrt{g d_p}}\right) \tag{40}$$

The correlation agrees with the simulation results within 16%. A different correlation with better agreement was found, however, extrapolating the correlation to larger particle diameters yielded values greater than 1, which is not possible. A better correlation may be obtained if a larger variety of system configurations are tested. The DEM simulations require a lot of computational power and time; therefore, it was not realistic to run more cases for the present study. The tube and particle diameters tested were therefore selected to best represent the experimental test cases of the present work. Regardless, although the error in the selected correlation (Equation 40) may seem large, the error observed in k_{wa} as a result of the errors in both the packing fraction and the number of contacts is less than 7%.

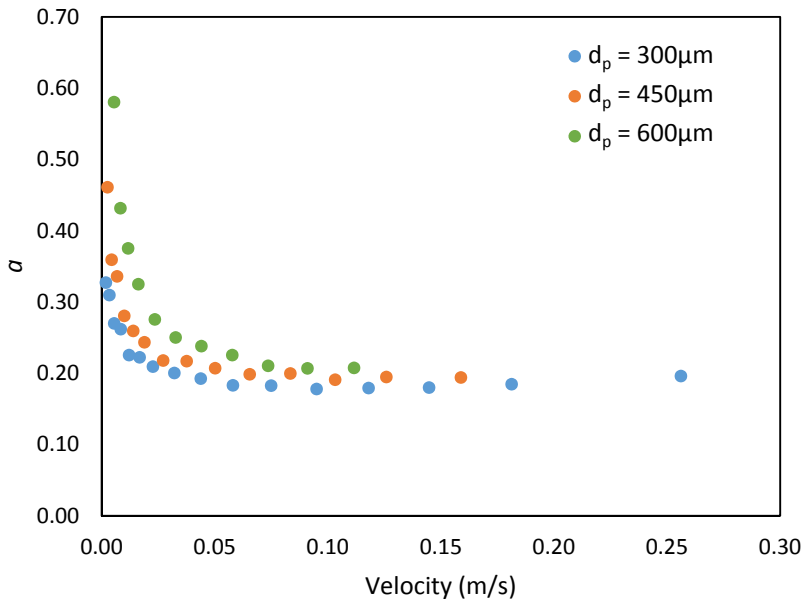

Figure 3.8: Variation in the average distance of NC particles with mean flow velocity and particle diameter.

The average distance of the NC particles from the wall (reported as the fraction of the particle radius, a) was calculated by taking the average radial location of all the NC particles in the wall-adjacent layer. The average distance, displayed in Figure 3.8, decreases with increasing flow rate at slow flow rates (<~0.03m/s) and then saturates to an essentially constant value for faster flow rates.

The simulation results were also used to validate the assumption that all NC particles can be approximated at the same average distance from the wall. The number of NC particles were calculated from the simulation centroid data, based on the total number of particles with partial volumes in the wall-adjacent layer and the number of contact particles. The number of NC particles was also calculated using Equation 31, the number of contact particles (Figure 3.6), and the fractional average distance data (Figure 3.8). The difference between the numbers of NC particles calculated from each method was less than 6%. As a result, the assumption that the NC particles can be approximated at an average distance seems reasonable.

Note that the results discussed above were found for flows composed of particles with the material properties of the zirconia-silica particles. We recognize that the behavior of granular flows depends on many structural and contact properties, such as the coefficient of restitution and the friction between particles. We suspect that the general trends observed in the wall-adjacent layer packing fraction and number of contact particles are true regardless of the particle material, however, we are uncertain whether the relative magnitudes will change. Testing different particles to examine this effect was beyond the scope of this work, as we were focused on the study of ceramic particles.

3.2.2. Results

An example of the relative contribution of each resistive component to the total effective thermal conductivity of the wall-adjacent layer is plotted in Figure 3.9 as a function of the distance of the NC particles from the wall. Note that these results are plotted for 300µm particles in the 7.75mm ID tube at a mean flow velocity of 0.058m/s, assuming zirconia-silica particle properties.

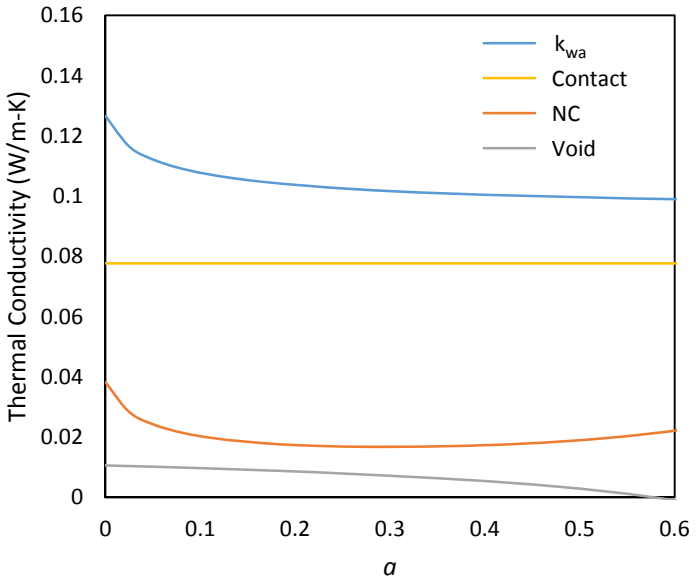

Figure 3.9: Wall-adjacent layer effective thermal conductivity and the individual thermal conductivities due to contact particles, NC particles, and void spaces, plotted as a function of the distance of NC particles from the wall. Plotted for 300µm particles in the 7.75mm ID tube at 0.058m/s.

The contribution from contact particles (2nd term of Equation 30) is constant for a given flow rate and system configuration. The contribution from NC particles (3rd term of Equation 30) initially decreases with increasing distance from the wall, then begins to increase at large values of 'a'. While the thermal conductivity of a single NC particle (k_{NC}) continually decreases with increasing distance from the wall (as indicated by Morris et al. [29]), the total contribution to the wall-adjacent layer ETC from NC particles depends on the number of NC particles. For a given

number of contact particles, which is constant for a given flow rate and system configuration, the number of NC particles increases with increasing distance from the wall. The contribution from the void spaces (1st term of Equation 30) gradually decreases, again due to the increased number of NC particles. Figure 3.9 suggests that k_{wa} decreases noticeably for small values of 'a'; however, for distances greater than approximately $0.2r_p$, the rate of decrease is more gradual. According to Figure 3.8, the average distance of NC particles for all system configurations tested is greater than $0.2r_p$. Therefore, the variation in 'a' observed in Figure 3.8 has minimal effect on the ETC value calculated. Thus, in an attempt to simplify the ETC correlation for the wall-adjacent layer (Equations 35-37), the average distance of the NC particles from the wall was assumed to be constant at $0.22r_p$. The resulting ETC correlation can thus be written as

$$k_{wa} = k_g \left\{1 + \pi r_p^2 n_C \left(1 + \frac{1}{A}\right)[2\Phi_C - 1] + \left(0.74 + \frac{1}{A}\right)\left[3\left(1 - \frac{0.5}{A}\right)\phi_{wa} - 2\pi r_p^2 n_C\right](2\Phi_{NC} - 0.95)\right\} \quad (41)$$

$$\Phi_{NC} = \left(\frac{K}{K-1}\right)^2 \left[\left(1.22 - \frac{0.22}{K}\right)\ln\left(\frac{K}{0.22K+0.78}\right) - \frac{0.78(K-1)}{K}\right] \quad (42)$$

This simplified solution shows good agreement with the complete solution for a cylindrical wall with variable 'a', yielding less than 1.0 % error.

Using the final expression for the wall-adjacent layer ETC (Equations 41,36,42) and the empirical correlations developed for the packing fraction (Equation 38) and the number of contacts (Equation 40), the variation in the heat transfer at the wall with flow rate was examined (Figure 3.10). As expected, the ETC of the wall-adjacent layer decreases with increasing flow rate due to the reduced packing fraction and number of contacts. The relative importance of the packing fraction and number of contacts on the wall-adjacent layer heat transfer was examined by varying one parameter while keeping the other constant. The ETC calculated using a constant packing

fraction (the slow flow rate value) and variable number of contacts, as well as the ETC calculated using a constant number of contacts (the slow flow rate value) and variable packing fraction are also plotted in Figure 3.10. It is clear that the number of particle-wall contacts is the primary factor contributing to the decrease in heat transfer observed.

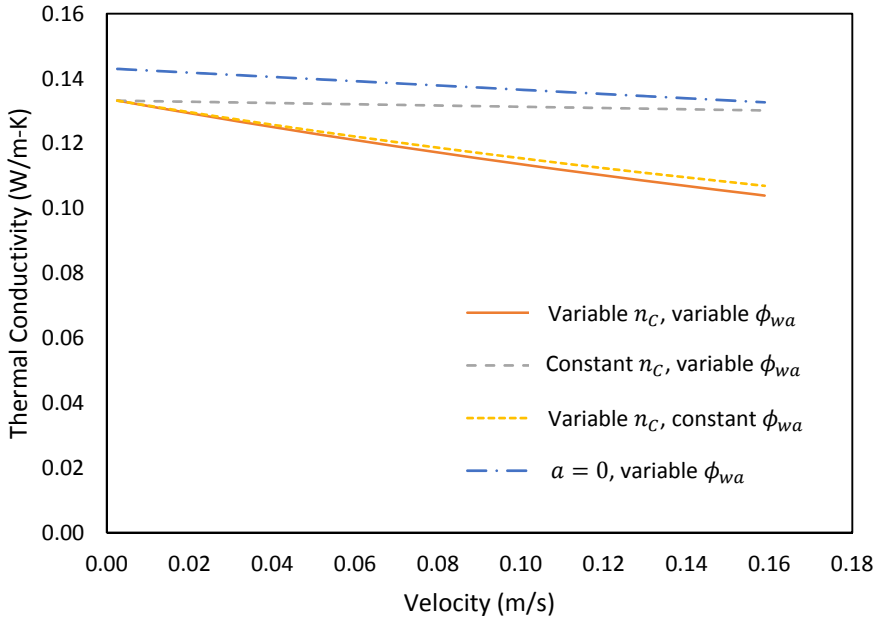

Figure 3.10: Effective thermal conductivity of the wall-adjacent layer as a function of mean flow velocity for $A = 17.2$, calculated using 1) variable n_C and ϕ_{wa}, 2) constant n_C and variable ϕ_{wa}, 3) variable n_C and constant ϕ_{wa}, and 4) $a = 0$ and variable ϕ_{wa}.

Finally, the significance of incorporating the heat transfer to NC particles was examined by calculating the ETC of the wall-adjacent layer assuming all particles are in contact with the wall (i.e. $a = 0$). The results, calculated using Equation 35 (with $a = 0$) and Equation 36 and a variable packing fraction, are also plotted in Figure 3.10. The thermal conductivity is greater than that predicted when including NC particles due to the superior heat transfer exhibited by contact particles. The difference is most apparent at faster flow rates, where the thermal conductivities calculated differ by up to 24%. The ETC for $a = 0$ approaches the ETC calculated using $a = 0.22$

with variable packing fraction and constant number of contacts since the packing fraction decreases at faster flow rates. For a given number of particle-wall contacts, the number of NC particles decreases with increasing flow rate and the relative contribution to the total ETC from the NC particles decreases. As a result, the two solutions converge when the packing fraction decreases such that there are no NC particles.

Chapter 4
Model Evaluation

The correlation developed in the previous chapter to describe the wall-adjacent layer effective thermal conductivity was implemented in the two-layer Nusselt number correlation and compared with the low temperature experimental results. The ETC correlation was also implemented in the single resistance model developed by Sullivan & Sabersky [16] and compared with results in the literature. The subsequent sections discuss the agreement with experimental results from the present work and results for similar system configurations found in the literature, as well as investigate how well the model developed predicts the thermal conductivity of a static particle bed measured using the DTC specimen cell.

4.1. Comparison with Experimental Results

In order to compare the experimental results from Section 2.3 with the two-layer model developed in Section 3.1, the wall-adjacent layer effective thermal conductivity (ETC) must first be determined. According to Section 3.2, the wall-adjacent layer ETC can be calculated based on the tube diameter, the particle diameter, the thermal conductivities of the interstitial gas and the solid particles, and the mean flow velocity. The temperature-dependent thermal conductivity

correlations for the particle materials determined in Section 2.2.3.3 were used to establish the particle thermal conductivity at the mean flow temperature. The bulk ETC was calculated at the mean flow temperature using the correlations discussed in Section 2.2.3.1.

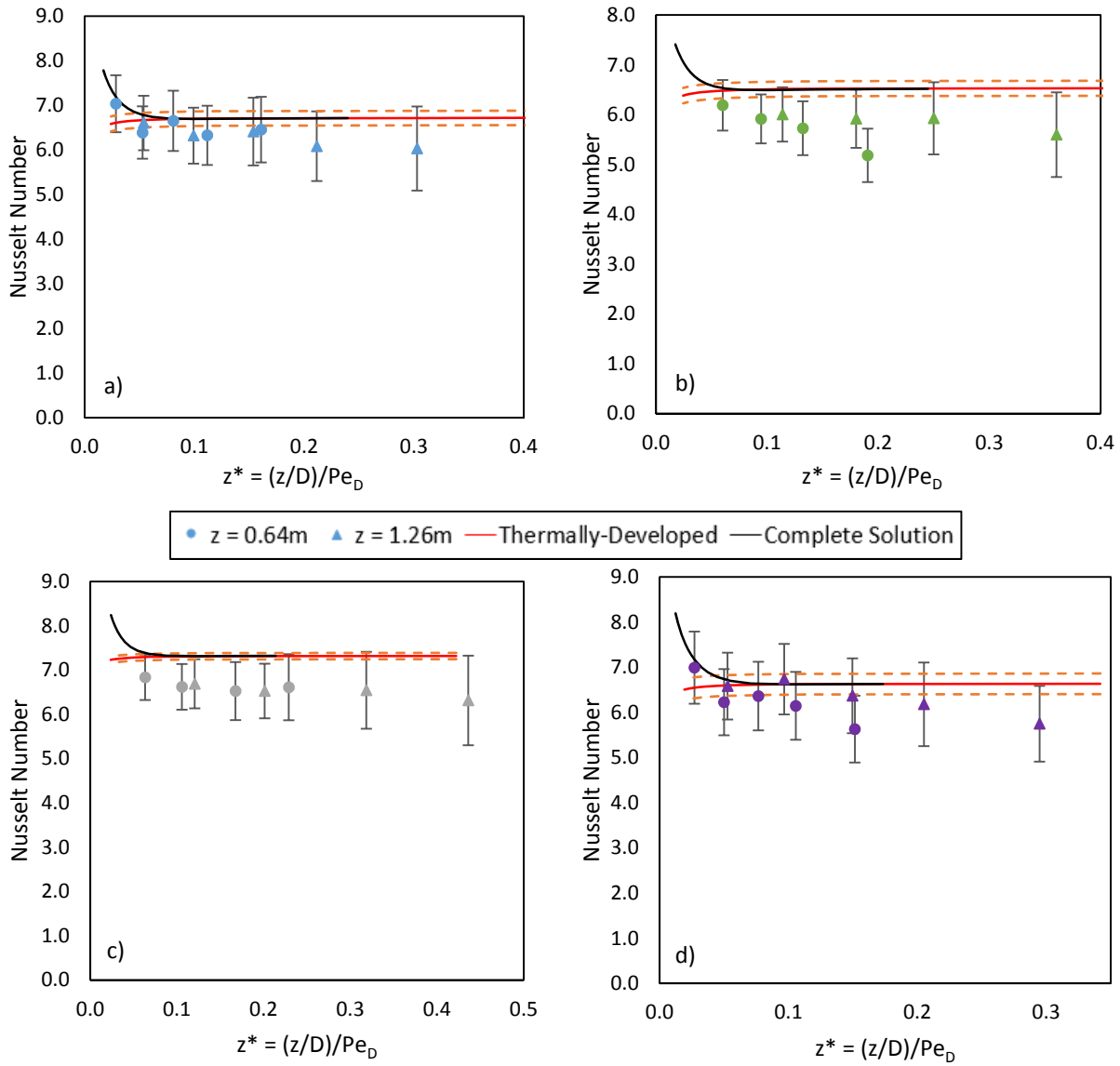

Figure 4.1: Comparison of experimental data and two-layer model for the 9.5mm OD tube with the a) 270µm Z-S, b) 320µm Z-S, c) 140µm Z-S, and d) 340µm A-S particles. Error bars and dashed lines denote 95% confidence interval.

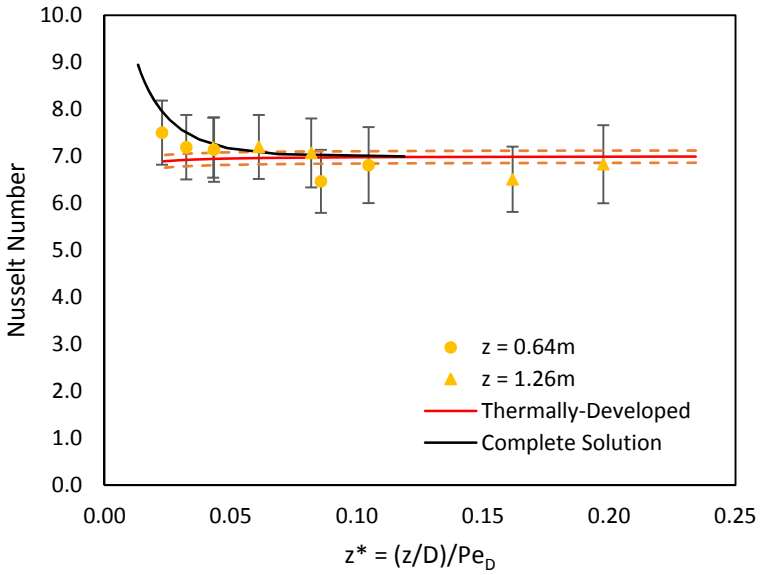

Figure 4.2: Comparison of experimental data and two-layer model for the 12.7mm OD tube with the 270µm Z-S particles. Error bars and dashed lines denote 95% confidence interval.

The experimental results for the 9.5mm OD tube and the 12.7mm OD tube are compared with the two-layer model in Figure 4.1 and Figure 4.2, respectively. The models displayed were calculated using thermal properties at the mean flow temperature (i.e. T = 105°C). The error bars and dashed lines denote the 95% confidence interval for the experimental data and the two-layer model. The 95% confidence interval calculated for the two-layer model Nusselt number depends only on the uncertainty in the bulk ETC.

The experimental results for all test cases, except for a couple stray values, agree with the two-layer model within the experimental uncertainty. The worst agreement is observed at the slowest flow rates (large inverse Graetz numbers) and for the smallest particles; these cases demonstrate the largest experimental uncertainty due to the small temperature differences across the flow. In all cases, note that the Nusselt numbers predicted demonstrate a slight decrease with increasing flow rate (i.e. decreasing inverse Graetz number), while the experimental results display a slight increase in heat transfer with increasing flow rate. Due to the large experimental

uncertainty, however, it was difficult to claim an increase in heat transfer. In addition, no physical explanation for an increase in heat transfer could be identified; therefore, it seems more likely that the heat transfer behaves as suggested by the model.

Figure 4.1 and Figure 4.2 display two forms of the two-layer model: the solution for the thermally-developed region and the complete solution for all axial positions. Recall that the two-layer model presented in Section 3.1 was developed for the thermally-developed region. The fastest flow rates, corresponding to small inverse Graetz numbers (z^*), are on the border of the thermally-developed region. The complete solution to the two-layer model system of equations (Equations 15-20) was derived to compare with the results from the fastest flow rates (see Appendix B for solution). Comparison of the two solutions suggests that the thermally-developed solution applies to $z^* > 0.08$. The Nusselt numbers measured for the fastest flows at z = 0.64m show good agreement with the complete solution. The thermally-developed solution to the two-layer problem was presented as the primary Nusselt number correlation because the complete analytic solution is a lengthy series solution and most all the cases tested in the present study fall within the thermally-developed region.

Close observation of Figure 4.1a and Figure 4.2 indicates that the 12.7mm OD tube with the 270μm zirconia-silica particles yielded larger Nusselt numbers than the 9.5mm OD tube with the 270μm zirconia-silica particles (for direct comparison, see Figure 2.19). This variation can be explained by the two-layer model. Recall from Section 3.1 that the thermally-developed correlation for the Nusselt number depends on three parameters: the bulk ETC, the wall-adjacent layer ETC, and the relative size of the bulk layer, W, which depends on the tube-to-particle diameter ratio. If the contact and bulk layer ETCs are assumed to be constant for all tube and particle diameter combinations, the general effect of tube and particle diameter on the heat transfer

to the flow can be observed. Figure 4.3 below displays the Nusselt number as a function of the tube-to-particle diameter ratio, assuming $k_{wa} = 0.12$W/m-K and $k_b = 0.30$W/m-K.

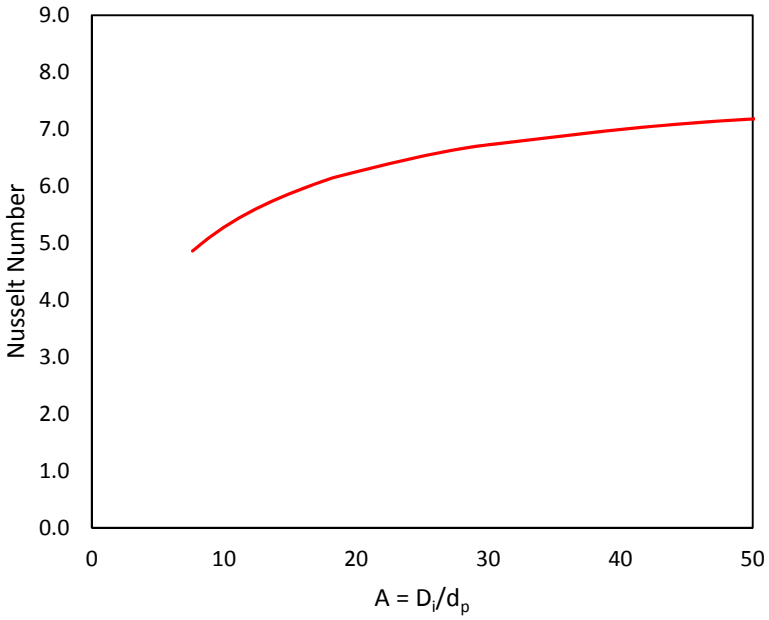

Figure 4.3: Nusselt number predicted by the two-layer model as a function of the tube-to-particle diameter ratio. Assumes k_{wa} and k_b are constant.

There is a clear increase in the Nusselt number with increasing tube diameter and/or decreasing particle diameter. As the tube-to particle diameter ratio approaches infinity, the Nusselt number approaches a value of 8. This makes sense, as the relative size of the bulk layer approaches a value of 1 as the tube-to-particle diameter ratio increases, thereby approaching a continuum solution. As demonstrated in Figure 4.1 and Figure 4.2, the model captures the increase observed in the experimental data.

The results presented in this section reiterate that the heat transfer to dense granular flows is well represented as a continuum flow with an increased thermal resistance at the wall, as discussed by other researchers. Unlike previous works implementing a thermal contact resistance at the heated surface, our model calculates the thermal resistance at the wall for a flow using system

parameters, rather than employing a single empirical coefficient or using static bed correlations. Ideally, the ETC correlation developed for the wall-adjacent layer should be compared with experimental or numerical results measuring this parameter. Due to time restrictions and the complex nature of experimentally measuring a wall temperature jump in a flow, however, this was not possible. Future work implementing heat transfer models into the DEM simulations may help verify the results observed. The agreement observed with the two-layer model after implementing the ETC correlation suggests, however, that the near-wall heat transfer phenomenon is being captured reasonably well.

4.2. Comparison with Data in the Literature

The validity of the ETC correlation developed for the wall-adjacent layer was also tested by using the correlation to estimate the resistance to heat transfer adjacent to the wall for vertical flows found in the literature. The experimental studies performed by two different groups of researchers were used to assess the model's applicability. Sullivan & Sabersky [16] and Natarajan & Hunt [17] studied the heat transfer to vertical chute flows (rectangular cross-section) with a single heated wall, each using different heated lengths. Both Sullivan & Sabersky and Natarajan & Hunt found good agreement between their experimental results and the single-resistance model developed by Sullivan & Sabersky for low flow rates.

Sullivan & Sabersky's model was developed for a chute flow with a single heated wall maintained at a constant temperature. They assumed that the flow consisted of a thin air gap adjacent to the heated wall; the rest of the flow was assumed to maintain bulk effective properties. Unlike the two-layer model developed in the present study, their solution employed a temperature jump boundary condition in the solution of the energy equation, using a conductance term to

represent the increased thermal resistance at the wall. The model developed by Sullivan & Sabersky is reprinted below for convenience:

$$\overline{Nu_L} = \frac{1}{\frac{\chi d_p k_b}{k_g L} + \frac{\sqrt{\pi}}{2}\sqrt{\frac{1}{Pe_L}}} \tag{43}$$

Here, χ represents the relative thickness of the air gap adjacent to the heated wall and Pe_L represents the Péclet number based on the length of the heated section, L. In order to utilize the model developed in the present study to calculate χ, the two modelling approaches were compared. The wall-adjacent layer utilized in the present study has a thickness of a particle radius, with a single ETC associated with the entire domain. This domain was divided into two regions to account for the modelling approach used by Sullivan & Sabersky: a small air layer with a thickness of χd_p and a bulk layer in the remaining thickness. Using thermal resistances, the thickness of the air layer used by Sullivan & Sabersky can be approximated based on k_{wa} according to

$$\chi = \frac{0.5}{\frac{k_b}{k_g} - 1}\left(\frac{k_b}{k_{wa}} - 1\right) \tag{44}$$

The wall-adjacent layer ETC correlation, which was developed for a cylindrical system, was rewritten in a more general form to be applicable for rectangular chute flows as well:

$$k_{wa} = k_g\left\{1 + \pi r_p^2 n_C B_C(2\Phi_C - 1) + 0.74 B_{NC}\left[3\left(1 - \frac{0.5}{A_m}\right)\phi_{wa} - 2\pi r_p^2 n_C\right](2\Phi_{NC} - 0.95)\right\} \tag{45}$$

$$A_m = \frac{P}{\beta d_p} \qquad \text{w/ } \beta = \begin{cases} \pi\,; & cylinder \\ 4\,; & chute \end{cases} \tag{46}$$

Here, B_C represents the correction term for the contact particles for a cylindrical system $\left(B_C = 1 + \frac{1}{A}\right)$, B_{NC} represents the correction term for the NC particles for a cylindrical system $\left(B_{NC} = 1 + \frac{1.35}{A}\right)$, A_m represents a modified tube-to-particle diameter ratio, P represents the

perimeter of the cross-section, and β represents a shape-dependent correction factor. Note that the modified tube-to-particle diameter ratio simplifies to the tube-to-particle diameter ratio for a circular cross-section. Also, note that B_C and B_{NC} are equal to 1 for a chute because the flat plate solution to the heat transfer problem is accurate for a chute $\left(A = D/d_p \to \infty\right)$.

While the correlations developed in the present study for the packing fraction and number of contacts are based on data obtained for flows through cylindrical tubes, they were used to estimate the values for the chute flows under consideration by utilizing the modified tube-to-particle diameter ratio. This may not be the best parameter to compare the flow physics in a cylinder and a chute, however, without any chute flow data, the modified tube-to-particle diameter ratio was used in an attempt to stay consistent. The hydraulic diameter-to-particle diameter ratio was also discussed as a possible controlling parameter, as it captures the shape of the cross-section, rather than just the perimeter, which may be an important parameter controlling the flow physics. Using the hydraulic diameter to calculate ϕ_{wa} and n_C sometimes yielded a negative number of NC particles for a chute, which does not make sense. A wider range of DEM data for different cross-section shapes and tube and particle diameters would help clarify the uncertainties present in extrapolating the empirical correlations to different system configurations. An understanding of the physics controlling the wall-adjacent layer packing fraction and number of contact particles would also help explain the trends observed.

Sullivan & Sabersky studied the heat transfer to slow flows of particles through chutes with short heated lengths (< 2.54cm). Their experimental results for the glass particles tested are displayed in Figure 4.4. The Nusselt numbers predicted by Equations 43 and 44, using the modified form of the wall-adjacent layer ETC correlation (Equations 45, 36, 42), are also displayed in Figure 4.4, along with the Nusselt numbers predicted by Sullivan & Sabersky using $\chi = 0.085$. The bulk

thermal conductivity was calculated using the correlation developed by Zehner & Schlünder [51] for a static particle bed. This correlation has been shown to provide a reasonably accurate prediction of bulk ETC over a wide range of solid-fluid thermal conductivity ratios [9].

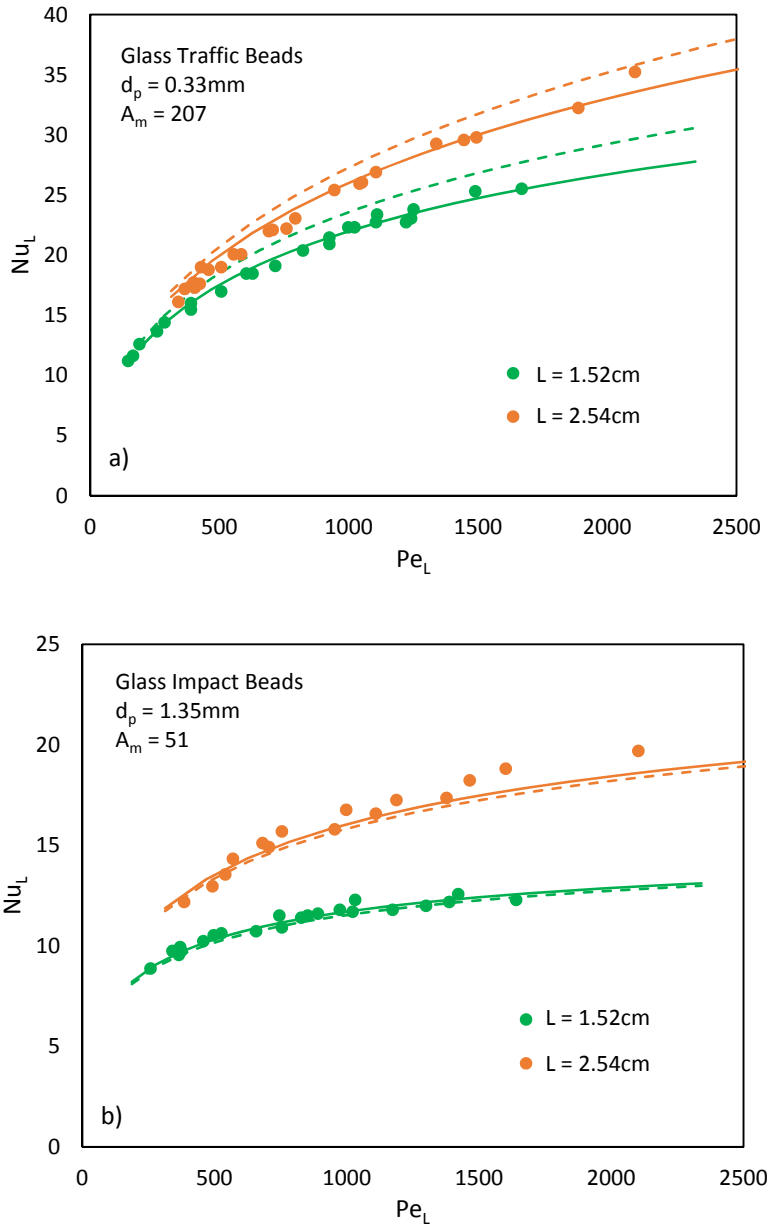

Figure 4.4: Variation of the Nusselt number with Péclet number and length of heated section. Data points represent experimental data from Sullivan & Sabersky for a) 0.33mm glass traffic beads and b) 1.35mm glass impact beads. Solid lines denote single resistance model prediction using k_{wa} for χ. Dashed lines denote single resistance model prediction with $\chi = 0.085$.

The Nusselt numbers calculated using the ETC correlation show good agreement with the experimental data. The Nusselt numbers predicted for the 1.35mm particles are similar to those predicted by Sullivan & Sabersky, which suggests that the thermal contact resistance is essentially constant for slow flow rates. The ETC correlation also predicts an essentially constant thermal contact resistance for the 0.33mm particles; the resulting χ value is slightly greater, however, than that used by Sullivan & Sabersky. Note that A_m for the 0.33mm particles is well outside the range of values tested using the DEM simulations.

Natarajan & Hunt expanded upon the work of Sullivan & Sabersky by testing a wider range of flow rates and a longer heated length. The experimental results for the glass particles tested by Natarajan & Hunt are displayed in Figure 4.5. Once again, the Nusselt numbers predicted by Equations 43 and 44 are plotted for a constant $\chi = 0.085$ and a variable χ calculated using the ETC correlation developed in the present study.

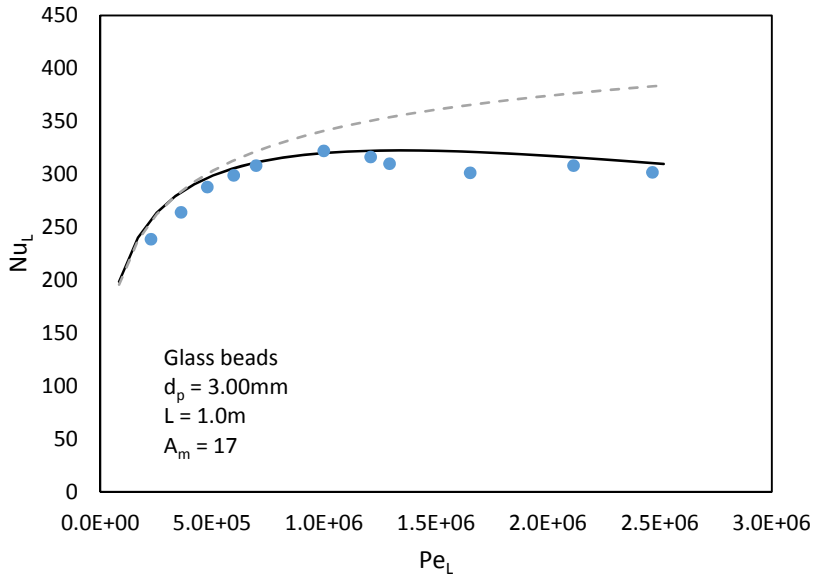

Figure 4.5: Variation of the Nusselt number with Péclet number. Data points represent experimental data from Natarajan & Hunt for 3.0mm glass particles in a vertical chute with L=1.0m. Solid line denotes single resistance model prediction using k_{wa} to find χ. Dashed line denotes single resistance model prediction using $\chi = 0.085$.

Both model predictions show good agreement with the experimental data for slow flow rates (U < 9.0cm/s), corroborating the observation made by Sullivan & Sabersky that a constant thermal contact resistance is valid for slower flows. At faster flow rates, however, a constant resistance does not capture the decrease in Nusselt number observed. As previously discussed, the ETC correlation developed in the present study yields a decrease in thermal conductivity with increasing flow rate, yielding an increase in χ with increasing flow rate. As a result, the decrease in Nusselt number observed experimentally is captured quite well.

4.3. Comparison with Static Bed Measurements

The accuracy of the Nusselt numbers calculated using the wall-adjacent layer ETC correlation developed, for the experimental studies in both past and present work, is encouraging. While the model was developed for particle flows, we were interested in examining its versatility. Recall from Section 2.2.3.2 that the static bed thermal conductivity measurements made using the DTC measured the thermal conductivity of a particle bed sandwiched between two heated plates. The particle bed was represented using three thermal resistances connected in series: an increased thermal resistance at both plates and a bulk resistance in between. The total thermal conductivity of the sample specimen could then be written as

$$k_{total} = \frac{t_{total}}{\frac{d_p}{k_{wa}} + \frac{(t_{total} - d_p)}{k_b}} \tag{47}$$

Using the ETC correlation developed for the wall-adjacent layer and the bulk thermal conductivity measurements discussed in Section 2.2.3.1, the total thermal conductivity of the DTC specimen cell was estimated. In an attempt to simulate the wall contact behavior present in vertical flows, the DTC apparatus was rotated 90° to lay on its side. The specimen cell was first clamped between the heater plates, and then filled with particles via a small hole drilled in the cell ring

(with the hole situated facing up to allow the cell to be completely filled). The cell was tapped during filling to allow the particles to settle within the cell. The specimen cell was assumed to have a rectangular cross-section, with dimensions based on the sample thickness and the average width of the circular plate.

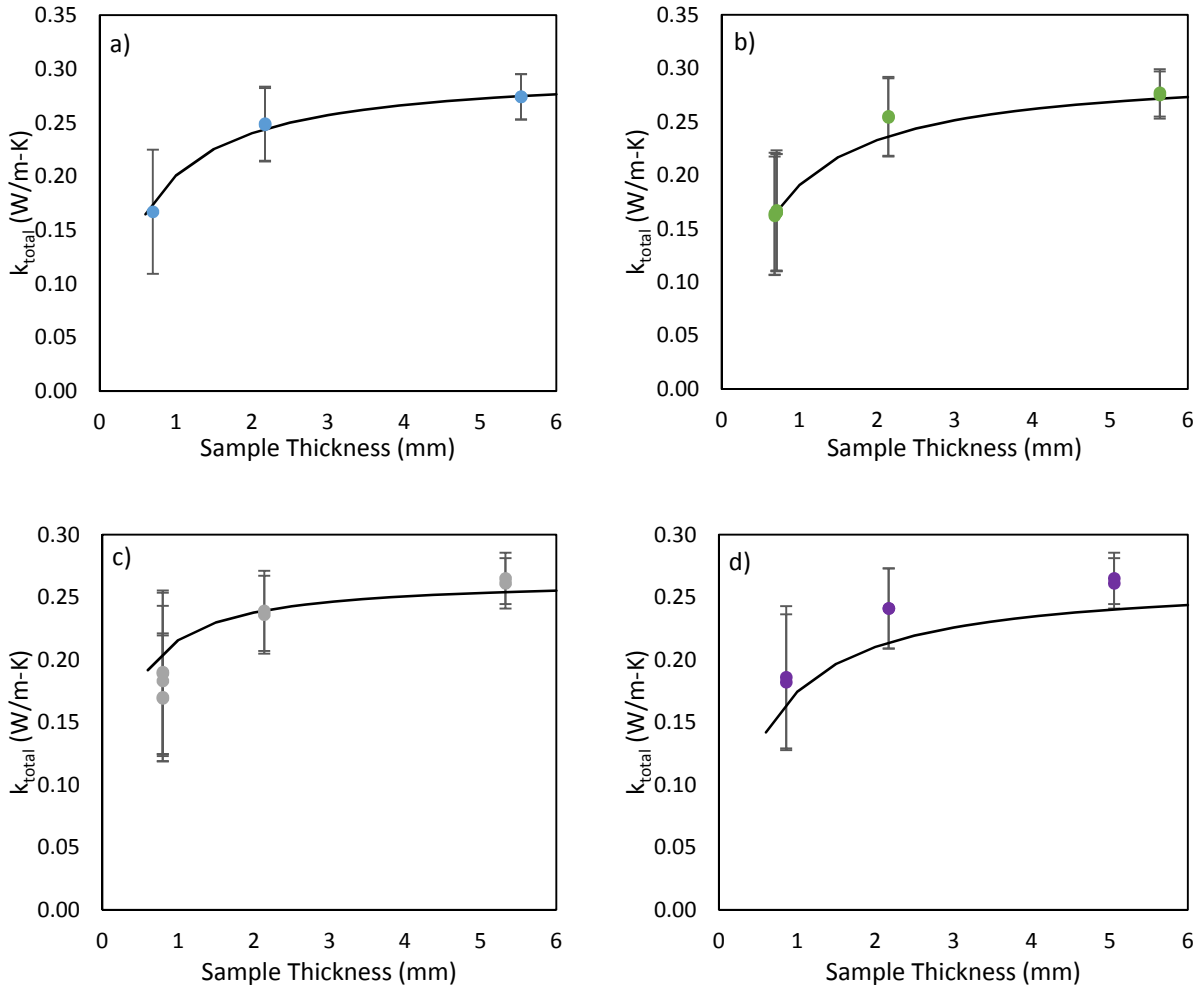

Figure 4.6: Total thermal conductivity of DTC specimen as a function of sample thickness for a) 270µm Z-S, b) 320µm Z-S, c) 140µm Z-S, and d) 340µm A-S particles. Solid line denotes total ETC calculation using k_{wa} and k_b. Error bars denote 95% confidence interval.

Figure 4.6 displays the total thermal conductivities measured for three different sample thicknesses using each particle type available, as well as the total thermal conductivity calculated using Equation 47. Note that the correlations developed for the packing fraction of the wall-

adjacent layer and the number of particle-wall contacts were extrapolated for the static bed measurements, as the correlations were developed for dense flows (U > 0.02m/s). The modified tube-to-particle diameter ratio for the specimen cell cross-section was used to approximate both parameters for U = 0m/s. The model shows good agreement with the average thermal conductivities measured for all particle diameters of zirconia-silica. The model underestimates the average thermal conductivity measured using the alumina-silicate particles. Errors may arise from the uncertainty in the bulk thermal conductivity, the extrapolation of the packing fraction and number of contacts correlations to static beds, and/or the use of the modified tube-to-particle diameter ratio.

The variation in packing fraction for a static bed was based on the trends observed for a cylinder packed with particles in their densest state [50]. For $A > 2$, the packing fraction of the wall-adjacent layer in its densest state increases with increasing tube-to-particle diameter ratio, plateauing for large values of 'A'. A similar trend was applied to the correlation developed in the present study for a static bed. The DEM data for each test case was extrapolated to U = 0m/s to determine the static bed value for each case; however, it is unclear whether these values have physical significance for a static bed. Applying the physics observed for a dense packing to these values may be incorrect; however, since there was no other data to use at this time, this was assumed correct for now. Future work may seek to validate the static bed behavior.

The correlation for the number of particle-wall contacts suggests that the number of contacts for a static bed decreases with an increasing modified tube-to-particle diameter ratio; however, this trend has no physical backing. Instead, it arose from the curve fitting process used to develop a correlation that best matched the DEM simulation data for the cases tested. Unlike the variation in packing fraction, it is unclear how or if the number of particle-wall contacts should

vary with tube-to-particle diameter ratio for a static bed. Future work may seek to examine a static bed to understand how and if the number of contacts varies for a static bed.

Despite the uncertainties present due to extrapolation of the correlations for static beds and the approximation of the DTC as a rectangular cross-section, along with the uncertainty in using the correlations for a chute configuration, the model does a respectable job of estimating the total thermal conductivity of the DTC specimen cell. This further confirms the validity of the ETC correlation developed for the wall-adjacent layer.

Chapter 5

Experimental Study of Heat Transfer to Flows at High Operating Temperatures

Since the motivation for the study was centered on concentrated solar power applications, it was important to examine the heat transfer to the particulate flows at temperatures more characteristic of solar power towers. The subsequent sections discuss the modifications made to the experimental apparatus to account for the higher temperatures and the variation in the heat transfer to the flow observed with increasing temperature. The modifications made to the two-layer model to incorporate radiation heat transfer within the flow is also discussed.

5.1. Modifications to Accommodate High Temperatures

The experimental apparatus discussed in Section 2.1.1 was modified to accommodate measurements at elevated temperatures. In particular, the thermal expansion of the tube disrupted the measurement of the radial temperature profile. Recall that the FF thermocouple probes were attached to a fixed support bar, with the probes inserted into the tube through a small hole in the tube wall. Thermal expansion of the tube at higher temperatures caused the thermocouple probe to

bend, yielding inaccurate radial positioning of the thermocouple within the tube. To ensure that the thermocouple probes did not bend, a system was designed to allow the probes to move axially with the tube as it expanded, as seen in Figure 5.1.

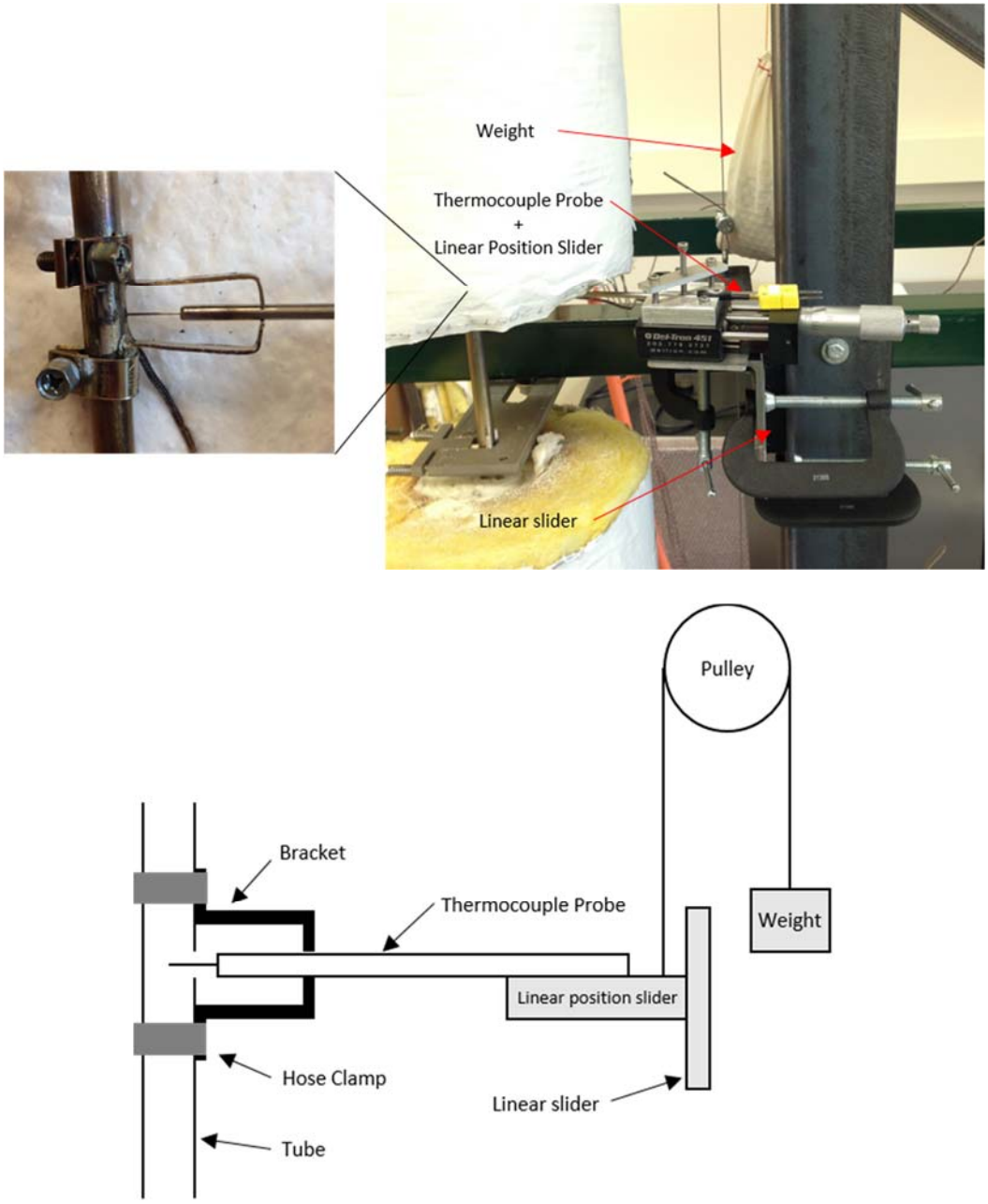

Figure 5.1: System designed to accommodate flow temperature measurement during tube expansion.

Two Inconel brackets were machined and attached to the tube using hose clamps to create a support for the thermocouple probe. The thermocouple probe and linear position slider were allowed to move axially by means of a linear slider, which was attached to the fixed support bar. A counter-weight was applied using a pulley to prevent the brackets from supporting the entire weight of the thermocouple and slider. During the heating of the tube, the top Inconel bracket forced the thermocouple to move with the tube as it expanded. During the cooling of the tube, the bottom Inconel bracket performed a similar function.

At the highest temperatures, the thermocouple was observed to move up to approximately 6mm. Insulating the tube around these brackets was a struggle, as any insulation in the path of the bracket motion impeded the motion of the thermocouple and resulted in slight bending of the thermocouple. Finding a balance between providing adequate insulation around the tube while allowing the thermocouple to move unimpeded was a challenge. Ultimately, the best method for achieving this balance was to leave space for the thermocouple to expand during heating; once the tube had reached approximately 95% of its final temperature, insulation was added in the open space. It was assumed that at this temperature, the primary expansion of the tube had occurred, yet there was still plenty of time for the system to equilibrate with the additional insulation.

The primary goal for the high temperature measurements was to examine how the heat transfer to the flow varied with increasing flow temperature. As such, a single orifice was used for the high temperature measurements to examine the variation with temperature at a constant flow rate. Both the 9.5 and 12.7mm OD tubes were utilized, along with the 270 and 320μm zirconia-silica particles. The system configurations utilized and the corresponding flow velocities are listed in Table 5.1.

Table 5.1: Experimental system configurations for high temperature measurements.

Configuration Number	Tube OD (mm)	Particle Diameter (mm)	Tube-to-Particle Diameter Ratio	Mean Flow Velocity (m/s)
2	9.53	0.270	28.2	0.020
5	12.70	0.270	40.1	0.014
6	12.70	0.320	33.8	0.014

The effective thermal conductivity correlations used to estimate the ETC of the flow at each FF location for the low temperature measurements were based on the values measured experimentally using the concentric tube apparatus. Recall that the experimental results were performed for temperatures up to 700°C or less. The correlations, therefore, would need to be extrapolated to estimate the ETC values for the high temperature measurements, which span up to 1000°C. Extrapolation may lead to inaccurate estimates of the ETCs, and as a result yield skewed Nusselt numbers. In an attempt to avoid "random" extrapolation, the Van Antwerpen et al. [44] model was used to estimate the effective thermal conductivity for the high temperature measurements. Recall that the material thermal conductivities for each particle were approximated by minimizing the difference between the experimental data and the Van Antwerpen model; the model, therefore, captures the experimental results reasonably well. A linear regression was fit to the model results for both the 270 and the 320μm zirconia-silica particles. This allowed for easy estimation of the ETC, rather than solving the Van Antwerpen model for each temperature tested. The resulting correlations are recorded in Table 5.2.

Table 5.2: Effective thermal conductivity correlations used for high temperature measurements.

Particle Material	Particle Diameter (μm)	Thermal Conductivity (W/m-K) [T in °C]	Range (°C)
Zirconia-silica	270	$0.00031T + 0.273$	40 < T < 1000
	320	$0.00033T + 0.270$	40 < T < 1000

5.2. High Temperature Measurement Results

The radial temperature distributions measured for the high temperature flow cases demonstrated similar characteristics to the low temperature profiles. An example of the profiles obtained using the 12.7mm OD tube with the 270µm zirconia-silica particles (configuration 5) are displayed in Figure 5.2.

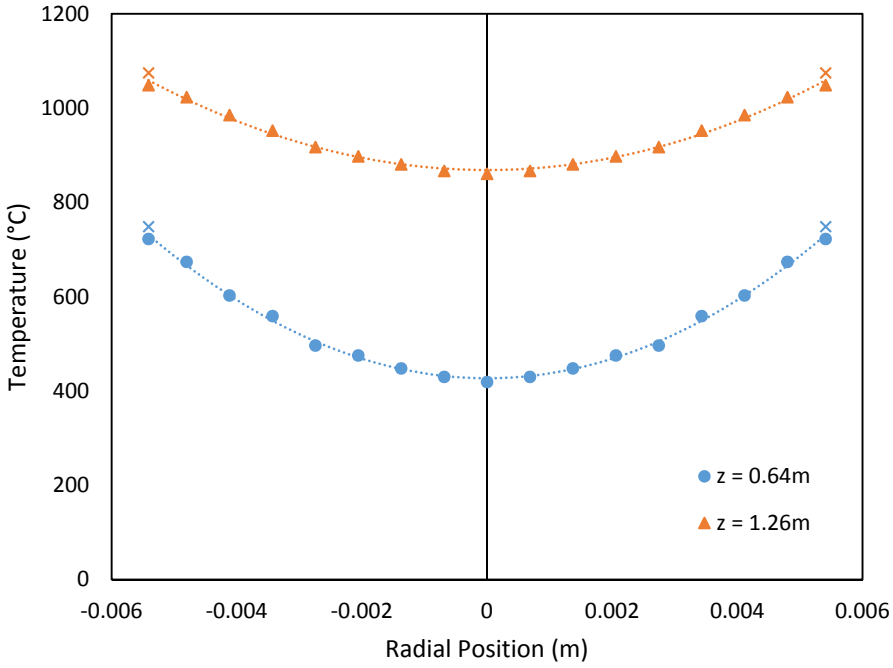

Figure 5.2: Radial temperature distributions for 270µm Z-S particles in the 12.7mm OD tube for $q''_{wall} = 46\text{kW/m}^2$. Solid shape denotes experimental data, dashed line denotes quadratic regression, and '×' denotes wall temperature.

For most cases, both temperature distributions demonstrated essentially quadratic shapes. Note that the profile at z = 1.26m is shallower than the profile at z = 0.64m due to the enhanced thermal properties at higher temperatures. A temperature jump is still observed at the wall; however, the relative magnitude of the jump decreases with increasing temperature. This can also be explained by enhanced thermal properties with increasing temperature.

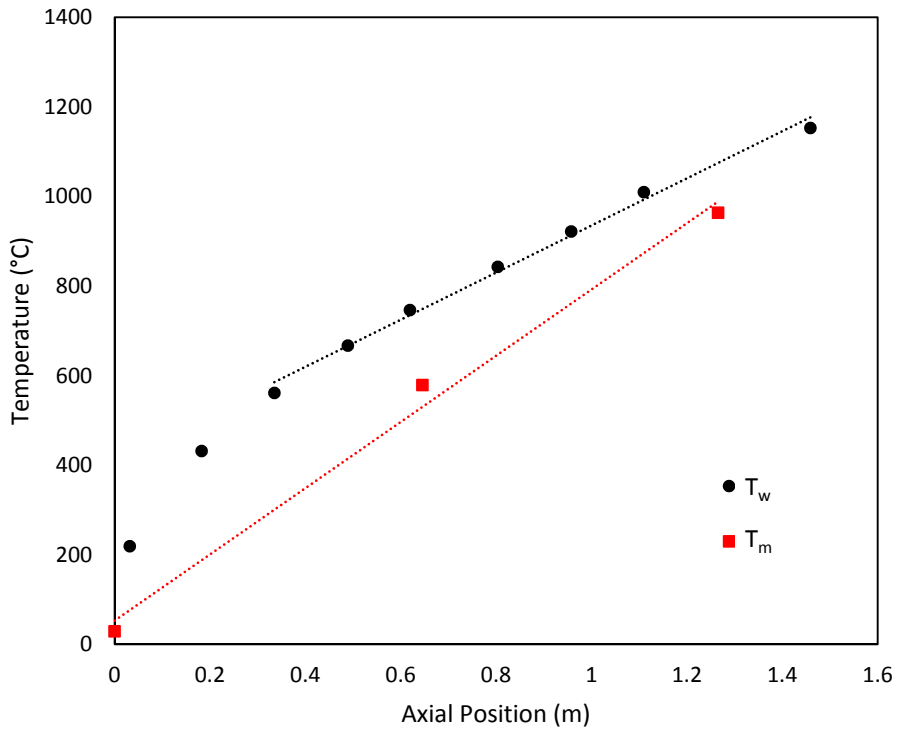

Figure 5.3: Axial wall and mean temperature distributions for 270µm Z-S particles in the 12.7mm OD tube for $q''_{wall} = 46\text{kW/m}^2$. Dashed lines denote linear regression.

The axial distribution of the mean temperatures calculated from the radial profiles in Figure 5.2 is plotted in Figure 5.3, along with the axial wall temperature distribution. The thermally-developing and thermally-developed regions are once again distinguishable by examining the wall temperature distribution. Since the present experiments span a very large temperature range (up to 1100°C in the hottest cases), the wall-mean temperature difference decreases with increasing axial position as the thermal properties increase with increasing temperature. The linear regression plotted with the mean temperature distribution does not capture the temperature at z = 0.64m very well. Examination of the 1st Law energy balance helps explain the trend observed in the mean temperature distribution.

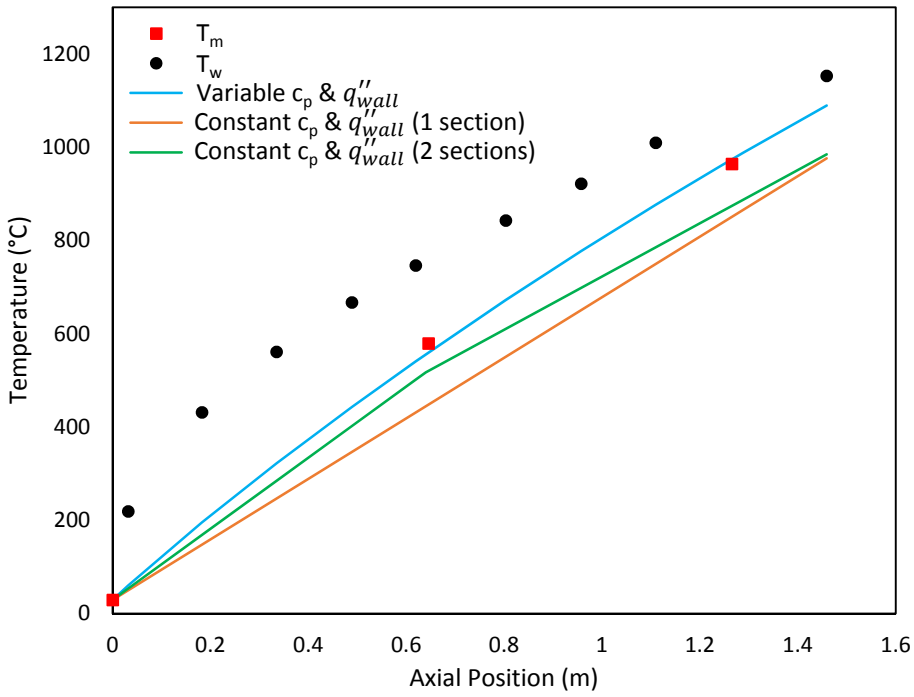

Figure 5.4: Comparison of mean temperatures calculated using an energy balance and experimental data (270μm Z-S particles, 12.7mm OD tube, $q''_{wall} = 46\text{kW/m}^2$). Solid shapes denote experimental data; solid lines denote energy balance results.

Figure 5.4 compares the axial distribution of the mean temperatures calculated from experimental data with those calculated using Equation 14. The mean temperatures calculated assuming constant specific heat and wall heat flux, using one and two tube sections, are also plotted. Recall that the constant specific heat, constant wall heat flux case matched well with the experimental data for the low temperature measurements. For the higher temperature measurements presented here, however, this is no longer the case. Since the tube spans such a wide temperature range, applying an average specific heat value to half of the tube no longer captures the mean temperature variation. The energy balance accounting for the variation in the specific heat and the variation in the wall heat flux, on the other hand, agrees well with the experimentally measured values.

The heat transfer coefficients calculated for each of the system configurations tested are shown in Figure 5.5. The local heat transfer coefficient calculated at each measurement location (i.e. z = 0.64 and z = 1.26m) is plotted at the corresponding mean flow temperature.

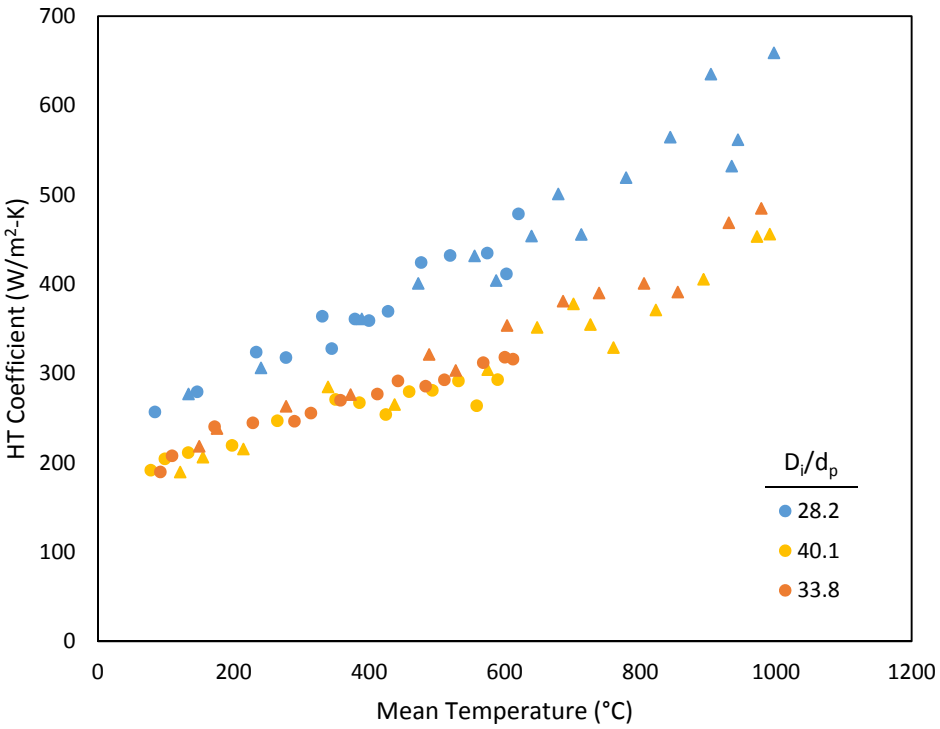

Figure 5.5: Heat transfer coefficients calculated for each system configuration as a function of mean temperature. '●' denotes value measured at z = 0.64m, '▲' denotes value measured at z = 1.26m.

Figure 5.6 displays the results for the 12.7mm OD tube with the 320µm particles with the 95% confidence intervals plotted in the form of error bars. The largest uncertainty is seen at the highest temperatures due to the increased uncertainty associated with the thermocouples at higher temperatures. Across all system configurations, the relative uncertainties calculated were up to 14%.

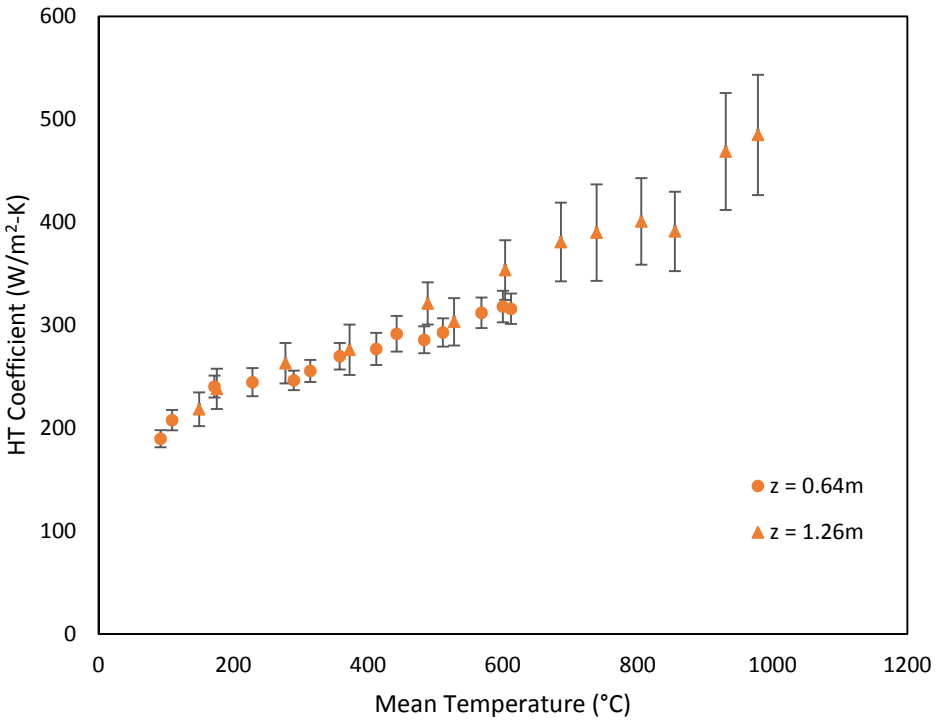

Figure 5.6: Heat transfer coefficients for the 320µm particles in the 12.7mm OD tube. Error bars denote 95% confidence interval.

As expected, all system configurations display an increase in heat transfer with increasing temperature due to enhanced thermal properties. Studies of heat transfer within static particle beds, such as the theoretical analysis by Van Antwerpen et al. [44] discussed in Section 2.2.3.3 or the experimental study of Yagi & Kunii [30], suggest that the radiation contribution increases not only with temperature, but also with increasing particle diameter. The 270 and 320µm zirconia-silica particles were tested in an attempt to examine this effect in the dense granular flows. As seen in Figure 5.5, the results for both particle diameters are essentially the same. In reality, the variation in heat transfer expected for such a small difference in particle diameter is too small to be discerned from the experimental uncertainty. The difference in effective thermal conductivity for these two particle diameters observed in Figure 2.12 is less than 4% at 1000°C. Future work should

investigate the effect of particle diameter at high operating temperatures more thoroughly by using a wider range of particle diameters.

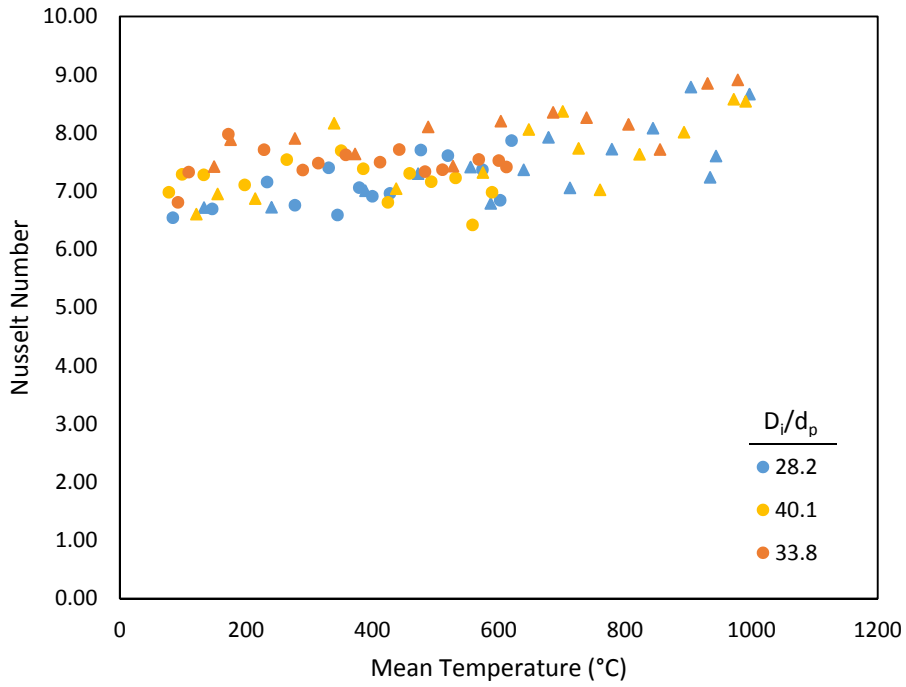

Figure 5.7: Nusselt numbers calculated for all system configurations as a function of mean temperature. '●' denotes value measured at z = 0.64m, '▲' denotes value measured at z = 1.26m.

The Nusselt numbers calculated from the heat transfer coefficients in Figure 5.5 and the effective thermal conductivity relations summarized in Table 5.2 are presented in Figure 5.7. Although it is a bit difficult to discern due to the scatter present in each data set, the Nusselt number increases marginally with temperature. Similar to the low temperature flow results, the 12.7mm OD tube yields slightly higher Nusselt numbers than the 9.5mm OD tube.

5.3. Comparison with Two-Layer Model

The ETC correlation developed for the wall-adjacent layer was modified to incorporate the presence of radiation at higher operating temperatures in an attempt to predict the trends observed

in the experimental data. Various works have attempted to model the radiation within a static particle bed, ranging widely in complexity; due to the complexity of radiation heat transfer and the random packing arrangement of particles in a bed, however, a clear modelling approach has not yet been determined. As with all models, there is a balancing act between accuracy and simplicity. Cheng & Yu [31] discuss the various radiation modelling techniques for particle beds and the drawbacks of each. Furthermore, the radiation heat transfer between a heated wall and the wall-adjacent layer of particles has not been explored in much detail. The radiation model developed for the wall-adjacent layer in the present study sought to provide a general understanding of the radiation contribution to the overall heat transfer to the flow; therefore, the resulting model is relatively simple.

An enclosure analysis was used as the basis for the model development. The particle bed/flow near the wall was classified into different particle layers, as defined in Figure 5.8. The first layer (i.e. the wall-adjacent layer) has a thickness of a particle radius; all other layers have a thickness of a particle diameter. Each layer of particles was considered a surface of the enclosure, with the surface areas of the particles in the layer summed to find the total surface area (as indicated by the different colors in Figure 5.8). The enclosure utilized consisted of four surfaces: the wall and three particle layers.

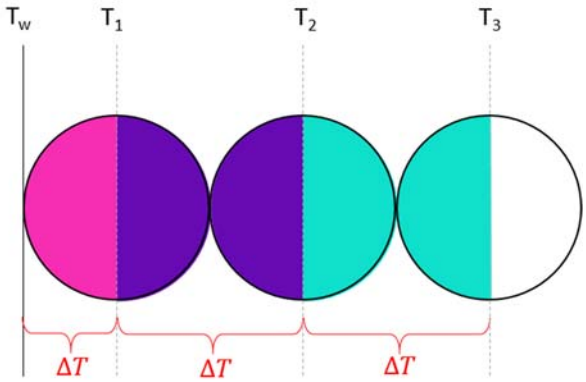

Figure 5.8: Schematic of layers used to define radiation from the wall.

According to Pitso [52], the radiation from a single sphere in a randomly packed bed penetrates no more than 2-3 particle diameters. Therefore, the radiation from the wall to the bed was assumed to penetrate a similar distance. For simplicity, the wall and particles were taken as blackbodies. The heat flux leaving the wall in the negative radial direction can be written as

$$q''_{wall,rad} = F_{w-1}\sigma(T_w^4 - T_1^4) + F_{w-2}\sigma(T_w^4 - T_2^4) + F_{w-3}\sigma(T_w^4 - T_3^4) \quad (48)$$

where $q''_{wall,rad}$ represents the radiation heat flux leaving the wall, F_{w-j} represents the view factor from the wall to the j^{th} layer, T_j represents the average temperature of the j^{th} layer, and σ represents the Stefan-Boltzmann constant. If $(T_w - T_j) \ll 4\overline{T_{wJ}}^2$ (where $\overline{T_{wJ}}$ represents the average temperature of T_w and T_j), then $(T_w^4 - T_j^4) \approx 4\overline{T_{wJ}}^3(T_w - T_j)$. This simplification seemed appropriate for the flows studied since the temperature drop across a couple particle diameters was much less than the wall temperature. A linear temperature distribution was assumed across layers 2 and 3 (i.e. $(T_1 - T_2) = \Delta T$, $(T_2 - T_3) = \Delta T$, while the temperature gradient across layer 1 was assumed twice that of the other layers due to the increased thermal resistance adjacent to the wall (i.e. $(T_w - T_1) = \Delta T$). Finally, assuming $\Delta T \ll T_w$, $\overline{T_{wJ}} \approx T_w$. After incorporating all the listed assumptions, Equation 48 can be rewritten as

$$q''_{wall,rad} = 4\sigma T_w^3 \Delta T[F_{w-1} + 2F_{w-2} + 3F_{w-3}\,] \quad (49)$$

To incorporate the radiation contribution to the total heat transfer through the wall-adjacent layer with the conduction contribution, an effective thermal conductivity due to radiation was desired. By comparing Equation 49 with Fourier's Law, the thermal conductivity due to radiation can be defined as

$$k_{wa,rad} = 4\sigma r_p T_w^3[F_{w-1} + 2F_{w-2} + 3F_{w-3}\,] \quad (50)$$

Note that Equation 50 is a function of the wall temperature and not the mean flow temperature. In Section 5.2, the mean flow temperature was used to characterize the heat transfer coefficients

measured, as well as approximate the thermal properties of the flow. However, when calculating the radiation contribution, using the mean temperature to approximate $k_{wa,rad}$ will underestimate the contribution from radiation. Similarly, when calculating the wall-adjacent layer ETC, it seems more appropriate to use the wall temperature to determine the thermal properties for the wall-adjacent layer. From a design standpoint, the expected heat transfer to a flow at a desired wall operating temperature may be more valuable, if designing based on the maximum operating temperature of the tube, for example. When calculating the heat transfer to a flow using the two-layer model, the bulk thermal conductivity will be overestimated when using the wall temperature, yielding a slightly lower Nusselt number than may actually be expected. The underestimation is, however, less than if the mean temperature was used to calculate all thermal properties and the radiation contribution. Therefore, the wall temperature was used to calculate the heat transfer to the flows.

In order to calculate the thermal conductivity due to radiation, the view factors from the wall to each layer of particles is required. StarCCM+ was used to calculate the view factors to the surface of each layer. The centroid data from the DEM flows discussed in Section 3.2 was used to create a solid model of the particles in the near-wall region using SolidWorks (Figure 5.9). The surface of each particle was split according to the cylindrical surface "cutting" the particle at the boundary of each layer (Figure 5.9b). The total surface area for each layer was then assigned to the sum of all the individual surfaces in the associated layer. The different colors in Figure 5.9 indicate the surfaces attributed to each layer. The process of splitting the particle surfaces was a very time intensive and difficult process, as each particle cut by the cylindrical surface had to be manually selected; as such, ensuring that all particles were selected was difficult due to the random packing of the bed. Therefore, due to the large number of particles present around the tube

diameter, only a section of the tube was used. As a result, there was a small amount of "leakage" to the top, bottom and side surfaces.

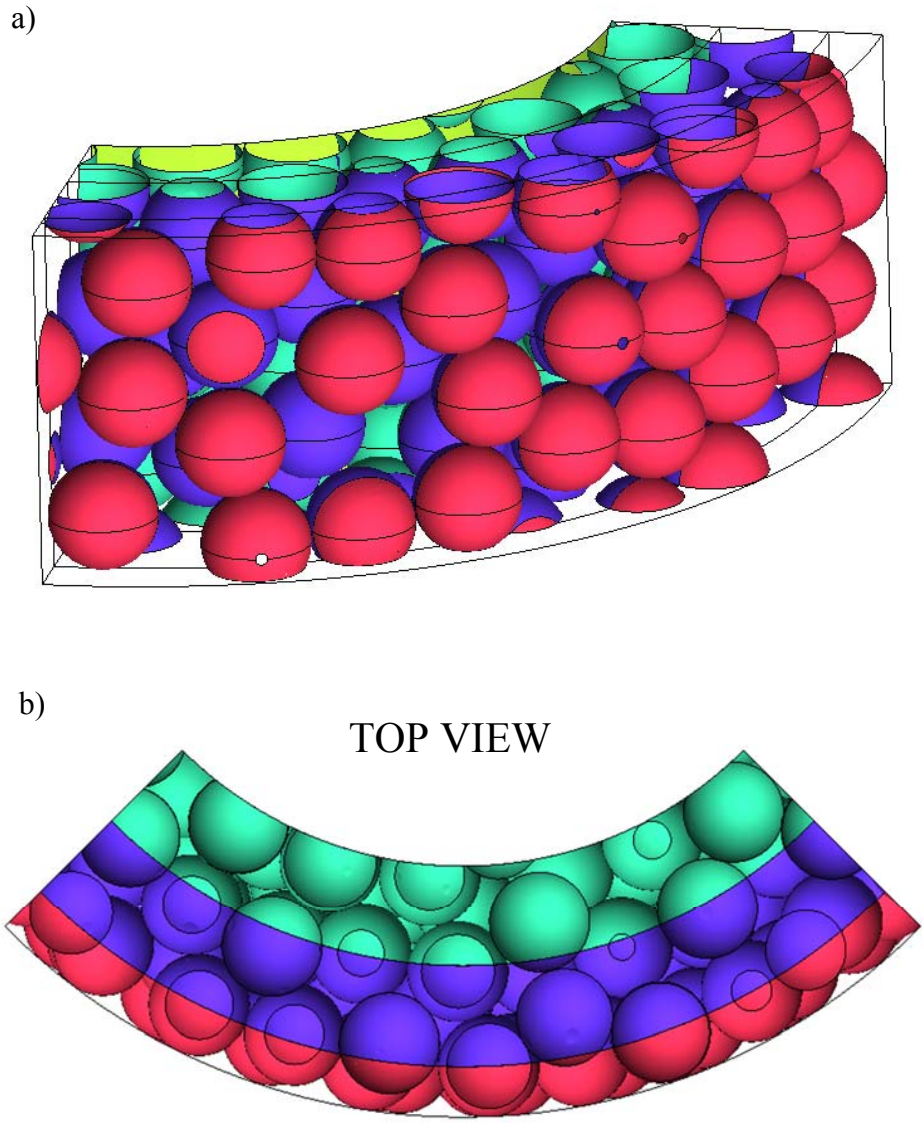

Figure 5.9: Particle bed used to calculate the view factors from the wall to each layer. Each color denotes the surfaces associated with each layer.

Once the solid model was created and the surfaces were split, the void spaces and surfaces were meshed. The ray-tracing algorithm of StarCCM+ was used to examine the radiation heat transfer between the surfaces and extract the view factors to each surface. Table 5.3 summarizes

the system configuration used and the resulting view factors calculated. Note that the leakage was incorporated into the primary view factors, such that the view factors summed to one for the enclosure.

Table 5.3: Properties of View Factor Simulation.

Property	Value
Tube Diameter (mm)	7.75
Particle Diameter (mm)	0.60
Mean Flow Velocity (m/s)	0.016
F_{w-1}	0.80
F_{w-2}	0.18
F_{w-3}	0.02

Utilizing the view factors, the radiation thermal conductivity was calculated for wall temperatures up to 1100°C for each system configuration tested at high operating temperatures. Assuming the radiation heat transfer acts in parallel with the conduction heat transfer, the total ETC for the wall adjacent layer is the sum of the two thermal conductivity components (i.e. $k_{wa,total} = k_{wa} + k_{wa,rad}$). The heat transfer to the flow as a function of the wall temperature was calculated using the two-layer model and the bulk thermal conductivity correlations developed for high temperatures (Table 5.2). Figure 5.10 displays the experimental results for each system configuration, along with the corresponding values predicted by the two-layer model. The model predictions calculated without radiation in the bulk and the wall-adjacent layer are also plotted so the relative contribution from radiation is easily observed.

The two-layer model with radiation included shows good agreement with the experimental data for most all test cases. The largest variation is observed at the hottest temperatures; however, the model agrees with the experimental data within experimental uncertainty. As expected, the contribution from radiation is negligible at low temperatures and begins to grow at higher

temperatures. For the systems tested, inclusion of radiation increases the heat transfer coefficient by up to 29%.

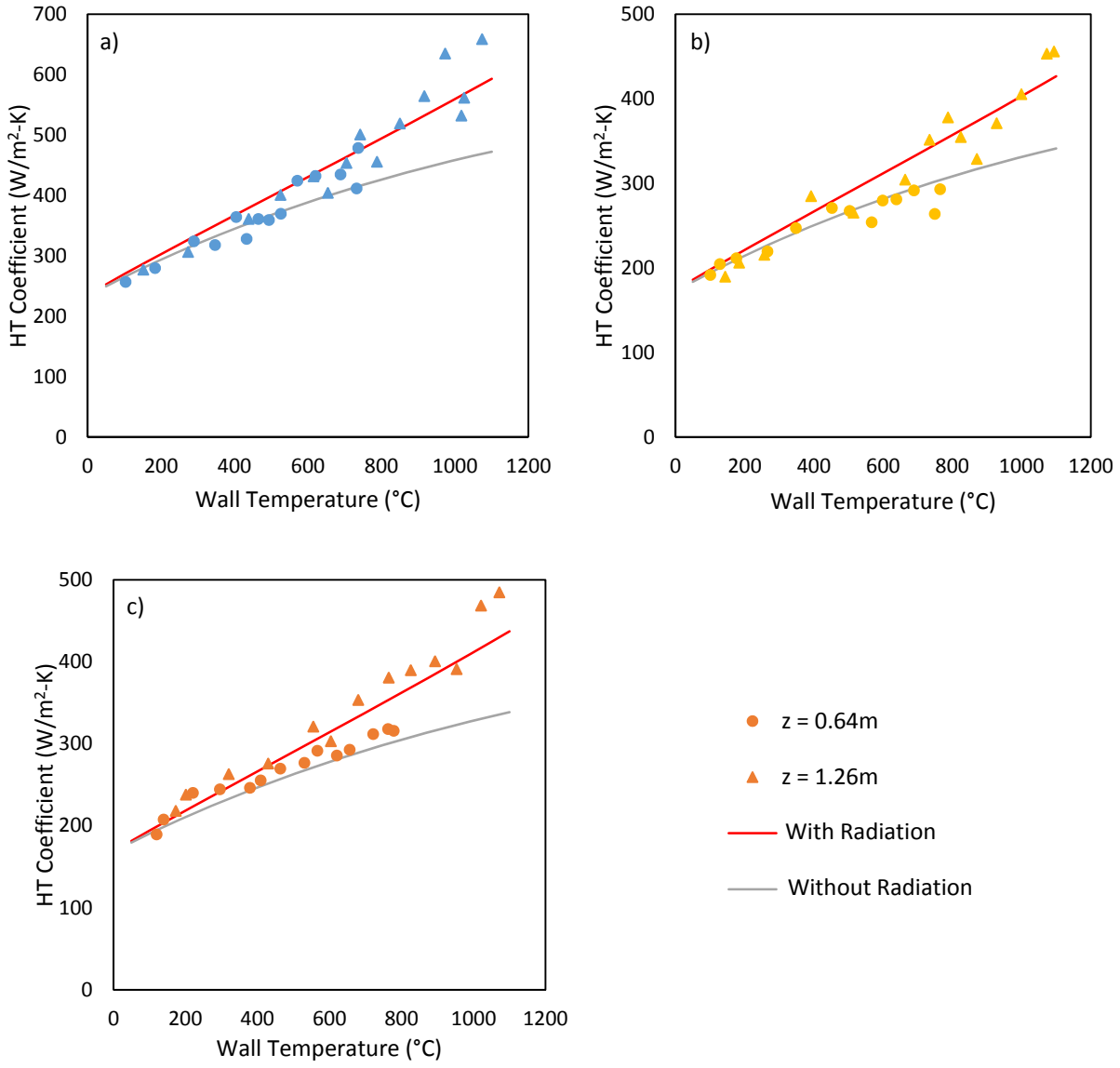

Figure 5.10: Comparison of experimental data and two-layer model for a) 9.5mm OD tube with 270µm Z-S particles, b) 12.7mm OD tube with 270µm Z-S particles, and c) 12.7mm OD tube with 320µm Z-S particles.

As discussed in Section 2.2.3.3, for a static bed, the relative contribution from radiation surpasses the conduction contribution at higher temperatures for particle diameters greater than 2.0mm. For smaller particles, conduction is the dominant heat transfer mechanism (as

demonstrated in Figure 2.11). Figure 2.12, however, demonstrated how drastically radiation could enhance the heat transfer within a bed for larger particle diameters. A similar trend was observed for $k_{wa,total}$ and the heat transfer coefficient. The relative contribution of radiation to the total heat transfer for a larger particle diameter (2.0mm) is displayed in Figure 5.11. Note that the tube-to-particle diameter ratio is the same as that in Figure 5.10a to remove any variation due to the relative size of the bulk layer. A 63% increase in the heat transfer coefficient is observed with the inclusion of radiation for the larger particle diameters, corroborating the observation that radiation has a more significant role for larger particle diameters. Note that the larger particle diameters yield lower heat transfer coefficients because a larger tube diameter was used to maintain the same tube-to-particle diameter ratio.

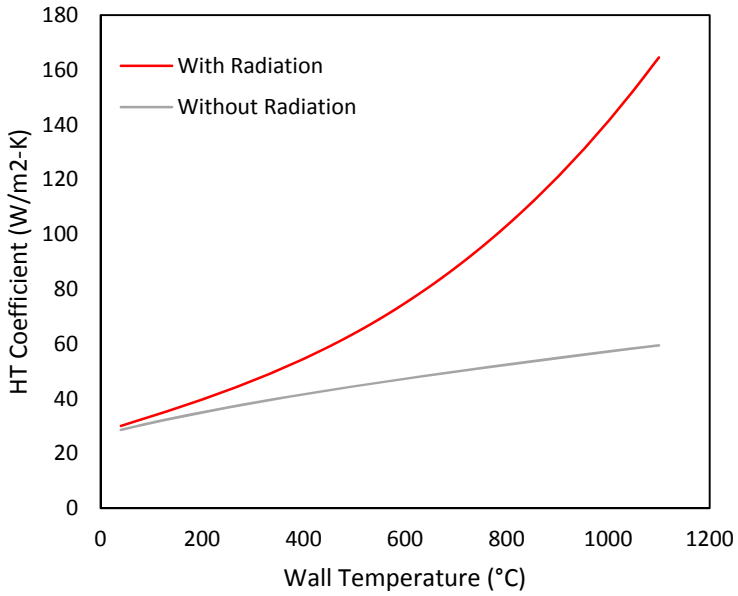

Figure 5.11: Relative contribution of conduction and radiation to the heat transfer to a flow composed of 2.00mm diameter Z-S particles. Trends calculated using the two-layer model with R_i = 28.2mm and U = 0.015m/s.

The variation in the heat transfer to a flow as a function of particle diameter (for a constant tube diameter) is shown in Figure 5.12. At low temperatures, the smaller particles demonstrate

superior heat transfer, as the thermal conductivity of both the bulk and wall-adjacent layers are similar for all particle diameters. Recall from Figure 4.3 that the Nusselt number increases with increasing tube-to-particle diameter ratio, which corresponds to a decrease in particle diameter for a given tube diameter. As the temperature increases, however, the thermal conductivity for the larger particles increases at a faster rate due to the increased contribution from radiation, ultimately yielding superior heat transfer at higher temperatures. When examining these results for different particle diameters, it is important to remember that the values demonstrate the best possible heat transfer, as all surfaces were taken as blackbodies. Future work should seek to validate these trends experimentally.

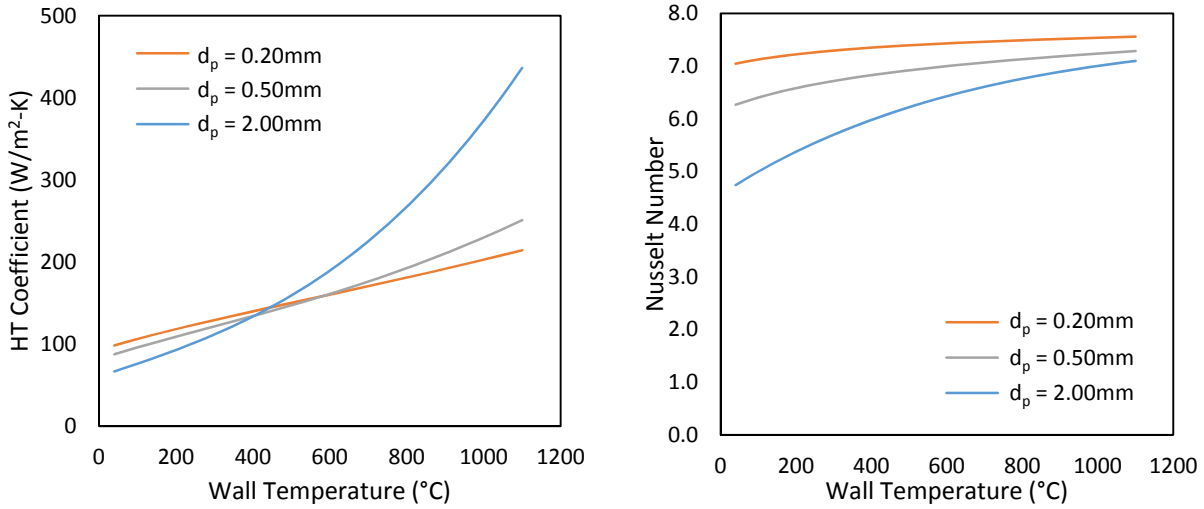

Figure 5.12: Heat transfer coefficient and Nusselt number as a function of wall temperature and particle diameter. Trends calculated using the two-layer model with R_i = 10mm and U = 0.015m/s.

All the high temperature results discussed thus far have been for relatively slow flows (U = 0.014 m/s). Initially, the penetration of radiation into the bed was thought to increase with increasing flow rate due to the reduced packing fraction in the wall-adjacent layer, manifesting itself in the view factors. Testing lower view factors for faster flow rates yielded a negligible

change in the heat transfer coefficient calculated for our system configuration. The variation was slightly greater for bigger particles. Due to the time-intensive nature of calculating the view factors, examination of the change in view factor was beyond the scope of the present study.

Chapter 6
Conclusions

The present study sought to gain an understanding of the physics governing the heat transfer to dense granular flows through vertical cylindrical tubes, as well as examine their applicability for use as a heat transfer fluid for concentrated solar power tower applications. An experimental apparatus was designed and built to measure the heat transfer to such flows, examining how the tube diameter, particle diameter, and flow rate effected the heat transfer. Unlike previous works, which quantified the heat transfer to dense flows using the heat transfer coefficient based on the wall-inlet temperature difference, the present work quantified the heat transfer using a heat transfer coefficient based on the wall-mean temperature difference. For long tubes, the use of the mean temperature provides a more accurate representation of the temperature difference driving the heat transfer to the flow. Presumably, previous works used the inlet temperature due to the ease of measurement as compared with measuring the local mean temperature.

As observed in previous studies of dense granular flows, our particulate flows demonstrated inferior heat transfer compared with a continuum flow. It is well accepted in the literature that the more structured arrangement of particles adjacent to the heated surface controls

the heat transfer to the flow. Attempts to model this behavior involve representing the flow as a continuum with an additional thermal contact resistance at the heated surface. A similar modeling approach was taken in the present work to predict the heat transfer to flows through cylindrical tubes. A two-layer model was proposed, which divides the flow into two layers: a bulk layer, which encapsulates the majority of the flow, and a thin layer adjacent to the wall (thickness of a particle radius), which captures the increased thermal resistance at the heated surface. Unlike previous models, which model the contact resistance using empirical parameters or correlations derived for static beds, an effective thermal conductivity (ETC) correlation for the wall-adjacent layer was derived for flows.

Discrete Element Method (DEM) simulations performed in lab show that both the packing fraction in the wall-adjacent layer and the number of particles in contact with the wall decrease with increasing flow rate. Since the heat transfer to a particle decreases drastically as soon as the particle loses contact with the wall, it was important to consider heat transfer to both particles in contact with the wall and particles not in contact. Using a parallel circuit of thermal resistances, accounting for heat transfer to particles in contact with the wall, particles not in contact with the wall, and heat transfer through void spaces where no particle is present, an expression for the ETC of the wall-adjacent layer was derived. The resulting correlation depends on the tube diameter, particle diameter, thermal conductivities of the solid material and gas, the packing fraction of the wall-adjacent layer, and the number of particles in contact with the wall.

DEM simulations performed for various tube and particle diameters were used to examine the packing fraction and number of contact particles as a function of flow rate and system configuration. Using the DEM data, empirical correlations were developed to capture the variation with flow rate, tube diameter, and particle diameter. The correlations developed are applicable for

a very small range of tube and particle diameters, as the DEM simulations were tailored to match the experimental systems tested. Extrapolation beyond the systems tested may lead to uncertainties. Future work should seek to test a broader range of system configurations to expand the applicability of the correlations developed.

Incorporating the ETC correlation into the two-layer model, the heat transfer to the flow predicted by the model was compared with the experimental results obtained. The two-layer models suggests that the heat transfer to the flow increases with increasing tube diameter and/or decreasing particle diameter due to the decrease in the relative size of the wall-adjacent layer. Experimentally, the effect of particle diameter was tested using three different particle diameters, ranging from 140 to 320μm. At low operating temperatures (<200°C), the particle diameter appeared to have little effect on the heat transfer. Due to experimental uncertainty (up to 14%), however, the variation predicted by the model was not discernable. A larger range of particle diameters would allow the effect of particle diameter to be more easily examined; due to the high cost of the particles used, however, this was not possible during the present study. The effect of tube diameter (tested using two different tubes) on the heat transfer to the flow was more noticeable in the experimental results and was captured well by the two-layer model. In all experimental configurations, the heat transfer to the flow appeared to increase slightly with increasing flow rate; however, due to the experimental uncertainty, this trend could not be claimed with certainty. The two-layer model suggests that the heat transfer to the flow decreases slightly with increasing flow rate due to the decrease in packing fraction and number of particle contacts. This trend was captured within the uncertainty of the experimental data.

To test the versatility of the ETC correlation developed, the correlation was used to predict the heat transfer to rectangular chute flows found in the literature. The ETC correlation was

modified slightly to accommodate the difference in the geometry cross-section. Incorporating the ETC correlation into the model developed by Sullivan & Sabersky [16] showed good agreement with the experimental results of both Sullivan & Sabersky and Natarajan & Hunt [17] for flows of glass beads. The model was able to capture not only the increase in heat transfer observed with increasing flow rate, but also the decrease observed at very fast flow rates.

The final portion of the study focused on the heat transfer to dense flows at operating temperatures more characteristic of concentrated solar power towers. The effect of temperature on the heat transfer to the flow was studied for a single flow rate, using different tube and particle diameters. Each system tested demonstrated an increase in heat transfer with increasing temperature due to enhanced thermal properties at higher temperatures. A simple ETC correlation was developed to account for radiation in the wall-adjacent layer at very high temperatures. The two-layer model predictions agreed well with the experimental results. For the small particle diameters tested, radiation did not contribute much to the overall heat transfer. The radiation contribution is expected to grow, however, with increasing particle diameter, as the size of the void spaces grow. Future work should investigate the effect of particle diameter, as well as flow rate, in more detail, as these parameters may have a significant effect on the heat transfer to dense flows at high operating temperatures.

The observations made throughout this work help increase our understanding of the parameters that effect the heat transfer to dense granular flows. The agreement between the model developed and experimental results shows promise for the ETC correlation developed. In its current form, the ETC correlation is limited by an understanding of the variation in packing fraction and number of particle-wall contacts with system parameters. An understanding of the mechanics that control the behavior of each parameter, as well as a study into the variation across

a wider range of system parameters would greatly expand the applicability of the ETC correlation derived. The model could possibly be expanded beyond vertical flows to flows down an inclined plane, as the underlying physics of the heat transfer behavior is the same; the packing fraction and number of contacts would need to be modified, however, to account for the denser packings present due to gravitational packing. Ultimately, we anticipate our model to serve as a gateway to analyzing the overall heat transfer behavior of dense granular flows and to serve as a means to identify other parameters that could be modified to improve the overall performance of dense flow systems.

REFERENCES

[1] D. L. Chandler, "Vast amounts of solar energy radiate to the Earth, but tapping it cost-effectively remains a challenge." MIT News, Cambridge, MA, 2011.

[2] NREL, "Concentrating Solar Power Projects in the United States," 2014. [Online]. Available: http://www.nrel.gov/csp/solarpaces/.

[3] C. K. Ho, "Advances in central receivers for concentrating solar applications," *Sol. Energy*, vol. 152, pp. 38–56, 2017.

[4] G. Flamant, D. Gauthier, H. Benoit, J. L. Sans, R. Garcia, B. Boissière, R. Ansart, and M. Hemati, "Dense suspension of solid particles as a new heat transfer fluid for concentrated solar thermal plants: On-sun proof of concept," *Chem. Eng. Sci.*, vol. 102, pp. 567–576, 2013.

[5] C. K. Ho, J. M. Christian, J. Yellowhair, K. Armijo, W. J. Kolb, S. Jeter, M. Golob, and C. Nguyen, "Performance evaluation of a high-temperature falling particle receiver," in *ASME 2016 Power & Energy Conference*, 2016.

[6] A. B. Morris, Z. Ma, S. Pannala, and C. M. Hrenya, "Simulations of heat transfer to solid particles flowing through an array of heated tubes," *Sol. Energy*, vol. 130, pp. 101–115, 2016.

[7] G. MiDi, "On dense granular flows.," *Eur. Phys. journal. E*, vol. 14, no. 4, pp. 341–365, 2004.

[8] S. B. Savage, "The Mechanics of Rapid Granular Flows," in *Advances in Applied Mechanics*, vol. 24, J. W. Hutchinson and T. Y. Wu, Eds. Academic Press, Inc., 1984, pp. 289–366.

[9] W. Van Antwerpen, C. G. Du Toit, and P. G. Rousseau, "A review of correlations to

model the packing structure and effective thermal conductivity in packed beds of mono-sized spherical particles," *Nucl. Eng. Des.*, vol. 240, no. 7, pp. 1803–1818, 2010.

[10] R. Yusuf, M. C. Melaaen, and V. Mathiesen, "Convective Heat and Mass Transfer Modeling in Gas-Fluidized Beds," *Chem. Eng. Technol.*, vol. 28, no. 1, pp. 13–24, 2005.

[11] D. Garrett and H. Ban, "Compressive pressure dependent anisotropic effective thermal conductivity of granular beds," *Granul. Matter*, vol. 13, no. 5, pp. 685–696, 2011.

[12] G. Weidenfeld, Y. Weiss, and H. Kalman, "A theoretical model for effective thermal conductivity (ETC) of particulate beds under compression," *Granul. Matter*, vol. 6, no. 2–3, pp. 121–129, 2004.

[13] S. S. Hsiau and M. L. Hunt, "Kinetic Theory Analysis of Flow-Induced Particle Diffusion and Thermal Conduction in Granular Material Flows," *J. Heat Transfer*, vol. 115, no. 3, pp. 541–548, 1993.

[14] V. V. R. Natarajan and M. L. Hunt, "Kinetic theory analysis of heat transfer in granular flows," *Int. J. Heat Mass Transf.*, vol. 41, no. 13, pp. 1929–1944, 1998.

[15] M. S. Brinn, S. J. Friedmen, and F. a Gluckert, "Heat Transfer to Granular Materials," *Ind. Eng. Chem.*, pp. 1050–1061, 1948.

[16] W. N. Sullivan and R. H. Sabersky, "Heat transfer to flowing granular media," *Int. J. Heat Mass Transf.*, vol. 18, pp. 97–107, 1975.

[17] V. V. R. Natarajan and M. L. Hunt, "Heat Transfer in Vertical Granular Flows," *Experimental Heat Transfer*, vol. 10, no. 2. pp. 89–107, 1997.

[18] J. K. Spelt, C. E. Brennen, and R. H. Sabersky, "Heat Transfer To Flowing Granular Material," *Int. J. Heat Mass Transf.*, vol. 3, pp. 791–796, 1981.

[19] J. S. Patton, R. H. Sabersky, and C. E. Brennen, "Convective heat transfer to rapidly

flowing, granular materials," *Int. J. Heat Mass Transf.*, vol. 29, no. 8, pp. 1263–1269, 1986.

[20] H. Ahn, "Experimental and analytical investigations of granular materials: shear flow and convective heat transfer," California Institute of Technology, 1989.

[21] E. U. Schlünder, "Heat transfer to packed and stirred beds from the surface of immersed bodies," *Chem. Eng. Process.*, vol. 18, no. 1, pp. 31–53, 1984.

[22] A. O. O. Denloye and J. S. M. Botterill, "Heat transfer in flowing packed beds," *Chem. Eng. Sci.*, vol. 32, no. 5, pp. 461–465, 1977.

[23] H. S. Mickley and D. F. Fairbanks, "Mechanism of heat transfer to fluidized beds," *AIChE J.*, vol. 1, no. 3, pp. 374–384, 1955.

[24] A. P. Baskakov, "The mechanism of heat transfer between a fluidized bed and a surface," *Int. Chem. Eng.*, vol. 4, pp. 320–324, 1964.

[25] S. Yagi and D. Kunii, "Studies on heat transfer in packed beds," in *International Heat Transfer Conference*, 1961, vol. IV, pp. 750–759.

[26] E. U. Schlünder, "Particle Heat Transfer," in *Proceedings of the 7th International Heat Transfer Conference*, 1982, pp. 195–211.

[27] R. Ernst, "Der Mechanismus des Wärmeüberganges an Wärmeaustauschern in Fließbetten (Wirbelschichten)"," *Chemie Ing. Tech.*, no. 3, pp. 166–173, 1959.

[28] J. S. M. Botterill, M. H. D. Butt, G. L. Cain, and K. A. Redish, "The effect of gas and solids thermal properties on the rate of heat transfer to gas-fluidized beds," in *Proceeding of the International Symposium on Fluidization*, 1967, pp. 442–457.

[29] A. B. Morris, S. Pannala, Z. Ma, and C. M. Hrenya, "A conductive heat transfer model for particle flows over immersed surfaces," *Int. J. Heat Mass Transf.*, vol. 89, pp. 1277–1289,

2015.

[30] S. Yagi and D. Kunii, “Studies on Effective Thermal Conductivities in Packed Beds,” *A.I.Ch.E J.*, vol. 3, no. 3, pp. 373–381, 1957.

[31] G. J. Cheng and A. B. Yu, “Particle Scale Evaluation of the Effective Thermal Conductivity from the Structure of a Packed Bed: Radiation Heat Transfer,” *Ind. Eng. Chem. Res.*, vol. 52, pp. 12202–12211, 2013.

[32] H. A. Beverloo, H. A. A. Leniger, and J. Van De Velde, “The flow of granular solids through orifices,” *Chem. Eng. Sci.*, vol. 15, no. 3–4, pp. 260–269, Sep. 1961.

[33] Specialty Products & Insulation, “Mineral Wool Pipe Insulation,” 2014. [Online]. Available: http://www.spi-co.com/pdf/Mineral-Wool-Pipe-Insulation-Datasheet.pdf.

[34] “Mineral Wool Insulation,” *Engineering Toolbox*. [Online]. Available: https://www.engineeringtoolbox.com/mineral-wool-insulation-k-values-d_815.html.

[35] M. T. Ceramics, “Cerablanket.” [Online]. Available: http://www.morganthermalceramics.com/media/3993/cerablanket_cerachem_cerachromeblanket_english.pdf.

[36] L. C. Burmeister, *Convective Heat Transfer*, 2nd ed. New York, NY: John Wiley & Sons, Inc., 1993.

[37] F. Chevoir, M. Prochnow, P. Moucheront, F. da Cruz, F. Bertrand, J.-P. Guilbaud, P. Coussot, and J.-N. Roux, “Dense granular flows in a vertical chute,” in *Powders and Grains*, 2001, pp. 399–402.

[38] Y. N. Chilamkurti and R. D. Gould, “Experimental and computational studies of gravity-driven dense granular flows,” in *International Mechanical Engineering Congress & Exposition*, 2015.

[39] Y. N. Chilamkurti and R. D. Gould, “Discrete element studies of gravity-driven dense granular flows in vertical cylindrical tubes,” in *ASME 2016 Power & Energy Conference*, 2016.

[40] High Temp Metals, “Inconel 625 Technical Data,” 2015. [Online]. Available: http://www.hightempmetals.com/techdata/hitempInconel625data.php.

[41] Y. S. Muzychka, E. Walsh, and P. Walsh, “Simple Models for Laminar Thermally Developing Slug Flow in Noncircular Ducts and Channels,” *J. Heat Transfer*, vol. 132, no. 11, p. 111702 1-10, 2010.

[42] M. W. Chase, *NIST-JANAF Thermochemical Tables*, 4th ed. American Institute of Physics, American Chemical Society, 1998.

[43] A. M. Abyzov, A. V. Goryunov, and F. M. Shakhov, “Effective thermal conductivity of disperse materials. I. Compliance of common models with experimental data,” *Int. J. Heat Mass Transf.*, vol. 67, pp. 752–767, 2013.

[44] W. Van Antwerpen, P. G. Rousseau, and C. G. Du Toit, “Multi-sphere Unit Cell model to calculate the effective thermal conductivity in packed pebble beds of mono-sized spheres,” *Nucl. Eng. Des.*, vol. 247, pp. 183–201, 2012.

[45] H. S. Katz and J. V Milewski, Eds., *Handbook of Fillers for Plastics*. Van Nostrand Reinhold, 1987.

[46] J. F. Shackelford and W. Alexander, Eds., *CRC Materials Science and Engineering Handbook*, 3rd ed. CRC Press, 2001.

[47] M. Adams, “Thermal Conductivity: III, Prolate Spheroidal Envelope Method,” *J. Am. Ceram. Soc.*, vol. 37, no. 2, pp. 74–79, 1954.

[48] B. Legawiec and D. Ziolkowski, “Structure, voidage and effective thermal conductivity of

solids within near-wall region of beds packed with spherical pellets in tubes," *Chem. Eng. Sci.*, vol. 49, no. 15, pp. 2513–2520, 1994.

[49] M. Sperl and H. A. Janssen, "Experiments on corn pressure in silo cells - Translation and comment of Janssen's paper from 1895," *Granul. Matter*, vol. 8, no. 2, pp. 59–65, 2006.

[50] A. Mughal, H. K. Chan, D. Weaire, and S. Hutzler, "Dense packings of spheres in cylinders: Simulations," *Phys. Rev. E - Stat. Nonlinear, Soft Matter Phys.*, vol. 85, no. 5, 2012.

[51] P. Zehner and E. U. Schlünder, "Thermal conductivity of granular materials at moderate temperatures," *Chemie Ing. Tech.*, vol. 44, no. 23, pp. 1303–1308, 1972.

[52] L. Pitso, "Characterisation of long range radiation heat transfer in packed pebble beds," The North-West University, 2011.

[53] H. G. Cetin, G. Ozturk, Y. Celebi, and A. Dindar, "Design, calibration and measurement uncertainty analysis of a tension measurement test system," in *2015 IEEE International Instrumentation and Measurement Technology Conference (I2MTC) Proceedings*, 2015.

[54] D. C. Montgomery, G. C. Runger, and N. F. Hubele, *Engineering Statistics*, 3rd ed. John Wiley & Sons, Inc., 2004.

[55] S. Singh, P. K. Jain, and Rizwan-uddin, "Analytical solution to transient heat conduction in polar coordinates with multiple layers in radial direction," *Int. J. Therm. Sci.*, vol. 47, no. 3, pp. 261–273, 2008.

APPENDICES

Appendix A – Uncertainty Calculations

The uncertainty associated with all experimental measurements was examined as a way to understand how best to interpret the trends observed. Uncertainty was calculated for the effective thermal conductivity measurements and the fluid flow measurements. For all calculations, both random and instrumental uncertainty were considered. Relative error (S_x) was used to represent the uncertainty in each parameter (x). Relative error was defined as

$$S_x^2 \propto \left(\frac{\sigma_x}{x}\right)^2 \tag{51}$$

where σ_x^2 represents the variance in parameter x. All reported uncertainties are within a 95% confidence interval. The relative error associated with a function (y) of multiple parameters was determined using

$$S_y^2 = \left(\frac{\sigma_y}{y}\right)^2 = \left(\frac{1}{y}\frac{\partial y}{\partial x_1}\right)^2 \sigma_{x_1}^2 + \left(\frac{1}{y}\frac{\partial y}{\partial x_2}\right)^2 \sigma_{x_2}^2 + \cdots \tag{52}$$

Effective Thermal Conductivity

The effective thermal conductivity measured using the concentric tube apparatus was calculated based on a logarithmic regression fit to the temperature profile measured (Equation 10). The voltage, current, and length of the heated section were assumed to be known with certainty. Therefore, the relative uncertainty in the bulk ETC was determined using

$$S_{k_b}^2 = \left(\frac{\sigma_{k_b}}{k_b}\right)^2 = \left(\frac{\sigma_{a_b}}{a_b}\right)^2 \tag{53}$$

where a_b represents the coefficient from the regression. The type K thermocouples (from Omega) utilized are specified to have a tolerance of 0.4% of the temperature measured. To incorporate the instrumental uncertainty associated with the temperature measurements, an approach based on the Monte Carlo technique was applied. An array of temperature values was randomly generated based

on a normal distribution for each radial position. The values were generated based on the average temperature measured at each position; the standard deviation was associated with the instrumental uncertainty and the standard deviation of the temperatures measured. Logarithmic regressions were calculated for each set of temperature values in the array, then the coefficients obtained from each regression were averaged and used to calculate the uncertainty in a_b. Across all measurements, the relative uncertainty was found to be less than 9%.

In order to calculate the Nusselt number, the linear regression fit to the CT apparatus data was used to predict the bulk ETC. The uncertainty in the predicted ETC was calculated based on two parts: the average uncertainty of the individual ETC values and the uncertainty associated with using a linear regression to predict a value [53], [54]. The combined relative uncertainty was calculated based on the sum of the squares of the individual components and found to be less than 11%.

Fluid Flow Measurements

The heat transfer coefficient calculated for the flows depends on the input heat flux and the wall and mean temperatures. In most cases, the uncertainty in the wall temperature was calculated based on the standard deviation observed in the temperature measurements and the instrumental uncertainty associated with the thermocouples, yielding a combined uncertainty. In the instances when the linear regression fit to the wall temperature data was used to estimate the temperature at the desired axial position, an approach similar to that used to predict the bulk ETC was implemented. The average uncertainty of the individual wall temperature values (each of which included both random and instrumental uncertainty) was combined with the uncertainty

associated with predicting a value from a linear regression. The wall temperatures demonstrated uncertainties less than 1%.

The mean temperature was calculated based on the quadratic regression fit to the temperature profile measured (Equation 4). Assuming the radius of the tube was known with certainty, the relative uncertainty associated with the mean temperature was calculated based on the uncertainty in the regression coefficients using

$$S_{T_m}^2 = \left(\frac{\sigma_{T_m}}{T_m}\right)^2 = \frac{\frac{1}{4}R_i^4\sigma_{C_1}^2 + \frac{4}{9}R_i^2\sigma_{C_2}^2 + \sigma_{C_3}^2}{T_m^2} \tag{54}$$

Using the Monte Carlo-based approach utilized for the bulk ETC measurements to incorporate both the random and instrumental uncertainties, the relative uncertainty associated with the mean temperature was found to be less than 1%.

The heat flux entering the flow was calculated based on the input heating power and the heat losses through the insulation. Assuming the tube radius, insulation radius, tube length, and thermal conductivities of the ceramic and mineral wool insulations were known with certainty, the relative uncertainty in the wall heat flux was expressed as

$$S_{q''_{wall}}^2 = \left(\frac{\sigma_{q''_{wall}}}{q''_{wall}}\right)^2 = \frac{I^2\sigma_V^2 + V^2\sigma_I^2}{\left(VI - \frac{2\pi L(T_{w,o} - T_{wool})}{\frac{\ln(R_{cer}/R_o)}{k_{cer}} + \frac{\ln(R_{wool}/R_{cer})}{k_{wool}}}\right)^2} + \left(\frac{2\pi L}{VI\left(\frac{\ln(R_{cer}/R_o)}{k_{cer}} + \frac{\ln(R_{wool}/R_{cer})}{k_{wool}}\right) - 2\pi L(T_{w,o} - T_{wool})}\right)^2 \left(\sigma_{T_{w,o}}^2 + \sigma_{T_{wool}}^2\right) \tag{55}$$

The uncertainty in the temperature of the insulation (T_{wool}) was based on the standard deviation of the temperatures measured. The uncertainty in both the current and the voltage were dependent on random and instrumental error. The instrumental uncertainty in the current was taken to be

±0.1A, while the uncertainty in the voltage was taken to be ±0.005V, based on the precision of the measurement instruments. The uncertainty in the wall heat flux was found to be within 1.5%.

Using the uncertainties discussed above, the relative uncertainty in the heat transfer coefficient and Nusselt number were determined using

$$S_h^2 = \left(\frac{\sigma_h}{h}\right)^2 = \left(\frac{\sigma_{q''_{wall}}}{q''_{wall}}\right)^2 + \frac{\sigma_{T_w}^2 + \sigma_{T_m}^2}{(T_w - T_m)^2} \tag{56}$$

$$S_{Nu}^2 = \left(\frac{\sigma_{Nu}}{Nu}\right)^2 = \left(\frac{\sigma_h}{h^2}\right)^2 + \left(\frac{\sigma_{k_b}}{k_b}\right)^2 \tag{57}$$

The relative error associated with the heat transfer coefficient was within 15%, while the error associated with the Nusselt number was within 17%.

Appendix B – Two-Layer Model Derivation

The following section describes the derivation performed to obtain the Nusselt number correlation associated with the two-layer model. The work of Singh et al. [55] was used as a guide for solving the transient conduction equation for a system with multiple layers. Since the problem in the present work assumes a plug flow, the transient conduction equation can be written in terms of the axial position and mean flow velocity. The temperature, $T_j(r,z)$, was rewritten as $T_j(r,z) = \overline{T_j}(r,z) + S_j(r) + Z_j(z)$ so the non-homogeneous "transient" problem could be separated into a "transient" homogenous problem and a "steady-state" non-homogeneous problem. The problem was thus rewritten as

Transient Homogeneous

$$U\frac{\partial \overline{T_J}}{\partial z} = \frac{\alpha_j}{r}\frac{\partial}{\partial r}\left(r\frac{\partial \overline{T_J}}{\partial r}\right) \tag{58}$$

$$\left.\frac{\partial \overline{T_b}}{\partial r}\right|_{r=0} = 0 \tag{59}$$

$$\left.\frac{\partial \overline{T_{wa}}}{\partial r}\right|_{r=R_i} = 0 \tag{60}$$

$$\overline{T_b}(\delta,z) = \overline{T_{wa}}(\delta,z) \tag{61}$$

$$k_b\left.\frac{\partial \overline{T_b}}{\partial r}\right|_{r=\delta} = k_{wa}\left.\frac{\partial \overline{T_{wa}}}{\partial r}\right|_{r=\delta} \tag{62}$$

$$\overline{T_j}(r,0) = T_{in} - S_j(r) - Z_j(0) \tag{63}$$

Steady-State Non-Homogeneous

$$U\frac{\partial Z_j}{\partial z} = \frac{\alpha_j}{r}\frac{\partial}{\partial r}\left(r\frac{\partial S_j}{\partial r}\right) \tag{64}$$

$$\left.\frac{\partial S_b}{\partial r}\right|_{r=0} = 0 \tag{65}$$

$$\left.\frac{\partial S_{wa}}{\partial r}\right|_{r=R_i} = \frac{q''_{wall}}{k_{wa}} \tag{66}$$

$$S_b(\delta) + Z_b(z) = S_{wa}(\delta) + Z_{wa}(z) \tag{67}$$

$$k_b \frac{\partial S_b}{\partial r}\Big|_{r=\delta} = k_{wa} \frac{\partial S_{wa}}{\partial r}\Big|_{r=\delta} \tag{68}$$

The "steady-state" non-homogeneous problem was solved to obtain the thermally-developed solution. Using separation of variables and assuming that both layers possessed the same density and specific heat, the thermally-developed temperature profiles (T_{TD}) for both the bulk and wall-adjacent layers were obtained:

$$T_{TD,b} = \frac{q''_{wall}}{2k_b R_i} r^2 + \frac{2q''_{wall}}{\rho c_p R_i U} z + T_{in} - \left(\frac{q''_{wall}\delta^2}{2R_i}\right)\left(\frac{\delta^2}{2R_i^2} - 1\right)\left(\frac{1}{k_{wa}} - \frac{1}{k_b}\right) - \frac{q''_{wall}R_i}{4k_{wa}} \tag{69}$$

$$T_{TD,wa} = \frac{q''_{wall}}{2k_{wa} R_i} r^2 + \frac{2q''_{wall}}{\rho c_p R_i U} z + T_{in} - \left(\frac{q''_{wall}\delta^4}{4R_i^3}\right)\left(\frac{1}{k_{wa}} - \frac{1}{k_b}\right) - \frac{q''_{wall}R_i}{4k_{wa}} \tag{70}$$

Note that the coefficients were obtained using boundary conditions and by comparing the mean temperature distribution from the 1st law of thermodynamics with the mean temperature calculated using the temperature distributions. The temperature profiles were then used to find the thermally-developed Nusselt number (Equation 22).

To find the complete solution to the energy equation, the "transient" homogeneous problem was solved, using the work of Singh et al. for guidance. The "transient" temperature distributions took the form

$$\overline{T_b} = \sum_{p=1}^{\infty} D_p e^{-\frac{\lambda_{b,p}^2 \alpha_b z}{U}} J_0(\lambda_{b,p} r) \tag{71}$$

$$\overline{T_{wa}} = \sum_{p=1}^{\infty} D_p e^{-\frac{\lambda_{b,p}^2 \alpha_b z}{U}} \left[G_{wa} J_0(\lambda_{wa,p} r) + H_{wa} Y_0(\lambda_{wa,p} r)\right] \tag{72}$$

where D_p, G_{wa}, and H_{wa} represent coefficients and λ represents the eigenvalues. Using the "transient" and "steady-state" solutions, the resulting Nusselt number correlation for the complete solution took the form of a series solution:

$$Nu_{complete} = \frac{2}{\Gamma+\frac{\kappa}{4}-\frac{1}{4}\left(\frac{\delta}{R_i}\right)^4(\kappa-1)} \tag{73}$$

$$\Gamma = \sum_{p=1}^{\infty} E_p \left\{ \left[G_{wa} J_0(\lambda_{wa,p} R_i) + H_{wa} Y_0(\lambda_{wa,p} R_i) \right] - \frac{2}{\lambda_{b,p} R_i} \left(\frac{\delta}{R_i}\right) J_1(\lambda_{b,p}\delta) - \right.$$

$$\frac{2}{\lambda_{wa,p} R_i} \left[G_{wa} J_1(\lambda_{wa,p} R_i) + H_{wa} Y_1(\lambda_{wa,p} R_i) - \left(\frac{\delta}{R_i}\right) \left[G_{wa} J_1(\lambda_{wa,p}\delta) + \right. \right. \tag{74}$$

$$\left. \left. H_{wa} Y_1(\lambda_{wa,p}\delta) \right] \right] \right\}$$

$$G_{wa} = \frac{\sqrt{\kappa} J_1(\lambda_{b,p}\delta) Y_0(\lambda_{wa,p}\delta) - J_0(\lambda_{b,p}\delta) Y_1(\lambda_{wa,p}\delta)}{J_1(\lambda_{wa,p}\delta) Y_0(\lambda_{wa,p}\delta) - J_0(\lambda_{wa,p}\delta) Y_1(\lambda_{wa,p}\delta)} \tag{75}$$

$$H_{wa} = \frac{J_0(\lambda_{b,p}\delta) J_1(\lambda_{wa,p}\delta) - \sqrt{\kappa} J_0(\lambda_{wa,p}\delta) J_1(\lambda_{b,p}\delta)}{J_1(\lambda_{wa,p}\delta) Y_0(\lambda_{wa,p}\delta) - J_0(\lambda_{wa,p}\delta) Y_1(\lambda_{wa,p}\delta)} \tag{76}$$

$$E_p = e^{-\frac{\lambda_{b,p}^2 \alpha_b z}{U}} \frac{1}{n_p} \left\{ \frac{1}{\lambda_{b,p}^2} \left(\frac{\delta}{R_i}\right) \left[\lambda_{b,p} \left(\frac{\delta}{4} \left(\frac{\delta}{R_i}\right)^3 (\kappa - 1) - \kappa \frac{\delta}{2} \left(\frac{\delta}{R_i}\right) + \frac{R_i}{4} \kappa \right) J_1(\lambda_{b,p}\delta) + \right. \right.$$

$$\left. \left(\frac{\delta}{R_i}\right) J_2(\lambda_{b,p}\delta) \right] - \frac{1}{\lambda_{wa,p}^4} \left[G_{wa} \lambda_{wa,p}^2 \kappa \left(J_0(\lambda_{wa,p} R_i) - \left(\frac{\delta}{R_i}\right)^2 J_0(\lambda_{wa,p}\delta) \right) + \right.$$

$$\lambda_{wa,p} \left(\frac{\delta}{R_i}\right) \left\{ \frac{\delta}{4} \left(\frac{\delta}{R_i}\right)^3 \lambda_{wa,p}^2 (\kappa - 1) - \lambda_{wa,p}^2 \kappa \frac{\delta}{2} \left(\frac{\delta}{R_i}\right) + \frac{\kappa}{4R_i} (8 + \right. \tag{77}$$

$$\left. \lambda_{wa,p}^2 R_i^2) \right\} \left(G_{wa} J_1(\lambda_{wa,p}\delta) + H_{wa} Y_1(\lambda_{wa,p}\delta) \right) + H_{wa} \lambda_{wa,p}^2 \kappa \left(Y_0(\lambda_{wa,p} R_i) - \right.$$

$$\left. \left(\frac{\delta}{R_i}\right)^2 Y_0(\lambda_{wa,p}\delta) \right) + \lambda_{wa,p} \left\{ \frac{\delta}{4} \left(\frac{\delta}{R_i}\right)^3 \lambda_{wa,p}^2 (1 - \kappa) + \frac{\kappa}{4R_i} (\lambda_{wa,p}^2 R_i^2 - \right.$$

$$\left. \left. 8) \right\} \left(G_{wa} J_1(\lambda_{wa,p} R_i) + H_{wa} Y_1(\lambda_{wa,p} R_i) \right) \right] \right\}$$

$$n_p = \frac{\delta^2}{2}\Big\{J_0(\lambda_{b,p}\delta)^2 + J_1(\lambda_{b,p}\delta)^2 + \left(\frac{R_i}{\delta}\right)^2\Big[G_{wa}^2\left(J_0(\lambda_{wa,p}R_i)^2 + J_1(\lambda_{wa,p}R_i)^2\right) + 2G_{wa}H_{wa}\left(J_0(\lambda_{wa,p}R_i)Y_0(\lambda_{wa,p}R_i) + J_1(\lambda_{wa,p}R_i)Y_1(\lambda_{wa,p}R_i)\right) + H_{wa}^2\left(Y_0(\lambda_{wa,p}R_i)^2 + Y_1(\lambda_{wa,p}R_i)^2\right)\Big] - \Big[G_{wa}^2\left(J_0(\lambda_{wa,p}\delta)^2 + J_1(\lambda_{wa,p}\delta)^2\right) + 2G_{wa}H_{wa}\left(J_0(\lambda_{wa,p}\delta)Y_0(\lambda_{wa,p}\delta) + J_1(\lambda_{wa,p}\delta)Y_1(\lambda_{wa,p}\delta)\right) + H_{wa}^2\left(Y_0(\lambda_{wa,p}\delta)^2 + Y_1(\lambda_{wa,p}\delta)^2\right)\Big]\Big\} \quad (78)$$

Eigenconditions

$$J_0(\lambda_{b,p}\delta)\left[Y_1(\lambda_{wa,p}\delta)J_1(\lambda_{wa,p}R_i) - J_1(\lambda_{wa,p}\delta)Y_1(\lambda_{wa,p}R_i)\right] + \sqrt{\kappa}J_1(\lambda_{b,p}\delta)\left[J_0(\lambda_{wa,p}\delta)Y_1(\lambda_{wa,p}R_i) - J_1(\lambda_{wa,p}R_i)Y_0(\lambda_{wa,p}\delta)\right] = 0 \quad (79)$$

$$\lambda_{b,p} = \lambda_{wa,p}\sqrt{\frac{1}{\kappa}} \quad (80)$$

Here, κ represents the ratio of the bulk-to-wall-adjacent layer thermal conductivities ($\kappa = k_b/k_{wa}$). MATLAB was used to examine the complete solution results for each system configuration.

Appendix C – Single Particle Effective Thermal Conductivity for Cylinder

The thermal conductivities for a single particle (k_C and k_{NC}) were determined by considering the heat transfer through both the interstitial fluid and the solid particle, similar to the approach used for the flat plate solution. Due to the curved surfaces of both the tube wall and the particle, the resistance across an infinitesimal volume must be considered. Using Figure C.1 as a guide, the infinitesimal resistances can be represented by

$$dR_g = \frac{\ln(R_i/R_1)}{k_g}\frac{R_i}{dA_g} \tag{81}$$

$$dR_s = \frac{\ln(R_1/\delta)}{k_s}\frac{R_1}{dA_s} \tag{82}$$

where k_s represents the thermal conductivity of the solid particle material, dA_g and dA_s represent the infinitesimal areas, and R_1 is the radius of the curve dividing the gas and the particle at a given axial and angular position. Note that a very small tube-to-particle diameter ratio was used in Figure C.1 to exaggerate the curvature and easily display the dimensions utilized.

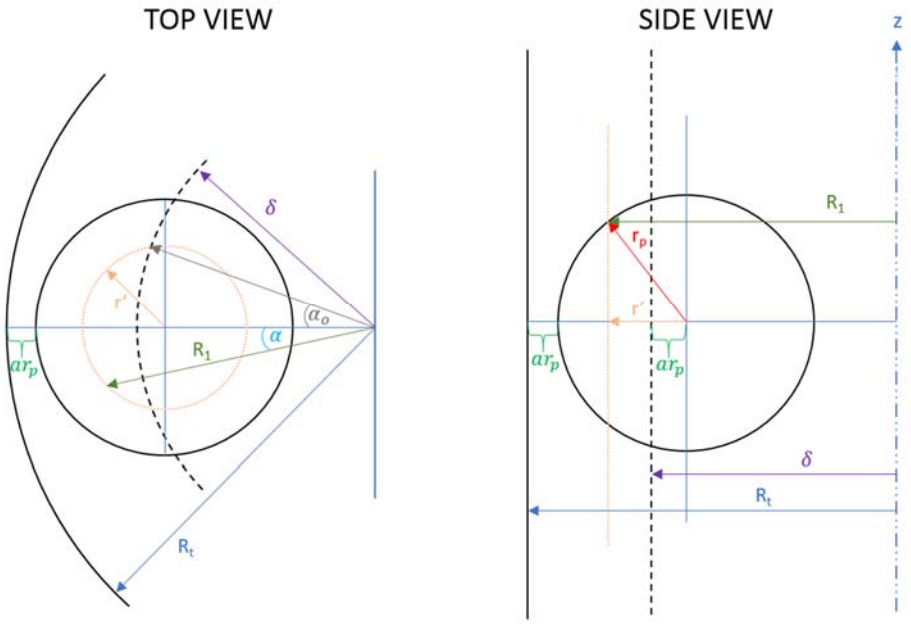

Figure C.1: Schematic of single particle in wall-adjacent layer.

Using Equations 81 and 82, and substituting for the infinitesimal areas, the total infinitesimal thermal resistance can be simplified to

$$dR_{total} = \frac{(K-1)\ln(R_i/R_1)+\ln(R_i/\delta)}{k_s d\alpha dz} \tag{83}$$

The total thermal conductivity based on the heat transfer from the tube wall to the inner "surface" of the wall-adjacent layer can then be determined based on

$$k_{particle} = \frac{\ln\left(\frac{R_i}{\delta}\right) R_i}{A_{particle}} \int_{-r_p\sqrt{1-a^2}}^{r_p\sqrt{1-a^2}} \int_{-\alpha_0}^{\alpha_0} \frac{k_s d\alpha dz}{(K-1)\ln(R_i/R_1)+\ln(R_i/\delta)} \tag{84}$$

$$R_1 = r_p\left[(A-1-a)\cos\alpha + \sqrt{1-\left(\frac{z}{r_p}\right)^2 - (A-1-a)^2\sin^2\alpha}\right] \tag{85}$$

$$\alpha_0 = \arccos\left[\frac{2(A-1-a)^2+2a(A-1-a)+a^2-1+\left(\frac{z}{r_p}\right)^2}{2[(A-1-a)^2+a(A-1-a)]}\right] \tag{86}$$

Here, $A_{particle}$ represents the projected area of the particle on the tube wall through which heat transfer is considered. The area considered for heat transfer depends on the distance from the wall and can be determined according to

$$A_{particle} = 2R_i \int_{-r_p\sqrt{1-a^2}}^{r_p\sqrt{1-a^2}} \alpha_0 dz \tag{87}$$

Note that the above equations are used to calculate the thermal conductivity of particles in contact with the wall ($k_{contact}$) by letting $a = 0$. The effective thermal conductivity of the wall-adjacent layer for a cylindrical wall can be calculated using Equations 30, 31, and 84-87. The volume of a particle in the wall-adjacent layer ($\forall_C, \forall_{NC}$) for a cylindrical system, used to calculate the packing fraction (Equation 31), can be determined using

$$\forall = \int_{ar_p}^{r_p} 2r\sqrt{r_p^2 - r^2}\left[2\pi - 2\arccos\left(\frac{\left(\frac{r}{r_p}\right)^2 - 2Aa - 1 + (1+a)^2}{\left(\frac{r}{r_p}\right)(A - 1 - a)}\right)\right] \tag{88}$$